TITLE PAGE

Title: Divergent opioid-mediated suppression of inhibition between hippocampus and neocortex across species and development

Authors: Adam P. Caccavano[1], Anna Vlachos[1], Nadiya McLean[1], Sarah Kimmel[1], June Hoan Kim[1], Geoffrey Vargish[1], Vivek Mahadevan[1], Lauren Hewitt[1], Anthony M. Rossi[2,3], Ilona Spineux[2,3], Sherry Jingjing Wu[2,3], Elisabetta Furlanis[2,3], Min Dai[2,3], Brenda Leyva Garcia[2,3], Yating Wang[2,3], Ramesh Chittajallu[1], Edra London[1], Xiaoqing Yuan[1], Steven Hunt[1], Daniel Abebe[1], Mark A. G. Eldridge[4], Alex C. Cummins[4], Brendan E. Hines[4], Anya Plotnikova[4], Arya Mohanty[4], Bruno B. Averbeck[4], Kareem Zaghloul[5], Jordane Dimidschstein[3], Gord Fishell[2,3], Kenneth A. Pelkey[1*] and Chris J. McBain[1*]

Affiliations:

[1]*Eunice Kennedy Shriver* National Institute of Child Health and Human Development (NICHD), Section on Cellular and Synaptic Physiology, National Institutes of Health (NIH), Bethesda, MD 20892, USA

[2]Harvard Medical School, Blavatnik Institute, Department of Neurobiology, Boston, MA 02115, USA

[3]Stanley Center for Psychiatric Research, Broad Institute of MIT and Harvard, Cambridge, MA 02142, USA

[4]National Institute of Mental Health (NIMH), NIH, Bethesda, MD 20892, USA

[5]National Institute of Neurological Disorders and Stroke (NINDS) Intramural Research Program, NIH, Bethesda, MD 20892, USA

Corresponding authors email: pelkeyk2@nih.gov (KAP), mcbainc@nih.gov (CJM)

SUMMARY

Within the adult rodent hippocampus, opioids suppress inhibitory parvalbumin-expressing interneurons (PV-INs), thus disinhibiting local micro-circuits. However, it is unknown if this disinhibitory motif is conserved in other cortical regions, species, or across development. We observed that PV-IN mediated inhibition is robustly suppressed by opioids in hippocampus proper but not primary neocortex in mice and nonhuman primates, with spontaneous inhibitory tone in resected human tissue also following a consistent dichotomy. This hippocampal disinhibitory motif was established in early development when PV-INs and opioids were found to regulate early population activity. Acute opioid-mediated modulation was partially occluded with morphine pretreatment, with implications for the effects of opioids on hippocampal network activity important for learning and memory. Together, these findings demonstrate that PV-INs exhibit a divergence in opioid sensitivity across brain regions that is remarkably conserved across evolution and highlights the underappreciated role of opioids acting through immature PV-INs in shaping hippocampal development.

INTRODUCTION

The endogenous opioid system in the CNS plays a crucial role in pain sensation, stress response, and mood[1,2] and is a key target for exogenous drugs of abuse including heroin and fentanyl. With a high risk of dependency, mortality from respiratory depression, and epidemic levels of abuse, opioids have fueled a public health emergency. One third of pregnant women report opioid use, and in almost 60,000 annual pregnancies there is reported opioid abuse[3]. Children born to opioid-dependent mothers are at increased risk of neurodevelopmental deficits within cognitive, psychomotor, and language domains[4]. Despite these risks, there remains an urgent need for potent and safe analgesics. To develop improved opioid or non-opioid analgesics, research is required into the mechanisms of opioids at the cellular and microcircuit level. Novel genetic tools enable us to study the mechanisms of opioids in distinct neuronal subpopulations across species, with the goals of elucidating endogenous opioid function and developing more targeted treatments.

Endogenous opioids (e.g., endorphins, enkephalins) and exogenous opiates (e.g., morphine, fentanyl) act with differing specificities on mu, delta, and kappa opioid receptors (μOR, δOR, and κOR). Notably, μORs are associated with reward-processing of both natural stimuli and drugs of abuse[1,5,6]. These G_i/G_o coupled metabotropic receptors have both pre- and post-synaptic inhibitory secondary effects[7,8] including the pre-synaptic closure of Ca^{2+} channels[9,10] and post-synaptic opening of inward-rectifying K^+ channels[11-13]. Within the hippocampus (HPC), μOR activation has an overall disinhibitory effect on the network[14-17] due to a preferential suppression of inhibitory GABAergic cells[18-20]. Within the CA1 region of HPC, this suppression of inhibition has been primarily associated with parvalbumin-expressing interneurons (PV-INs)[21-23]. Perisomatic-targeting PV-INs of the HPC highly express μORs/δORs, though not exclusively, as lower percentages of dendritic-targeting somatostatin-expressing interneurons (SST-INs) and neuropeptide Y-expressing ivy and neurogliaform cells (NPY-INs) also express μORs/δORs[24,25], and are suppressed by opioids[26,27]. Although μORs/δORs are expressed throughout the CNS[28-32], most functional studies of opioid suppression of interneurons have been restricted to the adult rodent HPC, with less focus on other regions, species, or across development.

PV-INs are critical organizers of rhythmic activity important for learning and memory including sharp wave ripples (SWRs) and gamma oscillations[33]. PV-INs throughout the forebrain have common developmental origins in the medial ganglionic eminence (MGE)[34] and are often treated as monolithic with common circuit motif functionality, leading to textbook observations of inhibitory microcircuits that may not generalize across brain regions[33,35,36]. PV-INs within different brain regions may express unique receptors, as is the case in striatum, where PV-INs express the CB_1 cannabinoid receptor[37], which in HPC is selectively expressed by cholecystokinin-expressing interneurons (CCK-INs)[38]. Given the degree of inhibitory control this neuronal population has over cortical microcircuits, any regional specializations become essential to understand if PV-INs are expected to participate in or be targets of therapeutic

interventions for addiction. Moreover, it is essential to translate any rodent findings to higher species as cellular and circuit motifs may have diverged over 70 million years of evolution, particularly considering evidence of human-specific PV-IN innovations in channel expression and electrophysiological properties[39,40].

In the present study we examined the opioid-mediated suppression of PV-INs across cortical regions, species, and development. We observed this disinhibitory motif was unique to the hippocampus proper (CA1-3), was remarkably conserved from mouse to macaque to human, and was established in early postnatal development, just as inhibitory synapses were being established, with important control over population activity of the developing hippocampus. The hippocampal specificity of opioid-mediated disinhibition has profound implications for rhythmic activities supporting learning and memory. Indeed, prior studies have demonstrated that both SWRs[41] and gamma oscillations[42] are highly sensitive to opioid administration. In the present study we extend these findings to opioid modulation of postnatal population activity, with severe implications for the harmful aspects of opioid use *in utero* and early development. Together, our findings demonstrate that despite common developmental origins in the MGE, not all PV-INs are destined to fulfill equivalent circuit roles.

RESULTS

μORs are selectively enriched in hippocampal PV-INs.

μORs are expressed throughout hippocampus (HPC) and neocortex (CTX)[1], and within the HPC are highly enriched in PV-INs[24,25]. However, less is known about the specificity of μOR expression to PV-INs throughout CTX. To address this, we compared the expression of *Oprm1* (encoding μORs) across HPC and CTX in GABAergic INs via single-nucleus RNA sequencing (snRNAseq) of postnatal day (P)28 mice, observing an enrichment of *Oprm1* in HPC versus CTX within the delineated PV cell cluster (Fig. 1A-B). We next assessed the spatial colocalization of mRNA via RNAscope, observing a decreased percentage of *Pvalb*+ somata colocalized with *Oprm1* in neocortical pyramidal cell layers (both supragranular layers 2/3 and infragranular layers 5/6) in primary motor (M1), somatosensory (S1) and visual (V1) cortex relative to hippocampal pyramidal cell layers in CA (CA1-3, Fig. 1C-D). Notably, we observed several *Oprm1*+*Pvalb*- cells in CTX (Fig. 1C, *open arrow*), which we did not encounter in HPC. To assess if transcript associated with the translational machinery was altered, we employed a RiboTag sequencing approach of all MGE-derived interneurons (MGE-INs, of which PV-INs comprise a substantial fraction[43]), employing Nkx2.1$^{Cre/+}$:Rpl22(RiboTag)$^{HA/HA}$ mice[44-46]. We observed a selective enrichment of *Oprm1* in hippocampal MGE-INs relative to neocortical MGE-INs and all bulk hippocampal/neocortical tissue (Fig. 1E).

At the protein level, we quantified PV-μOR colocalization via immunohistochemistry (IHC) by staining for PV in P70 μOR-mCherry mice (Fig. 1F). μOR-mCherry mice were employed as their expression

83 pattern closely matched μOR antibody signal with brighter somatic labeling (Fig. S1A-B). We observed
84 an increased colocalization of PV and μOR somata across all layers of hippocampal proper (CA1, CA2,
85 CA3) relative to primary cortical regions (M1, S1, V1) and higher-order prelimbic cortex (PrL) (Fig. 1G-
86 H). Hippocampal dentate gyrus (DG) exhibited intermediate PV-μOR colocalization relative to
87 hippocampus proper and neocortex.

88 As hippocampal MGE-INs are born earlier than neocortical MGE-INs (embryonic day (E)11.5[43] versus
89 E13.5[47,48]), we next examined if embryonic PV-IN birthdate was associated with *Oprm1* expression.
90 Through EdU proliferation labeling across E11-15 (Fig. S2A-C), we replicated prior observations that
91 hippocampal versus neocortical PV-INs are born earlier (Fig. S2D). This large biological replicate
92 RNAscope study also fully supported the above RNAscope evaluation of weak *Oprm1* expression within
93 cortical versus hippocampal PV-INs. However, later-born PV-INs were no more likely to express *Oprm1*
94 (Fig. S2E), suggesting factors other than embryonic birthdate establish the hippocampal-neocortical
95 divergence in PV-IN μOR expression.

96 ***Hippocampal PV-INs are selectively hyperpolarized by opioids.***

97 μORs hyperpolarize neurons and reduce neurotransmitter release via combined interactions with
98 inward-rectifying K^+ channels and closure of presynaptic Ca^{2+} channels[7,8]. To determine whether a
99 functional divergence existed between hippocampal and neocortical PV-INs, we recorded in a whole-cell
100 configuration, currents elicited by the administration of μOR agonist DAMGO (100 nM) and antagonist
101 CTAP (500 nM) in PV-tdTomato$^{+/-}$ mice (Fig. 2A-B). Consistent with prior studies[21,22], we observed an
102 outward DAMGO-mediated hyperpolarizing current in CA1 PV-INs voltage-clamped to -50 mV (ΔV = +60
103 ± 12 pA, Fig. 2C, D_1-F_1). However, no significant change in holding current was observed in V1 PV-INs
104 (+12 ± 5 pA, Fig. 2C, D_2-F_2). Of the CA1 PV-INs with sufficiently recovered morphology to assess axonal
105 target (n_{cell} = 5 of 11), 3 exhibited perisomatic-targeting basket cell (BC) morphology, 1 bistratified (BSC)
106 morphology targeting apical and basal dendrites, and 1 axo-axonic (AAC) morphology targeting the axon-
107 initial segment (AIS) of PCs. The hyperpolarizing DAMGO-elicited current was observed in all PV-IN
108 subpopulations (BC: +73 ± 37, BSC: +85, AAC: +101 pA), which is of interest as prior research has
109 suggested AACs are less sensitive than BCs to DAMGO following carbachol administration[42]. V1 PV-INs
110 had somata spanning cortical layers 2 through 6, and of those with sufficiently labeled axons (n_{cell} = 6/15),
111 5 exhibited BC and 1 AAC morphology, with neither subpopulation responsive to DAMGO. The input
112 resistance was also decreased in CA1 PV-INs (Fig. 2G_1), consistent with the opening of ion channels,
113 which was not observed in V1 PV-INs (Fig. 2G_2). We next substituted GTP in the internal pipette solution
114 with the non-hydrolyzable GTP analogue GTPγS, which binds to and prevents further GPCR activation[49],
115 and observed no DAMGO-mediated change in holding current in either CA1 or V1 (Fig. 2H-J), indicating
116 a direct mechanism of GPCRs expressed in the recorded PV-INs. Together, these findings point to a

117 transcriptional, translational, and functional enrichment of μORs within hippocampal versus neocortical
118 PV-INs.

119 ***Opioids selectively suppress hippocampal proper but not neocortical PV-IN mediated inhibition.***

120 To determine if the selective enrichment of μORs within hippocampal PV-INs reduces inhibitory
121 synaptic transmission, we adopted an optogenetic approach to light-activate PV-INs and record their
122 output in downstream pyramidal cells (PCs) in $PV^{Cre/+}$:$ChR2^{fl/+}$ mice (Fig. 3A-B). $GABA_A$-mediated
123 currents were pharmacologically isolated with bath administration of AMPA, NMDA, and $GABA_B$
124 antagonists (μM: 10 DNQX, 50 DL-APV, and 1 CGP55845 respectively), with drugs of interest (nM: 100
125 DAMGO, 500 CTAP) bath administered for at least 5 minutes. Consistent with prior hippocampal
126 studies[21,22], light-evoked inhibitory post-synaptic currents (IeIPSCs) were suppressed by DAMGO in CA1-
127 PCs (Fig. 3C). To assess a pre- or post-synaptic mechanism, we analyzed the coefficient of variation
128 (Fig. 3C), and in a subset of cells, the paired pulse ratio (Fig. 3D), observing an increase in both metrics
129 (Fig. 3E-F), consistent with a presynaptic mechanism and prior studies[21,23]. Notably however, PV-IN
130 output was differentially modulated between HPC and CTX, with significant suppression (64 ± 5% of
131 baseline) observed in CA1-PCs and no suppression (108 ± 6%) observed in M1-PCs (Fig. 3G). To
132 broadly assess this across cortical regions, we recorded IeIPSCs in three hippocampal (CA1, CA3, DG)
133 and four neocortical regions (M1, PrL, S1, V1). Additionally, as differences in PV connectivity have been
134 reported between *radiatum* (*rad.*)- adjacent superficial and *oriens* (*or.*)-adjacent deep PCs (sPCs and
135 dPCs respectively)[50,51], we segregated recordings from these cell populations. DAMGO suppressed
136 IeIPSCs in both CA1-sPCs (55 ± 8%, Fig. 3H) and CA1-dPCs (72 ± 7%, Fig. 3I), with no difference
137 between these cell populations ($p = 0.135$, Fig. S3A). Both in CA1-sPC and CA1-dPC recordings, CTAP
138 reversed the DAMGO-mediated suppression, although this could be achieved through wash alone (data
139 not shown). DAMGO also suppressed IeIPSCs in CA3-PCs (69 ± 6%), although this did not fully reverse
140 with either CTAP or wash (Fig. 3J). Interestingly, this long-lasting μOR-mediated suppression in CA3 is
141 similar to observations of a long-lasting δOR-mediated suppression in CA2 that was not observed in
142 CA1[52]. In DG granule cells (DG-GCs), we observed a highly variable response, with no significant group
143 effect of DAMGO or CTAP (95 ± 8%, Fig. 3K). Throughout neocortex, we also observed highly variable
144 responses with no significant group effects of either DAMGO or CTAP in M1 (108 ± 6%, Fig. 3L), PrL (96
145 ± 8%, Fig. 3M), S1 (107 ± 9%, Fig. 3N), and V1 (89 ± 11%, Fig. 3O). Neocortical PCs were recorded in
146 both supragranular (2/3) and infragranular (5/6) layers. To address the possibility that differing opioid
147 sensitivity between cortical layers contributes to the increased variability in the observed IeIPSC
148 amplitude, we combined primary cortex (M1, S1, V1) PCs and segregated the combined data across
149 L2/3 and L5/6, with no differences observed in the baseline normalized DAMGO response ($p = 0.291$,
150 Fig. S3B). We also explored the increased variability of cortical responses by removing outliers (ROUT

151 method) and all cells with greater than 150% increase from baseline, but still observed no significant
152 group effects (data not shown).

153 We next examined the role of sex, as there have been reported differences in morphine response[53]
154 and μOR trafficking in hippocampal PV-INs[54,55]. Most regions were insufficiently powered to segregate
155 along sex. However, by combining hippocampal proper (CA1, CA3) and primary neocortex (M1, S1, V1),
156 we achieved sufficiently powered groups to analyze via 2-way ANOVA the effects of sex and region. A
157 significant effect of region was found with sex not reaching significance (Fig. S3C). Thus, sex did not
158 appear to be a driving confounder behind the observed hippocampal-neocortical differences.

159 The concentration of DAMGO was selected to be consistent with prior literature[21], but to determine if
160 the lack of cortical effect was due to lower affinity in these regions, we increased the DAMGO
161 concentration 10-fold (1 μM) and observed similar results, with suppression in CA1 (58 ± 8% of baseline)
162 and none in DG (96 ± 11%) or M1 (108 ± 9%, Fig. S3D). These findings were not unique to the selective
163 μOR agonist DAMGO, as the less selective and potent μOR agonist morphine (10 μM) had similar effects
164 in CA1 (56 ± 10%) and S1 (110 ± 12%, Fig. S3E). To test if endogenous opioids were tonically
165 suppressing PV-IN release, we applied neutral antagonist CTAP preceding DAMGO, observing no
166 increase from baseline in CA1 (83 ± 10%) or S1 (99 ± 13%), nor any effect from subsequent DAMGO
167 administration with CTAP still applied (Fig. S3F). As μORs and δORs can become constitutively active,
168 in which they activate G proteins even in the absence of agonist[56,57], we also tested the antagonist
169 naloxone, which can function as an inverse agonist after opioid exposure[58,59]. We observed no increase
170 from baseline in PV-IN output from 1 μM naloxone in CA1 (110 ± 18%) or S1 (81 ± 11%, Fig. S3G). All
171 drug conditions are summarized in Fig. S3H.

172 Although we previously observed DAMGO-mediated hyperpolarization in one morphologically
173 identified PV-AAC, we more thoroughly explored this cell population due to prior reports of divergent
174 opioid response amongst BCs and AACs[42]. We employed the novel BiPVe4(AAC) enhancer virus (see
175 Fig. S4 and[60] for validation), which labels AACs with closely matched features as other strategies to label
176 this subpopulation{Dudok, 2021 #1651;Raudales, 2023 #1973. After injecting WT mice with *pAAV-*
177 *BiPVe4(AAC)-ChR2-mCherry*, we observed a robust DAMGO-mediated suppression of AAC inhibition in
178 CA1 (47 ± 5%, Fig. 3P-R). Moreover, we confirmed DAMGO-mediated outward currents in a larger cohort
179 of AACs (Fig. S4F-H). Critically, suppression of PV-IN inhibition was directly mediated by μORs
180 expressed within PV-INs, as we observed no DAMGO-mediated suppression (92 ± 6%) following
181 selective knockout of *Oprm1* in PV-INs through breeding $PV^{Cre/+}$:$Oprm1^{fl/fl}$ and probing output from these
182 mice after injection with the red-shifted opsin C1V1 under control of Cre-recombinase (Fig. 3S-U and Fig.
183 S5).

184 ***δOR activation and SST-IN inhibition exhibit similar functional HPC-CTX divergence.***

185 Hippocampal PV-INs are also enriched in δORs, with μORs and δORs functioning through partially
186 occlusive downstream pathways to hyperpolarize interneurons{He, 2021 #1680}. In contrast to our
187 observed lack of *Oprm1* expression in neocortical PV-INs, we observed a high level of *Oprd1* transcript
188 within PV-INs in our snRNAseq dataset (Fig. 4A-B), as well as high neocortical *Pvalb-Oprd1*
189 colocalization via RNAscope, albeit significantly less than hippocampal *Pvalb-Oprd1* colocalization (Fig.
190 4C-D). Our RiboTag dataset revealed consistent findings; both hippocampal and neocortical MGE-INs
191 were enriched in *Oprd1*, with higher enrichment in hippocampal versus neocortical MGE-INs (Fig. 4E).
192 We next applied the δOR-selective agonist DPDPE (500 nM) in $PV^{Cre/+}$:$ChR2^{fl/+}$ mice (Fig. 4F), observing
193 a significant suppression in CA1 (76 ± 5%) that did not reach significance in V1 (88 ± 6%, Fig. 4G).
194 However, when analyzing all normalized drug responses with a less conservative 1-way rather than
195 repeated-measures ANOVA of the raw data, we found that across all drug conditions in CTX, only DPDPE
196 resulted in a significant suppression (Fig. S3H). Thus, δOR activation may modestly suppress neocortical
197 PV-IN output.

198 Somatostatin-expressing interneurons (SST-INs) comprise a substantial portion of MGE-INs[43], and
199 within the HPC also express μORs and δORs[25]. Both in HPC and CTX, snRNAseq revealed an apparent
200 enrichment of *Oprm1* and *Oprd1* within SST-INs (Fig. 1A, Fig. 4A,B). We undertook similar optogenetic
201 experiments in $SST^{Cre/+}$:$ChR2^{fl/+}$ mice (Fig. 4H-I), observing that as with PV-INs, IeIPSCs from SST-INs
202 were reversibly suppressed by DAMGO in CA1 (49 ± 5%) but not S1 (99 ± 12%, Fig. 4J). DPDPE resulted
203 in a non-significant suppression in CA1 SST-IN output (62 ± 12%) with no suppression in S1 (101 ± 8%,
204 Fig. 4K). Thus, hippocampal SST-INs appear to exhibit a similar functional specialization as PV-INs
205 regarding opioid response, despite an apparent enrichment of μORs and δORs within neocortical SST-
206 INs. The lack of effect suggests altered subcellular localization with limited opioid receptor expression at
207 PV/SST-IN→PC synapses throughout CTX, in contrast to hippocampal PV/SST-IN→PC synapses.

208 Prior research into the effects of systemic morphine administration on PrL observed microcircuit
209 alterations distinct from our acute DAMGO findings (Fig. 3M), with morphine inducing weakened μOR-
210 dependent PV-IN→PC and strengthened δOR-dependent SST-IN→PV-IN inhibition[61]. The surprising
211 δOR-mediated increase in SST-IN output was linked to an upregulation of *Rac1* and *Arhgef6* specifically
212 in SST-INs. While it is unclear if these downstream plasticity mechanisms occur in our acute
213 DAMGO/DPDPE administrations, the high expression of δORs within neocortical PV-INs/SST-INs and
214 inhibitory interconnections between these populations could contribute to the highly variable neocortical
215 opioid modulation we observed.

216 ***Opioids selectively suppress hippocampal synaptic inhibition in nonhuman primates and***
217 ***resected human tissue.***

218 To determine if μOR-mediated disinhibitory motifs are present in primate species, we turned to the
219 study of rhesus macaques and resected human tissue. ISH RNAscope analysis of adult macaque tissue
220 revealed that, consistent with mice, the percentage of *Pvalb*+ cells co-expressing *Oprm1* was strongly
221 enriched in CA1 (85.4 ± 4.7%), in contrast to neighboring temporal cortex (16.0 ± 5.3%, Fig. 5A-B). To
222 functionally target PV-INs in macaques, we adopted a viral enhancer strategy. Adult macaques were
223 injected with *pAAV(PHP.eB)-S5E2-ChR2-mCherry* in HPC or M1, an enhancer targeting PV-INs [62], which
224 we found to be strongly colocalized with stained PV-INs (Fig. S6A-B). Consistent with our observed PV
225 overlap, S5E2 IeIPSCs in acute macaque slices were insensitive to the N-type Ca^{2+} channel blocker ω-
226 conotoxin (95 ± 7%, Fig. S6C), robustly suppressed by the P/Q-type Ca^{2+} channel blocker ω-agatoxin
227 (10 ± 4%, Fig. S6D), and unaffected by the synthetic cannabinoid agonist WIN 55212-2 (97 ± 5%, Fig.
228 S6E), indicating that primate PV-INs utilize similar synaptic mechanisms as in mice. We next assessed
229 the effect of μOR drugs on IeIPSCs (Fig. 5C-D). As observed in mice, CA1 IeIPSCs were reversibly
230 suppressed by DAMGO (74 ± 3%, Fig. 5E). CA3 IeIPSCs exhibited a long-lasting though non-significant
231 DAMGO suppression (66 ± 9%), which was not easily reversed with CTAP or wash (Fig. 5F). DAMGO
232 elicited a highly variable response with no significant suppression in both DG (102 ± 4%, Fig. 5G) and
233 M1 (111 ± 7%, Fig. 5H).

234 We next assessed the effect of DAMGO/CTAP on resected human tissue from patients with drug-
235 resistant epilepsy (Fig. 5I). We recorded spontaneous IPSCs (sIPSCs) in CA-PCs (CA1 & CA3) and
236 temporal cortex PCs (Fig. 5J). Although sIPSCs include GABAergic currents from all inhibitory
237 interneurons, perisomatic-targeting FS PV-INs are expected to be overly represented in this measure. Of
238 note, several resections exhibited hippocampal sclerosis within CA1, observable as a marked shrinking
239 of *str. pyr.* with few PCs available for patch clamp electrophysiology. Such sclerosis was likely related to
240 the site of epileptogenesis, and sclerotic resections were not included for this study. Neighboring temporal
241 cortical tissue was surgically removed to reach hippocampal structures and was not pathological.
242 Notwithstanding these limitations, human sIPSCs exhibited a markedly similar regional divergence in
243 DAMGO-mediated suppression, with a significant suppression in CA-PCs (63 ± 8%, Fig. 5K) and no
244 suppression of CTX-PCs (111 ± 8%, Fig. 5L). Thus, although we cannot rule out that pathological activity
245 was present in our human hippocampal resections, the remarkable similarity to healthy murine and
246 nonhuman primate tissue would suggest that opioid-mediated suppression of inhibition was at least
247 unimpaired. Comparing across species, this hippocampal-neocortical divergence was remarkably well-
248 conserved across mice (Fig. 5M), macaques (Fig. 5N), and humans (Fig. 5O). An emerging model for
249 this observed difference is that hippocampal PV-INs are enriched in μORs relative to neocortex, resulting
250 in opioid-mediated hyperpolarization and presynaptic suppression of neurotransmission (Fig. 5P).

251 ***Tac1 cells, as a proxy for immature PV-INs, are suppressed by μOR agonists in HPC.***

252 We next explored whether PV-INs exhibit regional opioid divergence in early development. PV-IN
253 function has traditionally been difficult to study in early development as PV itself is not well-expressed
254 until P10 in mice[63]. We undertook an alternate approach from PV^{Cre} mice, with the observation that
255 tachykinin precursor 1 (Tac1, which with post-translational modification produces substance P and
256 neurokinin A) is co-expressed in and can be used as a marker for immature PV-INs[64-67]. To confirm the
257 utility of Tac1 as a marker for immature PV-INs, we examined via snRNAseq of hippocampal interneurons
258 from P10 mice, the expression of principal markers delineating interneurons (Fig. 6A). MGE-INs were
259 distinguished from CGE-INs via expression of *Lhx6*, while *SST* and *Lamp5* (labeling neurogliaform/Ivy
260 cells) labeled clusters of MGE-INs. *Pvalb* at this age was expressed at low levels with high overlap with
261 Tac1. Amongst MGE subgroups at this developmental stage, the future PV cluster was enriched in *Tac1*
262 relative to SST and Lamp5 clusters (Fig. 6B). RiboTag evaluation confirmed that Tac1 associated with
263 the translational machinery was enriched in both HPC and CTX relative to bulk tissue, and in HPC as
264 early as P5 (Fig. 6C).

265 We next conducted IHC for PV in P5, P8, P12, and P45 $Tac1^{Cre/+}$:$tdTom^{fl/+}$ mice (Fig. 6D-E). As
266 previously reported, PV was minimally expressed in P5-8 mice but was detectable within CA1 somata
267 and perisomatic axonal terminals by P12. In contrast, Tac1 somata were readily detectable at all ages,
268 with perisomatic axonal terminals detectable and highly colocalized with PV by P12 (Fig. S7A). We
269 quantified somatic colocalization by counting PV+ and Tac1+ cells across hippocampal and neocortical
270 (S1) layers, observing that the percentage of PV-INs co-expressing Tac1 rapidly increased to 85 ± 1%
271 by P12 (Fig. 6G, left), coinciding with the emergence of labeled PV-INs (Fig. 6H, left). CA1 PV co-
272 expression with Tac1 was maintained in adulthood at 81 ± 2% (Fig. 6G, middle). Across subregions and
273 layers, most PV-INs co-expressed Tac1 in HPC (70 ± 4%) and S1 (58 ± 6%). The inverse measure, the
274 percentage of Tac1 cells co-expressing PV, was somewhat lower, rising to ~50% throughout HPC and
275 S1 in adulthood. Some putative Tac1+ PCs were observed and readily distinguished by morphology and
276 bright fluorescent labeling of dendrites, perhaps representing a limitation of $Tac1^{Cre/+}$:$tdTom^{fl/+}$ mice as
277 they appeared clustered in irregular patches in a minority of sections (27/67 across all ages). Putative
278 $Tac1_{PCs}$ represented a minority fraction, appearing in principal cell layers and comprising 5.9% of all
279 Tac1+ labeled cells. However, their presence warrants caution if employing $Tac1^{Cre}$ mice for functional
280 studies of immature PV-INs without isolating GABAergic transmission or adopting an intersectional
281 approach. Additionally, as there is a reported subpopulation of Tac1-expressing SST-INs[68], we also
282 stained for SST (Fig. 6F). We observed only a small minority of SST cells co-expressing Tac1 and Tac1
283 cells co-expressing SST (4-8%, Fig. 6G-H, right, Fig. S7B), consistent with the limited expression of Tac1
284 in the SST cluster of our snRNAseq data and prior single cell evaluation[69,70].

285 We also assessed Tac1-PV colocalization in adult Tac1$^{Cre/+}$:ChR2$^{fl/+}$ mice, observing that across all
286 layers of CA1 the percentage of PV cells co-expressing Tac1 was 48 ± 3%, while the percentage of Tac1
287 cells co-expressing PV was 74 ± 3% (Fig. S7C-D). We did not observe putative Tac1$_{PCs}$ in this cohort,
288 indicating it may be a reporter-specific observation. These colocalization ratios were effectively inverted
289 from the Tac1$^{Cre/+}$:tdTom$^{fl/+}$ colocalization, likely pointing to the limitations of IHC. ChR2 is a poor somatic
290 label even with immunoboosting, and as PV levels themselves are dynamically regulated[71,72], several
291 PV-INs likely express sub-threshold levels of PV. In a third IHC cohort, we confirmed that hippocampal
292 Tac1 cells were enriched in μOR receptors by triple labeling Tac1$^{Cre/+}$:μOR-mCherry mice injected
293 perinatally with Cre-dependent *pAAV(AAV5)-pCAG-FLEX-EGFP-WPRE* and staining against PV (Fig.
294 S7E) at P13 and P45. Tac1+PV+ at both ages were >50% colocalized with μORs, while Tac1+PV- were
295 non-significantly less colocalized with μORs (~40%). However, in total Tac1+ were enriched in μORs
296 relative to Tac1- cells (Fig. S7F).

297 To more directly assess Tac1 cells as a method to target immature PV-INs, we recorded intrinsic
298 parameters from 90 Tac1+ cells from P5-11 Tac1$^{Cre/+}$:tdTom$^{fl/+}$ mice (Fig. 6I), including from CA1 (44),
299 CA2 (10), CA3 (22), DG (5), and CTX (8). From these cells, 50 hippocampal Tac1+ cells were
300 morphologically reconstructed with visible axon, of which 33/50 (66%) primarily targeted *str. pyr.* and *gr.*
301 consistent with BCs, 11/50 (22%) targeted both *str. or.* and *rad.* consistent with BSCs, 6/50 (12%)
302 primarily targeted superficial dendritic layers, and none exhibited PC morphology (Fig. 6J, Fig. S8).
303 Notably, hippocampal Tac1-IN somata were primarily targeted within *str. pyr*. For comparison of
304 electrophysiological properties, we also recorded from 14 non-labeled putative PCs in HPC, observing
305 striking differences in spiking properties of Tac1-INs versus PCs, consistent with a fast-spiking phenotype
306 expected from PV-INs (Fig. 6K, Fig. S8A-D). We did not observe any regional differences between Tac1-
307 INs (Table S2). To characterize the development of these cells we also recorded from an additional 13
308 P16-18 Tac1-INs, observing maturation to a faster spiking phenotype similar to 10 PV-INs recorded from
309 mature PV-tdTom mice (Fig. S8E-H). Overall, the developmental trajectory of recorded Tac1-IN
310 physiology and morphology closely matched reported progress of immature to mature PV basket cells[73].

311 To assess the opioid sensitivity of Tac1 cells, we applied 100 nM DAMGO to 9 of the recorded
312 hippocampal Tac1 cells in P8-11 mice, observing a reversable hyperpolarizing change in holding current
313 (ΔV = +17 ± 4 pA, Fig. 6L-M). Next, we performed paired recordings of 7 CA1 and 3 CA3 Tac1→PC pairs
314 (Fig. 6N-O) in P10-12 mice, with connected pairs comprising 15% of attempted pairs, observing a strong
315 suppression of transmission in both regions (CA1: 37 ± 5%, CA3: 37 ± 2%, Fig. 6P) and consistent with
316 adult PV→PC pairs[21]. Utilizing Tac1$^{Cre/+}$:ChR2$^{fl/+}$ mice (Fig. 6Q-R), we further explored the opioid
317 modulation of inhibitory output across regions. In P5-7 mice we observed that GABAergic-isolated
318 IeIPSCs were reversibly suppressed by DAMGO in both CA1 (47 ± 4%) and CA3 (34 ± 4%, Fig. 6S).
319 Within S1-L5, we observed that functional Tac1→PC light-evoked synaptic responses were often small

320 and unreliable before the age of ~P8, thus we included in our study slightly older mice with a full age
321 range from P7-10. Consistent with adult PV-INs, we did not observe a significant suppression of Tac1
322 mediated inhibition (89 ± 10%, Fig. 6S). Thus, at the earliest timepoints just as immature PV-IN→PC
323 synaptic connections are being established, there is opioid receptor dependent modulation within the
324 hippocampus not found in neocortex.

325 ***Opioids and Tac1 cells regulate spontaneous activity of the developing hippocampus.***

326 During early postnatal development between P5-10, the principal network signature is that of giant
327 depolarizing potentials (GDPs). These spontaneous synchronous events occur during this critical
328 developmental window while GABA is depolarizing[74] and are believed to play an important role in
329 hippocampal synaptogenesis[75]. To test the importance of opioids in regulating these events, in P5-8 mice
330 we recorded spontaneous GDP associated currents (GDP-Is) intracellularly from CA3-PCs voltage-
331 clamped to 0 mV to isolate GABAergic contributions, in which GDP-Is are detectable as outward events
332 due to a barrage of $GABA_A$ currents (Fig. 7A-B). GDP-I rate was highly variable across brain slices, so
333 to ensure enough events for averaging we only considered slices with ≥ 4 baseline GDPs (69/105 slices
334 across all conditions). We next applied 100 nM DAMGO and observed a robust and reversible decrease
335 in GDP-I event frequency (32 ± 6% of baseline), with no change in GDP-I amplitude (Fig. 7C). DAMGO
336 also suppressed GDPs within S1 cortex (21 ± 9%), which we observed occurring at a lower rate than in
337 CA3 (Fig. S10A-B). δOR agonist DPDPE could also suppress CA3 GDPs (55 ± 13%, Fig. S10C-D), while
338 μOR antagonist CTAP had no effect (104 ± 16%, Fig. S10E-F). Thus, opioid agonists potently suppress
339 spontaneous network activity of the developing brain, analogous to the effect of DAMGO on spontaneous
340 sharp wave ripples (SWRs) in adulthood[41]. To determine if Tac1 cells could subserve this suppressing
341 role, we optogenetically silenced Tac1 cells with $Tac1^{Cre/+}$:$ArchT^{fl/+}$ mice (Fig. 7D-E), observing that GDP-
342 Is were significantly suppressed (76 ± 8% of baseline, Fig. 7F), with no effect on sIPSCs (Fig. S10G).
343 Moreover, Tac1 cell silencing occluded the effect of DAMGO, as DAMGO produced no further reduction
344 in GDP-I frequency (97 ± 16% compared to light-on period, Fig. 7G-I). Prior work from our lab identified
345 MGE-INs as key regulators of GDP activity; optogenetically silencing MGE-INs reduces GDP-I frequency
346 to 34 ± 6% of baseline[76]. Several studies have attributed GDP regulation and generation to dendritic-
347 targeting SST-INs[77,78]. However, optogenetically silencing SST-INs results in only modest reductions of
348 GDP-I frequency (71-80% of baseline)[79]. Thus, to account for the entire effects of DAMGO-mediated
349 suppression and optogenetic MGE-IN silencing, other IN subpopulations likely contribute. This study
350 presents for the first-time evidence that immature PV-INs play a key role in early hippocampal population
351 activity, consistent with the extensive and functional perisomatic innervation already provided by these
352 cells at this stage of development (Fig. 6I-P, Fig. S8) and the essential role adult PV-INs play in
353 hippocampal rhythmogenesis. The limited information regarding immature PV-IN participation in
354 developmental hippocampal population activity likely reflects a prior lack of viable animal model to target

355 these cells. Importantly, the suppression of immature PV-INs by opioids at these early developmental
356 time-points has severe implications for the harmful aspects of opioid use on synaptogenesis and circuit
357 development in the developing brain.

358 ***Morphine pre-treatment occludes acute DAMGO suppression.***

359 Exposure to exogenous opioids can result in a shift in μOR/δOR function to become more
360 constitutively active in chronic[80] and withdrawal conditions[59,81], which is believed to contribute to tolerance
361 and dependence. Drug-induced alterations to the endogenous opioid system have not been well-studied
362 in the hippocampus. One study found chronic morphine treatment results in altered RNA levels of *Penk*
363 and *Gnas* (encoding the $G_{\alpha s}$ subunit of GPCRs)[82], although it is unclear if these changes are specific to
364 distinct neuronal populations. Therefore, to determine if the opioid-mediated suppression of PV-INs is
365 altered after morphine exposure, we injected morphine or saline in $PV^{Cre/+}$:$ChR2^{fl/+}$ mice prior to acute
366 slice preparation and whole cell patch clamp recordings of IeIPSCs. We used three treatment regimens
367 (Fig. 8A), each with an independent saline control group, including a bolus injection (15 mg/kg), a chronic
368 treatment with increasing doses over 6 days (15, 20, 25, 30, 40, 50 mg/kg), and a withdrawal group
369 receiving the chronic treatment but with acute slice preparation 72 hours instead of 1 hour after the final
370 injection as with other groups. Optogenetic IeIPSC recordings were performed in CA1-PCs as previously
371 described. Saline controls all exhibited significant DAMGO-mediated suppression of IeIPSCs (Fig. 8B)
372 similar to un-injected mice (cf. Fig. 3H-I). In morphine-injected mice, the acute DAMGO-mediated
373 suppression was partially occluded, particularly in the withdrawal group for which DAMGO no longer
374 significantly deviated from baseline (Fig. 8C). Comparing the normalized DAMGO response across all
375 groups (Fig. 8D), the bolus and withdrawal groups exhibited a significant deviation from their saline
376 control, which was somewhat moderated in the chronic group, potentially through long-term adaptations
377 distinct from the withdrawal conditions where constitutive receptor activity has been described[59,81].
378 Although the physiological role of the opioid-mediated suppression of hippocampal PV-INs is not yet fully
379 understood, these data indicate that this disinhibitory motif becomes dysregulated after morphine use.
380 Exogenous opioids, in addition to well-described roles in analgesic and stress response, can therefore
381 interfere with neuromodulation of hippocampal PV-INs, leading to disruption of rhythmic activity such as
382 GDPs (Fig. 7), SWRs[41], and gamma oscillations[42], activities essential for learning and memory in the
383 developing and adult brain.

384 **DISCUSSION**

385 PV-INs are essential gatekeepers of cortical activity, supporting excitatory:inhibitory (E:I) balance,
386 feedforward inhibition, gamma oscillations, SWRs, and as observed in this study, GDPs. The ability of
387 opioids to suppress PV-IN activity has critical implications for these roles. This study demonstrates that
388 outside the hippocampus proper, PV-INs largely do not express μOR receptors and are unaffected by
389 μOR agonists. Consistent with these findings, early micro-iontophoresis studies observed that

390 administering enkephalin throughout CTX suppresses network spiking activity, in contrast to HPC where
391 enkephalin increases network activity via disinhibition[14,18]. IHC studies have revealed that μOR-
392 expressing neocortical cells are overwhelmingly GABAergic (97%), but primarily vasoactive intestinal
393 peptide-expressing interneurons (VIP-INs, 92%) rather than PV-INs (8%)[83]. Intriguingly, neocortical μOR-
394 expressing cells largely co-express *Penk*, the precursor to enkephalin, suggesting an auto-suppressing
395 role of these cells. Within HPC, VIP-INs are also the primary source of enkephalin[84], the release of which
396 supports plasticity and social memory[85]. Thus, VIP-INs are the local source of endogenous opioids in
397 both HPC and CTX, but the downstream receptor-expressing cells have shifted to include PV/SST-INs
398 in HPC.

399 Contrasting with this dichotomy, some studies have found evidence for opioid-mediated suppression
400 of PV-INs in select regions of neocortex. In the medial entorhinal cortex (mEC), μ-opioids suppress GABA
401 release from fast-spiking (FS) PV-INs onto stuttering PV-INs, with a consequent increase in gamma
402 oscillations[86]. Voltage-dependent Na^+ currents in prefrontal GABAergic INs are suppressed by DAMGO,
403 though this study did not delineate GABAergic subtype[87]. Within insular cortex, paired recordings from
404 FS, non-FS, and PCs indicate that DAMGO suppresses FS→FS, non-FS→FS but not FS→PC, non-
405 FS→PC connections, while DPDPE suppresses FS→FS, FS→PC but not non-FS→FS, non-FS→PC
406 connections[88], pointing to a complex interplay of interneuronal opioid modulation. Notably, these cortical
407 findings largely agree with our own, with no effect of DAMGO on PV-IN→PC, DAMGO/DPDPE on SST-
408 IN→PC, and a subthreshold effect of DPDPE on PV-IN→PC connections. In orbitofrontal cortex (OFC),
409 electrical- and light-evoked PV-IN inputs to PCs display sensitivity to DAMGO in medial (m) but not lateral
410 (l)OFC[89]. Within neighboring prelimbic cortex (PrL), systemic morphine suppresses light-evoked PV-IN
411 release via μORs but increases SST-IN release onto PV-INs via δORs[61]. Although we observed no
412 significant DAMGO-mediated suppression of PV-IN release across cortex (including PrL), the highly
413 variable responses observed and complex interplay of interneuronal circuitry across CTX evidenced in
414 these studies may prove distinct from microcircuitry motifs in HPC. Another possibility is that
415 phylogenetically older cortical regions such as allocortical HPC, mEC, PrL, and mOFC[90] exhibit region-
416 specific transcriptomic, translational, or post-translational programs permitting the expression of
417 functional μORs within PV-INs.

418 While we observed no evidence that earlier-born PV-INs expressed more μORs (Fig. S2), we did
419 replicate observations of a shifted developmental period of neurogenesis within HPC (E11.5[43]) versus
420 CTX (E13.5[47,48]). In our Tac1 experiments we observed that functional neocortical Tac1→PC synaptic
421 connections were delayed relative to HPC, becoming prominent around P8, while within HPC they were
422 robustly observed at the earliest ages studied (P5). Within HPC, early-born E11.5 PV-INs are reported
423 to express higher PV levels, receive higher synaptic E:I ratios, and preferentially innervate dPCs over
424 sPCs in contrast to late-born E13.5 PV-INs[72]. Within the SST-IN population, a subpopulation of early-

425 born hub cells critically regulate GDPs[77,78]. Thus, the birth date of interneurons strongly determines circuit
426 connectivity and function and, as has been suggested[91], may establish an additional criterion to classify
427 neuronal populations.

428 The energy demands of maintaining functional opioid receptors in hippocampal PV-INs suggest they
429 support important physiological roles. Both exogenous and endogenous opioid release promote long-
430 term potentiation (LTP) within the lateral perforant path to DG[92,93]. Within CA1, LTP is altered in rats
431 chronically treated with morphine[94,95]. The specific PC sub-compartments innervated by opioid-sensitive
432 inputs could also have profound effects on dendritic integration. Although we observed dendritic-targeting
433 CA1 SST-INs were suppressed by opioids (Fig. 4K), as well as prior work demonstrating NPY-INs are
434 suppressed by opioids[27], perisomatic-targeting PV-INs may be the greatest contributors to opioid-
435 mediated disinhibition of PCs. In addition to expressing the highest levels of μORs[24,25], perisomatic
436 inhibition targeting *str. rad*., *pyr*. and *or*. is more susceptible to opioid suppression relative to distal *l.m.*[96],
437 suggesting that opioid-mediated disinhibition may bias a PC to preferentially integrate more proximal
438 Schaffer collaterals relative to distal *l.m.* inputs. Opioids may also play a key role in place field formation.
439 During theta oscillations, a transient reduction in inhibition is critical for place field formation[97]. More
440 specifically, morphine causes place field remapping to environments associated with drug
441 administration[98]. Future studies are needed to explore how place field formation, learning, and memory
442 consolidation are affected by selective PV-IN modulation and opioid treatments.

443 The present study establishes that opioids are uniquely positioned to suppress hippocampal proper
444 and not primary neocortical PV-INs. In contrast to reports of PV-IN evolutionary divergence[39,40], our data
445 demonstrate this disinhibitory circuit motif is maintained across mice, macaques, and humans. This motif
446 is established in early development, and both opioids and immature PV-INs critically regulate
447 hippocampal population activity, suggesting one potential mechanism for neurodevelopmental deficits
448 due to chronic *in utero* opioid exposure[4]. These findings highlight that opioids acting through immature
449 PV-INs have an underappreciated role in regulating developmental hippocampal activity.

450 ## ACKNOWLEDGEMENTS

451 This work was supported by a NICHD Intramural Research Program (IRP) grant to CJM, NINDS IRP
452 grant to KZ, NIMH IRP grant to BBA, and NIH Center on Compulsive Behaviors (CCB) fellowship to APC.
453 This work was carried out in collaboration with the NIH Comparative Brain Physiology Consortium
454 (CBPC) at the NIH IRP. RNA sequencing and analysis support was provided by the Molecular Genomics
455 Core, Bioinformatics and Scientific Programming Core, NICHD. Imaging support was provided by Vincent
456 Schram at the NICHD Microscopy and Imaging Core.

AUTHOR CONTRIBUTIONS

APC was responsible for project conceptualization, experimental design, electrophysiology experiments, imaging, analysis, and principal writer of this manuscript. KAP and CJM conceptualized, designed, and supervised the project. JHK, GV, LH, RC, and KAP contributed to electrophysiology experiments. AV, NM, SK, XY, SH, AR, and IS contributed to IHC and ISH. VM conducted RiboTag experiments and analysis. EL assisted with morphine injections. EF, MD, BLG, and GF conducted snRNAseq data collection, analysis, and interpretation. DA supported mouse breeding, colony maintenance, and genotyping. MAGE, ACC, BEH, AP, AM, and BBA conducted NHP handling, injections, and surgery. KZ conducted surgical procedures with human patients. GF and JD provided support and design of viral constructs. All authors participated in drafting the manuscript. MAGE, BBA, KZ, and CJM provided critical resources for the study.

DECLARATION OF INTERESTS

The authors declare no competing interests.

470 ## FIGURE LEGENDS

471 ***Fig. 1: μORs are selectively enriched in hippocampal PV-INs.***

472 (**A**) snRNAseq of GABAergic INs in P28 mice across HPC and CTX, highlighting *Oprm1* expression.
473 Cardinal clusters of Lhx6-expressing MGE-INs are colored and delineated as SST (*aquamarine*), PV
474 (*red*), and LAMP5 (*peach*) in contrast to caudal ganglionic eminence (CGE)-derived INs (gray). (**B**)
475 *Oprm1* expression of PV cluster cells, n_{cell} = 1920 (HPC), 3935 (CTX) from n_{mice} = 2 (1F), age = P28.
476 Asterisks represent Dunn's *post hoc* comparisons of all HPC/CTX differences for *Oprm1*/*Oprd1* in
477 PV/SST-INs (see *Fig. 4B* for other comparisons). (**C**) *In situ* hybridization (ISH) RNAscope for *Oprm1*
478 and *Pvalb* in wild-type (WT) mice across pyramidal cell layers in CA (CA1-3) regions of HPC and primary
479 neocortical regions M1, S1, V1. Closed arrow (CA1) indicates *Oprm1*+*Pvalb*+ colocalized cell, while open
480 arrow (M1) indicates *Oprm1*+*Pvalb*- cell. (**D**) Colocalization quantification of percentage of *Pvalb*+ somata
481 co-expressing *Oprm1* for 2-5 sections from each of n = 4 (2F) WT mice, age = P62. Asterisks represent
482 Tukey's *post hoc* comparisons after a significant effect of region was observed via 1-way ANOVA. (**E**)
483 RiboTag-associated *Oprm1* expression in n = 4 (2F) P120 Nkx2.1^{Cre}: Rpl22(RiboTag)$^{HA/HA}$ mice,
484 comparing bulk HPC/CTX tissue to MGE-INs. Asterisks represent Tukey's *post hoc* comparisons after
485 significant effects of region, cell type, and region × cell type interaction were observed via 2-way ANOVA.
486 (**F**) Immunohistochemical (IHC) stain for PV in μOR-mCherry mice (boosted with anti-RFP) labeling
487 hippocampal regions: CA1, CA2, CA3, and DG and layers: *stratum* (*str.*) *oriens* (*or.*), *pyramidale* (*pyr.*),
488 *radiatum* (*rad.*), *lacunosum-moleculare* (*l.m.*), *molecular* (*mol.*), *granular* (*gr.*), *hilus* (*hil.*), and neocortical
489 regions: M1, PrL, S1, V1, and layers: L1, L2/3, L4, L5/6. (**G-H**) Quantification of IHC for $n_{section}$ = 4 from
490 n_{mice} = 2F, age = P70 for all layers of indicated region. (**G**) Colocalization quantification of the percent of
491 PV cells co-expressing μORs (*green circles*) and percent of μOR cells co-expressing PV (*magenta*
492 *triangles*). Enlarged markers indicate quantification from example images. Asterisks represent
493 significance of unpaired t-test comparing the percentage of PV cells co-expressing μORs across all HPC
494 and CTX. (**H**) Cell density (cells/mm^2) for μOR-expressing cells (*magenta*), PV cells (*green*) and PV-μOR
495 colocalized cells (*black*). Data are represented as mean ± SEM. * $p < 0.05$, ** $p < 0.01$, *** $p < 0.001$, ****
496 $p < 0.0001$. See *Table S1* for statistical details for this and all subsequent figures.

497 ***Fig. 2: Hippocampal PV-INs are selectively hyperpolarized by opioids.***

498 (**A**) Schematic of whole-cell recordings of PV-INs from PV-tdTom mice voltage-clamped to -50 mV to
499 record the effect of μOR agonist/antagonist DAMGO/CTAP. (**B**) Representative *post hoc* staining of
500 recorded PV-INs in CA1 and V1. (**C**) Average change in holding current elicited by DAMGO/CTAP
501 normalized to baseline for n_{cell} = 11 CA1 from n_{mice} = 5 (3F), age = P37-70 (P57 ± 7) and n_{cell} = 15 V1
502 from n_{mice} = 4 (3F), age = P47-71 (P58 ± 6), with (**D**) example traces showing effects of drugs on baseline
503 holding current (rapid inward and outward currents reflect sEPSCs/sIPSCs), (**E**) *post hoc* reconstructions,
504 (**F**) holding current summary data, and (**G**) input resistance summary data in a subset of cells, for CA1
505 PV-INs (**1***, left*) and V1 PV-INs (**2***, right*). Asterisks represent Tukey's *post hoc* comparisons after a
506 significant effect of treatment was found via 1-way repeated measures ANOVA. (**H**) Example traces
507 showing effect of DAMGO/CTAP with GTPγS substituted for GTP in the internal pipette solution, with
508 DAMGO administration occurring 15 min. after break-in, performed in n_{cell} = 12 CA1 and 12 V1 from n_{mice}
509 = 4 (2F), age = P118-392 (P315 ± 66). Summary statistics for DAMGO-mediated change from baseline
510 in (**I**) holding current and (**J**) input resistance for the four conditions (CA1/V1 and GTP/GTPγS). Asterisks
511 represent Tukey's *post hoc* comparisons after significant effects of region, internal solution, and region ×
512 internal interaction were observed via 2-way ANOVA. In these and all subsequent plots, data from
513 male/female subjects are indicated with a closed/open marker, with enlarged marker indicating example
514 trace.

515 ***Fig. 3: Opioids selectively suppress hippocampal but not neocortical PV-IN inhibition.***

516 (**A**) Schematic of whole-cell recordings of PCs from $PV^{Cre/+}$:$ChR2^{fl/+}$ mice voltage-clamped at -70 mV (with
517 high Cl^- internal) to record the effect of DAMGO/CTAP on light-evoked IPSCs (leIPSCs). (**B**)
518 Representative *post hoc* staining of a recorded CA1 superficial PC (sPC) and M1 layer 2/3 PC. (**C**)
519 Example CA1-PC leIPSC traces, dark lines represent average of ten light grey traces, showing an
520 increased coefficient of variation (CV = SD/mean). (**D**) Example paired pulse ratio (PPR = peak2/peak1)
521 traces recorded in a subset of CA1-PCs. Summary data for (**E**) CV for n_{cell} = 24 from n_{mice} = 10 (5F), age
522 = P28-133 (P55 ± 9) and (**F**) PPR for n_{cell} = 13 from n_{mice} = 3 (2F), age = P78-83 (P80 ± 2). Asterisks
523 represent results of paired t-test/Wilcoxon. (**G**) Average leIPSC peak amplitude normalized to baseline
524 in response to DAMGO/CTAP for n_{cell} = 19 CA1-PCs from n_{mice} = 7 (4F), age = P28-55 (P44 ± 3) and n_{cell}
525 = 16 M1-PCs from n_{mice} = 6 (4F), age = P34-61 (P46 ± 5). Asterisk marks regions where data (10 s bins)
526 survived multiple comparisons via 2-way ANOVA. (**H**-**O**) Mouse leIPSC experiments with (*top*) averaged
527 example traces, (*top inset*) example of brain slices, (*middle*) representative *post hoc* reconstructions, and
528 (*bottom*) summary data in (**H**) n_{cell} = 12 CA1-sPCs from n_{mice} = 6 (3F), age = P28-133 (P62 ± 15), (**I**) n_{cell}
529 = 14 CA1 deep PCs (dPCs) from n_{mice} = 9 (5F), age = P28-133 (P54 ± 10), (**J**) n_{cell} = 17 CA3-PCs from
530 n_{mice} = 7 (2F), age = P41-80 (P65 ± 6), (**K**) n_{cell} = 21 DG granule cells (GCs) from n_{mice} = 9 (3F), age =
531 P41-125 (P69 ± 9), (**L**) n_{cell} = 16 M1-PCs from n_{mice} = 6 (4F), age = P34-61 (P46 ± 5), (**M**) n_{cell} = 12 PrL-
532 PCs from n_{mice} = 3 (2F), age = P34-144 (P107 ± 37), (**N**) n_{cell} = 15 S1-PCs from n_{mice} = 4 (3F), age = P45-
533 52 (P49 ± 2), and (**O**) n_{cell} = 16 V1-PCs from n_{mice} = 6 (2F), age = P27-133 (P73 ± 18). (**P**) Viral bilateral
534 intra-cerebral injection of *pAAV-BiPVe4(AAC)-ChR2-mCherry* in dorsal hippocampus of WT mice, and
535 schematic of leIPSC recording. (**Q**) Representative *post hoc* staining of a recorded CA1-PC (*white*) and
536 viral expression (*orange*, see *Fig. S4* for AAC viral validation). (**R**) Summary data for n_{cell} = 12 CA1-PCs
537 from 1M, age = P50. (**S**) Viral bilateral injection of Cre-dependent *pAAV-Ef1a-DIO-C1V1-mCherry* in
538 dorsal hippocampus of $PV^{Cre/+}$:$Oprm1^{fl/fl}$ mice, and schematic of leIPSC recording. (**T**) Representative
539 *post hoc* staining of a recorded CA1-PC (*white*) and viral expression (*red*). (**U**) Summary data for n_{cell} =
540 9 CA1-PCs from 2M, age = P58-61. Asterisks in (*H-U*) summary plots represent *post hoc* comparisons
541 (Tukey's/Dunn's) after a significant effect of treatment was found via 1-way repeated measure
542 ANOVA/mixed model/Friedman's test.

543 ***Fig. 4: δOR activation and SST-IN inhibition exhibit similar functional HPC-CTX divergence.***

544 (**A**) snRNAseq of cardinal clusters of HPC/CTX MGE-INs, highlighting *Oprd1* expression. (**B**, *left*) *Oprd1*
545 expression in PV cluster cells, n_{cell} = 1920 (HPC), 3935 (CTX) and (*right*) *Oprm1* and *Oprd1* expression
546 in SST cluster cells, n_{cell} = 1518 (HPC), 3002 (CTX), from n_{mice} = 2 (1F), age = P28. Asterisks and non-
547 significant p-values represent results of Dunn's *post hoc* comparisons after comparing all HPC/CTX
548 differences for *Oprm1*/*Oprd1* in PV /SST-INs (including from *Fig. 1B*). (**C**) RNAscope for *Oprd1* and *Pvalb*
549 in WT mice comparing CA1 to V1 (all layers). Majority of cells were *Oprd1*+*Pvalb*+ colocalized (not
550 indicated), with *Oprd1*-*Pvalb*+ cells indicated with open arrows. (**D**) Colocalization quantification of
551 percentage of *Pvalb*+ somata co-expressing *Oprd1* for 1 section each from n = 4 (2F) WT mice, age =
552 P30-32. Asterisks represent significance of unpaired t-test. (**E**) RiboTag-associated *Oprd1* expression in
553 n = 4 (2F) P120 Nkx2.1^{Cre}: Rpl22(RiboTag)$^{HA/HA}$ mice, comparing bulk HPC/CTX tissue to MGE-INs.
554 Asterisks represent Tukey's *post hoc* comparisons after significant effects of region, cell type, and region
555 × cell type interaction were observed via 2-way ANOVA. (**F**) Schematic of whole-cell recordings of PCs
556 recorded in PV$^{Cre/+}$:ChR2$^{fl/+}$ mice voltage-clamped at -70 mV (with high Cl^- internal) to record the effect of
557 δOR agonist/antagonist DPDPE/naltrindole on IeIPSCs. δOR IeIPSC experiments were performed in (**G**)
558 n_{cell} = 14 CA1-PCs and 15 V1-PCs from n_{mice} = 7 (2F), age = P57-90 (P73 ± 5), with (*top*) averaged
559 example traces and (*bottom*) summary data. (**H**) Schematic of whole-cell recordings of PCs voltage-
560 clamped at -70 mV recorded in SST$^{Cre/+}$:ChR2$^{fl/+}$ mice to record the effect of μOR/δOR
561 agonists/antagonists on IeIPSCs. (**I**) Representative *post hoc* staining of recorded CA1 and S1 PCs in
562 SST$^{Cre/+}$:ChR2$^{fl/+}$ mice. SST IeIPSC experiments with (**J**) DAMGO/CTAP were performed in n_{cell} = 7 CA1-
563 PCs and 7 S1-PCs from n_{mice} = 4 (3F), age = P57-240 (P162 ± 46) and with (**K**) DPDPE/Naltrindole in
564 n_{cell} = 7 CA1-PCs and 7 S1-PCs from n_{mice} = 4 (2F), age = P74-135 (P106 ± 13), with (*top*) averaged
565 example traces and (*bottom*) summary data. Asterisks in (*G, J, K)* represent Tukey's/Dunn's *post hoc*
566 comparisons after a significant effect of treatment was found via 1-way repeated measure
567 ANOVA/Friedman's test.

568 ***Fig. 5: Opioids selectively suppress hippocampal inhibition in nonhuman primates and resected***
569 ***human tissue.***

570 (**A**) RNAscope for *Oprm1* and *Pvalb* in adult rhesus macaque. Closed arrow (CA1) indicates
571 *Oprm1+Pvalb+* colocalized cell, while open arrows (CTX) indicate *Oprm1+Pvalb-* cells. (**B**) Quantification
572 of the percentage of *Pvalb+* somata co-expressing *Oprm1* for $n_{section}$ = 3 from 1F, age = 17.6 years.
573 Asterisks represent significance of unpaired t-test. (**C**) Schematic of whole-cell recordings of PCs from
574 S5E2-ChR injected macaques to record the effect of DAMGO/CTAP on leIPSCs. (**D**) Representative *post*
575 *hoc* staining of recorded CA1 and M1 PCs. (**E**-**H**) Macaque leIPSC experiments with (*top*) averaged
576 example traces, (*middle*) representative *post hoc* reconstructions, and (*bottom*) summary data in (**E**) n_{cell}
577 = 6 CA1-PCs, (**F**) 7 CA3-PCs, (**G**) 9 DG-GCs, and (**H**) 8 M1-PCs, from $n_{primate}$ = 5 (2F), age = 7.4-15.9
578 (11.2 ± 1.4) years. (**I**) Schematic of whole-cell recordings of PCs from resected human slices to record
579 the effect of DAMGO/CTAP on spontaneous IPSCs (sIPSCs). (**J**) Representative *post hoc* staining of a
580 recorded CA1 and medial temporal cortex PC. (**K**-**L**) Human sIPSC experiments with (*top*) example
581 traces, (*middle*) representative *post hoc* reconstructions, and (*bottom*) summary data in (**K**) n_{cell} = 16 CA-
582 PCs (CA1 & CA3) and (**L**) n_{cell} = 13 CTX-PCs, from n_{human} = 4 (2F), age = 37.3-54.8 (44.8 ± 3.7) years.
583 Asterisks in (*E-L)* represent Tukey's/Dunn's *post hoc* comparisons after a significant effect of treatment
584 was found via 1-way repeated measure ANOVA/mixed model/Friedman's test. (**M**-**O**) Comparison of
585 DAMGO responses across species revealed a similar hippocampal-neocortical divergence in the opioid-
586 mediated suppression of inhibition across (**M**) mice (data from *Fig. 3H-O*, *bottom*), (**N**) macaques (data
587 from *E-H, bottom*), and (**O**) humans (data from *K-L, bottom)*. Asterisks represent significant deviations
588 from the normalized baseline via 1-sample t-test/Wilcoxon. (**P**) Proposed model: hippocampal PV-INs
589 are selectively enriched in μORs, leading to hyperpolarization and suppressed synaptic release.

590 ***Fig. 6: Tac1 cells, as a proxy for immature PV-INs, are suppressed by μOR agonists in HPC.***

591 (**A**) snRNAseq of GABAergic INs in P10 mice across HPC and CTX. *Far left*, Cardinal clusters of *Lhx6*-
592 expressing MGE-INs are colored and delineated as putative SST (*aquamarine*), PV (*red*), and LAMP5
593 (*peach*) in contrast to caudal ganglionic eminence (CGE)-derived INs (*gray*), with (*left to right*) individual
594 expression of markers *Lhx6*, *SST*, *Lamp5*, *Pvalb*, and *Tac1* indicated. Expression colormap shown in *B*.
595 (**B**) *Tac1* expression of cardinal MGE-IN cell clusters SST, Lamp5, and PV, n_{cell} = 1476 (SST), 920
596 (Lamp5), 1451 (PV) from n_{mice} = 2 (1F), age = P10. Asterisks represent results of Dunn's *post hoc*
597 comparisons after a significant effect of cell type was find via Kruskal-Wallis. (**C**) RiboTag-associated
598 *Tac1* expression in n = 3 P5 and 4 (2F) P60, P120, and P180 Nkx2.1^{Cre}: Rpl22(RiboTag)$^{HA/HA}$ mice,
599 comparing bulk HPC/CTX tissue to MGE-INs. Asterisks represent Tukey's *post hoc* comparisons after
600 significant effects of cell type and region × cell type interaction were observed via 2-way ANOVA. (**D-E**)
601 IHC stain for PV in Tac1$^{Cre/+}$:tdTom$^{fl/+}$ mice, ranging from ages (**D**, *top to bottom*) P5, P8, P12, P45 in
602 CA1, showing the developmental onset of PV expression and colocalization with Tac1, as well as (**E**) in
603 P45 adults throughout S1 cortex (*top*) and HPC (*bottom*). (**F**) IHC stain for SST in Tac1$^{Cre/+}$:tdTom$^{fl/+}$ mice,
604 same ages as *D*. Arrows indicate colocalized cells. Quantification of (**F**) percent colocalization and (**H**)
605 cell density. *Left*: PV-Tac1 CA1 quantification, $n_{section}$ = 2-4 from n_{mice} = 3 each P5, P8, P12. *Middle*: PV-
606 Tac1 quantification for HPC and S1, n_{mice} = 3F P45 (2-4 sections each). *Right*: SST-Tac1 CA1
607 quantification, $n_{section}$ = 2 from n_{mice} = 2 each P5, P8, P12, P45. (**I**) Schematic of whole-cell recordings of
608 Tac1-INs from P5-11 Tac1$^{Cre/+}$:tdTom$^{fl/+}$ mice to measure intrinsic parameters and the effect of DAMGO.
609 (**J**) Example morphological reconstruction of Tac1-INs (see *Fig. S8*). (**K**) Representative firing of Tac1-
610 IN (see *Fig. S9* and *Table S2*). (**L**) Example trace showing slow currents from DAMGO administration
611 and rapid sEPSCs/sIPSCs. (**M**) Holding current summary data across baseline, DAMGO, and wash
612 conditions for n_{cell} = 9 hippocampal Tac1-INs from n_{mice} = 4 (P8-11). (**N**) Schematic of Tac1→PC paired
613 recordings from P10-11 Tac1$^{Cre/+}$:tdTom$^{fl/+}$ mice to measure the effect of DAMGO on unitary currents
614 (uIPSCs). (**O**) Representative paired recording trace, with repetitive current injection to Tac1-IN to elicit
615 firing (*top*) and record uIPSCs in downstream PC (*bottom*). (P) Paired recording summary data of uIPSC
616 peak amplitude in n_{pairs} = 7 CA1 and 3 CA3 Tac1→PC pairs from n_{mice} = 3 (P10-11). (**Q**) Schematic of
617 whole-cell recordings of PCs recorded in Tac1$^{Cre/+}$:ChR2$^{fl/+}$ mice to record the effect of DAMGO on
618 IeIPSCs. (**R**) Representative *post hoc* stains of PCs recorded in CA1, CA3, and S1. (**S**) IeIPSC
619 experiments were performed in n_{cell} = 17 CA1-PCs from n_{mice} = 3 (P5-7), n_{cell} = 9 CA3-PCs from n_{mice} = 2
620 (P6-7), and n_{cell} = 12 S1-PCs from n_{mice} = 3 (P7-10), with (*top*) averaged example traces and (*bottom*)
621 summary data. Asterisks in (*M, P, S*) represent Tukey's/Dunn's *post hoc* comparisons after a significant
622 effect of treatment was found via 1-way repeated measure ANOVA/mixed model/Friedman's test.

623 ***Fig. 7: Opioids and Tac1 cells regulate spontaneous activity of the developing hippocampus.***

624 (**A**) Schematic of recordings of GDP associated currents (GDP-Is), recorded intracellularly in CA3-PCs
625 voltage-clamped to 0 mV in WT mice. (**B**) Example traces of the effect of 100 nM DAMGO applied for 5
626 minutes, with (*right inset*) example GDP-I events. (**C**) DAMGO summary data for GDP-I event frequency
627 and amplitude from n_{cell} = 18 from n_{mice} = 6 (P5-8). (**D**) Schematic of CA3-PC GDP-I recordings from
628 $Tac1^{Cre/+}$:$ArchT^{fl/+}$ mice to silence Tac1 cells. (**E**) Example traces of the effect of ArchT activation with 580
629 nm light for 1-2 min. (**F**) ArchT summary data for GDP-I event frequency and amplitude from n_{cell} = 20
630 from n_{mice} = 6 (P5-8). Asterisks in (*C*, *F*) represent Dunn's *post hoc* comparisons after a significant effect
631 of treatment was found via Friedman's test. (**G**) Schematic of ArchT-DAMGO occlusion in CA3-PCs. (**H**)
632 Example trace of the effect of Tac1-ArchT silencing for 10 min., with 100 nM DAMGO applied 5 min. after
633 start of Tac1-ArchT silencing. (**I**) ArchT-DAMGO occlusion summary data from n_{cell} = 13 from n_{mice} = 4
634 (P6-8). DAMGO administration following Tac1-AchT silencing did not further suppress GDP-I event
635 frequency (*yellow*). DAMGO alone (*orange*) plotted from *C* for comparison. Asterisks represent results of
636 unpaired t-test.

637 ***Fig. 8: Morphine pre-treatment occludes acute DAMGO suppression.***

638 (**A**) Morphine pretreatment experimental design with 3 regimens: bolus (15 mg/kg), chronic (15, 20, 25,
639 30, 40, 50 mg/kg) and withdrawal (chronic regimen + 72 hours). All injections were performed in adult
640 $PV^{Cre/+}$:$ChR2^{fl/+}$ mice with either daily morphine or saline injections, for a total of 6 groups. (**B**) Saline
641 control groups all exhibited significant DAMGO suppression of IeIPSCs recorded in CA1-PCs (cf. *Fig.*
642 *3H-I*). *Bolus*: n_{cell} = 12 from n_{mice} = 3 (2F), age = P64-126 (P103 ± 20). *Chronic*: n_{cell} = 15 from n_{mice} = 3F,
643 age = P67-76 (P73 ± 3). *Withdrawal*: n_{cell} = 14 from n_{mice} = 3 (2F), age = P78-83 (P80 ± 2). (**C**) Morphine
644 injected groups exhibited partial occlusion of acute DAMGO-mediated suppression of IeIPSCs,
645 particularly in the withdrawal group. *Bolus*: n_{cell} = 15 from n_{mice} = 3 (2F), age = P65-127 (P104 ± 20).
646 *Chronic*: n_{cell} = 18 from n_{mice} = 3M, age = P68-76 (P72 ± 2). *Withdrawal*: n_{cell} = 15 from n_{mice} = 3 (2F), age
647 = P77-81 (P79 ± 1). Asterisks in (*B-C*) represent Tukey's *post hoc* comparisons after a significant effect
648 of treatment was found via 1-way repeated measure ANOVA/mixed model. (**D**) Combined DAMGO
649 responses (non-injected data from *Fig. 3H-I* for comparison). Asterisks represent Šídák's *post hoc*
650 comparisons after a significant effect of treatment was found via 2-way ANOVA, with comparisons
651 restricted to those of *a priori* interest (morphine vs. saline for each regimen).

652 # METHODS

653 ## *KEY RESOURCES TABLE*

REAGENT or RESOURCE	SOURCE	IDENTIFIER
Antibodies		
Rabbit anti-Parvalbumin	Abcam	Cat# ab11427, RRID:AB_298032
Mouse anti-Parvalbumin	Sigma	Cat# P3088, RRID:AB_477329
Rabbit anti-Somatostatin 28	Abcam	Cat# ab111912, RRID:AB_10903864
Rabbit anti-μOR	Abcam	Cat# ab134054, RRID:AB_3122135
Rabbit anti-Satb1	Abcam	Cat# ab109122, RRID:AB_10862207
Rabbit anti-pIκBα	Cell Signaling Technology	Cat# 2859, RRID:AB_561111
Chicken anti-GFP	Aves Labs	Cat# GFP-1020, RRID:AB_10000240
Rabbit anti-GFP	Abcam	Cat# ab290, RRID:AB_303395
Guinea Pig anti-RFP	Synaptic Systems	Cat# 390005, RRID:AB_2737051
Rabbit anti-RFP	Antibodies-Online	Cat# ABIN129578, RRID:AB_10781500
AF488 Goat anti-Rabbit IgG (H+L)	Thermo Fisher Scientific	Cat# A-11008, RRID:AB_143165
AF488 Goat anti-Rabbit IgG (H+L)	Thermo Fisher Scientific	Cat# A-11034, RRID:AB_2576217
AF488 Donkey anti-Rabbit IgG (H+L)	Thermo Fisher Scientific	Cat# A-32790, RRID:AB_2762833
CF488A Donkey anti-Mouse IgG (H+L)	Biotium	Cat# 20014, RRID:AB_10561327
CF488A Donkey anti-Rabbit IgG (H+L)	Biotium	Cat# 20015, RRID:AB_10559669
CF488A Donkey anti-Chicken IgY (IgG) (H+L)	Biotium	Cat# 20166, RRID:AB_10854387
AF555 Goat anti-Rabbit IgG (H+L)	Thermo Fisher Scientific	Cat# A-21429, RRID:AB_2535850
AF555 Goat anti-Guinea Pig IgG (H+L)	Thermo Fisher Scientific	Cat# A-21435, RRID:AB_2535856
CF555 Donkey anti-Rabbit IgG (H+L)	Biotium	Cat# 20038, RRID:AB_10558011
CF555 Donkey anti-Guinea Pig IgG (H+L)	Biotium	Cat# 20276-1, RRID:AB_10853597
AF594 Donkey anti-Guinea Pig IgG (H+L)	Thermo Fisher Scientific	Cat# A-11076, RRID:AB_141930
CF647 Donkey anti-Mouse IgG (H+L)	Biotium	Cat# 20046-1, RRID:AB_10853778
CF647 Donkey anti-Rabbit (H+L)	Biotium	Cat# 20047, RRID:AB_10559808
Bacterial and virus strains		
pAAV(PHP.eB)-BiPVe4-ChR2-mCherry	Addgene[60]	RRID:Addgene_213937
pAAV(PHP.eB)-BiPVe4-tdTom-tdTom$_{nls}$	Addgene[60]	RRID:Addgene_213936
pAAV(AAV9)-Ef1a-DIO-C1V1(t/t)-TS-mCherry	Addgene	RRID:Addgene_100061-AAV9
pAAV(PHP.eB)-S5E2-ChR2-mCherry	Addgene[62]	RRID:Addgene_135634-PHPeB
pAAV(AAV5)-pCAG-FLEX-EGFP-WPRE	Addgene[99]	RRID:Addgene_51502-AAV5
Chemicals, peptides, and recombinant proteins		
DAMGO	Tocris	Cat# 1171
CTAP	Tocris	Cat# 1560
DPDPE	Tocris	Cat# 1431
Naltrindole hydrochloride	Millipore Sigma	Cat# N115
Morphine Sulfate Injection, USP (4 mg/mL)	Hikma Pharmaceuticals	NDC: 0641-6125
Naloxone Hydrochloride Injection (0.4 mg/mL)	Mylan Institutional	NDC: 67457-292-02
DNQX disodium salt	Tocris	Cat# 2312
DL-APV	Tocris	Cat# 0105
CGP 55845 hydrochloride	Tocris	Cat# 1248
ω-Agatoxin IVA	Tocris	Cat# 2799

ω-Conotoxin GVIA	Tocris	Cat# 1085
WIN 55212-2 mesylate	Tocris	Cat# 1038
Biocytin	Millipore Sigma	Cat# B4261
AF488 streptavidin	Thermo Fisher Scientific	Cat# S11223
AF555 streptavidin	Thermo Fisher Scientific	Cat# S21381
DAPI	Millipore Sigma	Cat# D9542
RNAscope mouse probe Mm-Pvalb	Advanced Cell Diagnostic	Cat# 421931
RNAscope mouse probe Mm-Oprm1-C2	Advanced Cell Diagnostic	Cat# 315841-C2
RNAscope mouse probe Mm-Oprd1	Advanced Cell Diagnostic	Cat# 427371
RNAscope macaque probe Mmu-PVALB	Advanced Cell Diagnostic	Cat# 461691
RNAscope macaque probe Mmu-OPRM1-C2	Advanced Cell Diagnostic	Cat# 518941-C2
EdU	Thermo Fisher Scientific	Cat# A10044
Opal 520	AKOVA	Cat# OP-001001
Opal 570	AKOVA	Cat# OP-001003
ProLong Diamond Antifade Mountant with DAPI	Thermo Fisher Scientific	Cat# P36962
ProLong Gold Antifade Mountant	Thermo Fisher Scientific	Cat# P10144
GTPγS-Li_4	Sigma	Cat# G8634
Critical commercial assays		
Chromium Single Cell 3' GEM, Library & Gel Bead Kit v3	10x Genomics	Cat# PN-1000075
RNAscope Multiplex Fluorescent v2 Assay	Advanced Cell Diagnostic	Cat# 323100
RNeasy Plus Micro Kit	Qiagen	Cat# 74034
RNA 6000 Pico kit	Agilent	Cat# 5067-1513
SMARTer Stranded Total RNA-Seq. Kit v2	Takara Bio	Cat# 634411
Click-iT EdU imaging Kit	Thermo Fisher Scientific	Cat# C10340
Experimental models: Organisms/strains		
Mouse: $PV^{Cre/Cre}$	Jax[100]	RRID:IMSR_JAX:017320
Mouse: $SST^{Cre/Cre}$	Jax[101]	RRID:IMSR_JAX:013044
Mouse: $Tac1^{Cre/Cre}$	Jax[102]	RRID:IMSR_JAX:021877
Mouse: $Nkx2.1^{Cre/Cre}$	Jax[103]	RRID:IMSR_JAX:008661
Mouse: $Dlx5/6^{Cre/Cre}$	Jax[104]	RRID:IMSR_JAX:008199
Mouse: $tdTomato(Ai9)^{fl/fl}$	Jax[105]	RRID:IMSR_JAX:007909
Mouse: $ChR2(Ai32)\text{-}eYFP^{fl/fl}$	Jax[106]	RRID:IMSR_JAX:024109
Mouse: $ArchT(Ai40D)\text{-}eGFP^{fl/fl}$	Jax[107]	RRID:IMSR_JAX:021188
Mouse: $Rpl22(RiboTag)^{HA/HA}$	Jax[44]	RRID:IMSR_JAX:011029
Mouse: $CAG\text{-}Sun1/sfGFP^{fl/fl}$	Jax[108]	RRID:IMSR_JAX:030952
Mouse: $Oprm1^{fl/fl}$	Jax	RRID:IMSR_JAX:030074
Mouse: μOR-mCherry	Jax[31]	RRID:IMSR_JAX:029013
Mouse: PV-tdTomato	Jax	RRID:IMSR_JAX:027395
Mouse: C57BL/6J	Jax	RRID:IMSR_JAX:000664
Software and algorithms		
pClamp 10.7	Molecular Devices	RRID:SCR_011323
FIJI (ImageJ)	NIH	RRID:SCR_002285
Excel	Microsoft	RRID:SCR_016137
Prism	Graphpad	RRID:SCR_002798

ZEN Microscopy Software	Zeiss	RRID:SCR_013672
SPOT Basic 5.2	SPOT Imaging	RRID:SCR_014313
CellRanger v7.0.0	10x Genomics	
DESeq2	Bioconductor[109]	RRID:SCR_015687
FIJI Macro: colocIHC	this manuscript	https://doi.org/10.5281/zenodo.10063200

654 ## *RESOURCE AVAILABILITY*

655 ### *Lead Contact*

656 Further information and requests for resources and reagents should be directed to and will be fulfilled by
657 the lead contact, Kenneth Pelkey (pelkeyk2@nih.gov).

658 ### *Materials Availability*

659 This study did not generate novel, unique reagents.

660 ### *Data and Code Availability*

661 Data generated during this study are available upon request. The custom ImageJ macro developed to
662 automate IHC colocalization is open-source and available via public repositories: a current version
663 subject to change (https://github.com/acaccavano/colocalizationIHC) and an archival copy used for this
664 manuscript (https://doi.org/10.5281/zenodo.10063200).

665 ## *EXPERIMENTAL MODEL AND STUDY PARTICIPANT DETAILS*

666 ### *Mice*

667 Targeted labeling of neuronal subpopulations was achieved through Cre-recombinase driven
668 expression of floxed reporters/genes, with experimental offspring maintained as heterozygous crosses
669 of the homozygous Cre driver and homozygous floxed reporter mouse lines listed in the Key Resources
670 Table. Ribotag experiments with Nkx2.1$^{Cre/+}$:Rpl22(RiboTag)$^{HA/+}$ offspring were cross-bred for several
671 generations to obtain homozygosity in Rpl22$^{HA/HA}$, to account for the relatively low expression of the
672 endogenous *Rpl22* gene[45,46]. To selectively knock-out *Oprm1* in PV-INs, PV$^{Cre/+}$:Oprm1$^{fl/+}$ offspring were
673 crossed with Oprm1$^{fl/fl}$ mice to achieve homozygosity in floxed *Oprm1*. Viral injections and experiments
674 were also performed in C57BL6/J wild-type (WT) mice.

675 Male and female mice were used in approximately equal number, with those above weaning age
676 sexed by inspection. The number of experimental mice used for this study were: 71 (36F) PV$^{Cre/+}$:ChR2$^{fl/+}$
677 P27-144 (P74 ± 3), 29 C57BL6/J P6-155 (P33 ± 6), 22 Tac1$^{Cre/+}$:tdTomato$^{fl/+}$ P5-45 (P14 ± 3), 15
678 Nkx2.1$^{Cre/+}$:Rpl22(RiboTag)$^{HA/HA}$ P5-180 (P97 ± 17), 13 (8F) PV-tdTomato$^{+/-}$ P37-392 (P136 ± 39), 11
679 Tac1$^{Cre/+}$:ChR2$^{fl/+}$ P5-37 (P15 ± 4), 9 Tac1$^{Cre/+}$:ArchT$^{fl/+}$ P5-8 (P6.8 ± 0.3), 9 (5F) SST$^{Cre/+}$:ChR2$^{fl/+}$ P57-
680 248 (P146 ± 25), 8 (4F) Tac1$^{Cre/+}$:μOR-mCherry$^{+/-}$ P13-45 (P29 ± 6), 4 (2F) Dlx5/6^{Cre}:CAG-Sun1/sfGFP
681 P10-28 (P19 ± 5), 3M PV$^{Cre/+}$:Oprm1$^{fl/fl}$ P58-77 (P65 ± 6), 1F PV$^{+/+}$:Oprm1$^{fl/fl}$ P77, and 2F μOR-mCherry$^{+/-}$

682 P70. Mice were housed and bred in a conventional vivarium with standard laboratory chow and water in
683 standard animal cages under a 12 hr circadian cycle. All rodent experiments were conducted under an
684 Animal Study Protocol approved by the ACUC at the National Institute of Child Health and Human
685 Development.

686 ***Nonhuman Primates (NHPs)***

687 Primate tissue was obtained from 7 (4F) adult rhesus macaques, aged 7-17 (12.2 ± 1.3) years, that
688 had reached the end of their paradigms for other experiments, as part of the NIH comparative brain
689 physiology consortium (CBPC). Of these macaques, 6 were virally injected (5 for acute slice preparation
690 and 1 fixed-perfused for IHC) and 1 was un-injected with tissue flash-frozen for ISH RNAscope. All
691 experiments were performed in accordance with the ILAR Guide for the Care and Use of Laboratory
692 Animals and were conducted under an Animal Study Protocol approved by the ACUC at the National
693 Institute of Mental Health. All procedures adhered to the applicable Federal and local laws, regulations,
694 and standards, including the Animal Welfare Act and Regulations and Public Health Service policy
695 (PHS2002).

696 ***Human Tissue***

697 Human tissue was obtained from surgical specimens collected from 4 (2F) anonymized/deidentified
698 patients with pharmaco-resistant epilepsy, aged 37-54 (44.8 ± 3.7) years. The participants underwent an
699 initial surgical procedure during which recording electrodes were implanted subdurally on the cortical
700 surface and within the brain parenchyma to monitor epileptiform activity. The location of the intracranial
701 electrodes was selected by the clinical team to localize the epileptogenic zone and recordings during a
702 monitoring period were used to identify the specific hippocampal region exhibiting ictal or inter-ictal
703 activity. During a second surgery the brain areas of seizure onset were surgically resected. The
704 Institutional Review Board (IRB) at the National Institute of Neurological Disease and Stroke approved
705 the research protocol and informed consent for the experimental use of surgically resected tissue was
706 obtained from each participant and their guardian.

707 ***METHOD DETAILS***

708 ***Viral Injections (mouse)***

709 For retro-orbital injections of *pAAV(PHP.eB)-BiPVe4-ChR2-mCherry* (Addgene 213937) and
710 *pAAV(PHP.eB)-BiPVe4-tdTom-tdTom*$_{nls}$ (Addgene 213936) viruses, mice were anesthetized with 5%
711 isoflurane then transferred to a nose-cone delivering 2% isoflurane for the duration of the injection. Mice
712 were injected with 80 µL of virus (1:9 dilution with sterile 1x PBS) with a 0.5 mL insulin syringe (BD
713 Syringes) in the retro-orbital sinus.

714 For intra-cranial injections, mice were anesthetized with 5% isoflurane and mounted on a stereotax
715 (Neurostar). Mouse were delivered 2% percent isoflurane throughout surgery. Subcutaneous injection of
716 buprenorphine (0.3 mg/ml) and topical application of lidocaine/prilocaine ointment (2.5%/2.5%) were
717 provided for post-operative analgesia. Injections were delivered with a glass micropipette (Neurostar) at
718 a rate of 100 nL/min. Following injection, the pipette was left in place at site for 5 minutes before removal.
719 Each craniotomy was plugged with Kwik-Sil silicone elastomer (World Precision Instruments Inc.)
720 following removal of pipette. C57BL6/J mice were injected with *pAAV(PHP.eB)-BiPVe4-tdTom-tdTom*$_{nls}$
721 (Addgene 213936) in bilateral dorsal CA1 and CTX (100 nL at each site) at the following coordinates: -
722 2.06 mm caudal and ± 1.60 mm lateral from bregma, 1.48 mm (CA1) and 0.81 mm (CTX) deep from the
723 dura. PV^{Cre}:Oprm1$^{fl/fl}$ mice were injected bilaterally (70 nL at each site) with *pAAV(AAV9)-Ef1a-DIO-*
724 *C1V1(t/t)-TS-mCherry* (Addgene 100061-AAV9, ≥ 1×10^{13} vg/mL) dorsal CA1 at the following coordinates:
725 -2.06 mm caudal and ± 1.40 mm lateral from bregma, and 1.41 mm deep from the dura. Topical lidocaine,
726 TAO, and ketoprofen were provided daily for 3 days following surgery. Mice were injected 2-4 weeks
727 before experiments.

728 For perinatal injections, P0 mice were anesthetized by hypothermia. The scalp was wiped with 70%
729 ethanol and a felt-tipped marker was used to mark the location of the injection over the lateral ventricles:
730 0.8 mm anterior to lambda and 0.8-1 mm lateral to the sagittal suture. Mice were bilaterally injected free-
731 hand with 1 µL of solution containing *pAAV(AAV5)-pCAG-FLEX-EGFP-WPRE* (Addgene 51502-AAV5,
732 ≥ 7 × 10^{12} vg/mL) and 0.05% trypan blue in the lateral ventricle, 2.5 mm below the surface of the scalp,
733 using a 32G microliter Neuros Syringe (Hamilton). Mice were placed on a heating pad until movement
734 returned and were rubbed with bedding material from the home cage before being returned to the mother.

735 ***Viral Injections (macaque)***

736 Intracranial macaque injections were targeted using stereotaxic coordinates derived from MRI and
737 delivered using a needle guide for enhanced accuracy[110]. Surgeries were performed under aseptic
738 conditions in a fully equipped operating suite. *pAAV(PHP.eB)-S5E2-ChR2-mCherry* (Addgene 135634-
739 PHPeB, ≥ 1×10^{13} vg/mL) was injected into HPC and M1 of 6 rhesus macaques. Within HPC, 30-50 µL of
740 total virus was injected, with 15-25 µL of virus injected at each of 2 locations spaced approximately 2 mm
741 apart in the antero-posterior plane, caudal to the level of the uncus. Within M1, 30-40 µL of total virus
742 was injected, with 10 µL of virus injected at each of 3-4 locations spaced approximately 2 mm apart,
743 targeted via direct visualization.

744 For brain extraction, 6-8 weeks after virus injection, animals were sedated with ketamine/midazolam
745 (ketamine 5-15 mg/kg, midazolam 0.05-0.3 mg/kg) and maintained on isoflurane. A deep level of
746 anesthesia was verified by an absence of response to toe-pinch and absence of response to corneal
747 reflex. Prior to brain removal and blocking, 5 macaques for electrophysiology were transcardially perfused
748 with ice-cold sucrose-substituted artificial cerebrospinal fluid (aCSF) containing in mM: 90 Sucrose, 80

749 NaCl, 3.5 KCl, 1.25 NaH_2PO_4, 24 $NaHCO_3$, 10 Glucose, 0.5 CaCl, 4.5 $MgCl_2$ saturated with carbogen
750 (95% O_2, 5% CO_2), with osmolarity 310-320 Osm. One macaque was fixed-perfused for IHC, euthanized
751 following AVMA guidelines, and transcardially perfused with heparinized saline followed by a solution of
752 4% paraformaldehyde (PFA) in 0.1M phosphate buffer. The brain was removed and cryoprotected
753 through an ascending series of glycerol solutions. The cryoprotected tissue was then frozen in isopentane
754 and serially sectioned (at 40 µm) using a sledge microtome. Series with every tenth section (400 µm
755 apart) of free-floating sections were processed for IHC.

756 ***Morphine Injections***

757 $PV^{Cre/+}$:$ChR2^{fl/+}$ mice were injected subcutaneously with morphine or saline in three treatment
758 regimens, including a bolus injection (15 mg/kg), a chronic treatment with increasing doses over 6 days
759 (15, 20, 25, 30, 40, 50 mg/kg), and a withdrawal group receiving the chronic treatment with delayed acute
760 slice preparation. Morphine Sulfate (4 mg/mL, Hikma Pharmaceuticals, NDC:0641-6125) was diluted in
761 saline so that each mouse received the same total volume (300 mL). Injections were performed at 9 AM
762 each day, with acute slices prepared one hour after the final injection, except for the withdrawal group in
763 which 72 hours passed. Mice were injected on a staggered alternating schedule so that 1 mouse was
764 recorded from each day, alternating between saline and morphine.

765 ***Acute Slice Preparation***

766 Adult mice were anesthetized with isoflurane and rapidly decapitated. Brains were dissected, blocked,
767 and sectioned in iced oxygenated sucrose-substituted aCSF. Horizontal or coronal slices (300 µm) were
768 sectioned on a VT-1200S vibratome (Leica Microsystems), then transferred to a submerged incubation
769 chamber containing oxygenated warmed (32-34 °C) sucrose-substituted aCSF for 30 minutes then
770 maintained at room temperature for the duration of the day. Slices were allowed to recover post-
771 sectioning for at least 1 hour before recording. Macaque and human samples were sectioned identically
772 but maintained for up to 72 hours in room temperature oxygenated sucrose-substituted aCSF, with
773 solution changes every 24 hours. Juvenile mice (<P21) were sectioned identically except high-Mg^{2+}
774 instead of sucrose-substituted aCSF was used for dissection, blocking, sectioning, and incubation,
775 containing in mM: 130 NaCl, 3.5 KCl, 1.25 NaH_2PO_4, 24 $NaHCO_3$, 10 Glucose, 1 CaCl, 5 $MgCl_2$, with
776 osmolarity 300-310 Osm. Slices for GDP recordings were sectioned at 500 µm.

777 ***Slice Electrophysiology***

778 Slices were transferred to an upright microscope (Olympus BX51WI) and perfused with oxygenated
779 extracellular aCSF containing in mM: 130 NaCl, 3.5 KCl, 1.25 NaH_2PO_4, 24 $NaHCO_3$, 10 Glucose, 2.5
780 CaCl, 1.5 $MgCl_2$, with osmolarity 300-310 Osm, with a flow rate of 2-3 mL/min at a temperature of 30-33
781 °C. Individual cells were visualized with a 40x objective using fluorescence and IR-DIC microscopy.
782 Electrodes were pulled from borosilicate glass (World Precision Instruments) to a resistance of 3-5 MΩ

783 with a vertical pipette puller (Narishige PC-10). Whole-cell patch-clamp recordings were made with a
784 Multiclamp 700B amplifier (Molecular Devices), with signals digitized at 20 kHz (Digidata 1440A, filtered
785 at 3 kHz). Recordings were made using a Windows 10 computer with pClamp 10.7 (Molecular Devices).
786 In voltage-clamp recordings, uncompensated access resistance (R_A) was monitored consistently with 5
787 mV voltage steps. Any recordings in which R_A deviated by more than 20% were discarded, as were any
788 with unstable leak current.

789 Direct response to opioids were recorded in fluorescently-identified cells with a standard K-Gluconate
790 internal containing in mM: 150 K Gluconate, 0.5 EGTA, 3 $MgCl_2$, 10 HEPES, 2 ATP•Mg, 0.3 GTP•Na_2,
791 and 0.3% biocytin (pH corrected to 7.2 with KOH, 285-290 Osm). Cells were held in voltage-clamp at -
792 50 mV, and 100 nM DAMGO (μOR selective agonist) and 500 nM CTAP (μOR selective neutral
793 antagonist) applied. GPCR function was occluded with an alternate internal solution replacing the 0.3
794 mM GTP•Na_2 with 1 mM GTPγS • Li_4, allowing 15 min of baseline before applying DAMGO/CTAP.

795 Recordings of inhibitory light-evoked and spontaneous inhibitory post-synaptic currents (leIPSCs and
796 sIPSCs) were made in visually-identified PCs held in voltage-clamp at -70 mV, with a high Cl^- K-
797 Gluconate internal (calculated Cl^- reversal = -24 mV), containing in mM: 100 K Gluconate, 50 KCl, 0.5
798 EGTA, 3 $MgCl_2$, 10 HEPES, 2 ATP•Mg, 0.3 GTP•Na_2, 4 QX314, and 0.3% biocytin (pH corrected to 7.2
799 with KOH, 285-290 Osm). A brief (0.5-2 ms) 470 nm light pulse train (20x at 10 Hz) illuminated a small
800 patch surrounding the recorded cell every 10 s. The light intensity was kept consistent between cells as
801 much as possible, but as every recording was internally normalized to baseline, greater importance was
802 placed on ensuring the leIPSC amplitude was detectable above noise and non-saturating (100-1000 pA).
803 $GABA_A$ currents were isolated by washing into the bath 10 μM DNQX, 50 μM DL-APV, and 1 μM CGP
804 55845, to eliminate the contributions of AMPA, NMDA, and $GABA_B$ receptors, respectively. After a stable
805 baseline was reached (5+ min), the opioids of interest were applied in the following nM concentrations:
806 100/1000 DAMGO, 500 CTAP, 500 DPDPE (δOR selective agonist), 100 naltrindole (δOR selective
807 neutral antagonist), 10000 morphine (μOR/δOR agonist), and 1000 naloxone (μOR/δOR
808 antagonist/inverse agonist). Each drug was applied for at least 5 min. Opioid concentrations were
809 selected from prior publications[21,52,58,111]. Detailed dose-response experiments were not conducted.

810 Intrinsic membrane and firing properties were recorded in cells with a standard K-Gluconate internal.
811 Resting membrane potential (RMP) was measured in a tight cell-attached configuration, voltage-clamped
812 to +60 mV during 100 ms voltage ramps (from +100 to -200 mV) every 5 s and followed after break-in
813 and a whole-cell current-clamp configuration with holding current I = 0. Membrane time constant (tau)
814 was measured by 20 repeated 400 ms hyperpolarizing current pulses of -20 pA. Input resistance (R_{in})
815 was determined by recording the response to 20 increasing current pulses (2 s duration from -50 pA with
816 increasing 5 pA increments). Sag index was measured during 800-1000 ms current steps in which the
817 peak voltage V_{peak} = -100 mV. Action potential (AP) and after-hyperpolarization (AHP) characteristics

818 were measured during 800-1000 ms current steps near spike threshold. Mean max firing and spike
819 adaption properties were measured during 800-1000 ms current steps at the maximum depolarizing
820 current that preceded depolarization block. The range of current steps was dependent on input resistance
821 and set for each cell to cover voltage responses from -100 mV to threshold to maximum firing.

822 Paired Tac1→PC recordings were conducted by targeting and characterizing intrinsic parameters of
823 a fluorescently-identified Tac1 cell with a standard K-Gluconate internal, followed by targeting a non-
824 labeled PC and recording in voltage-clamp at -70 mV with a high Cl^- K-Gluconate internal. A train of
825 depolarizing current pulses (20x 2 ms 1-2 nA at 100 Hz) was injected into the pre-synaptic Tac1 cell to
826 elicit unitary IPSCs (uIPSCs) in the post-synaptic PC. Multiple post-synaptic PCs were targeted within
827 the same slice until detectable uIPSCs were observed, after which the drug of interest (100 nM DAMGO)
828 was applied.

829 Giant depolarizing potential associated currents (GDP-Is) were recorded intracellularly, by recording
830 visually-identified PCs voltage-clamped to 0 mV in standard K-Gluconate. Optogenetic inactivation of
831 Tac1 cells was achieved by sustaining a light pulse for 2-3 min at 580 nm in ArchT-expressing mice.

832 ***Electrophysiology Analysis***

833 All electrophysiology analysis was conducted in Clampfit 10.7 (Molecular Devices) and processed in
834 Microsoft Excel. Drug responses of the holding current were calculated as the final 2 min average for
835 each drug condition. IeIPSC amplitudes recorded in PCs were calculated as the final ten sweep average
836 for each drug condition. sIPSCs were detected using a template search and averaged for the final 2 min
837 of each drug condition. GDP-Is were detected using a threshold set above spontaneous sIPSCs and with
838 a minimum event duration of 25 ms. GDP-Is were quantified for the final 2 min of each drug condition,
839 and only recordings with a rate ≥ 2 events/min in the baseline period were included. GDP-Is recorded in
840 S1 occurred at a significantly lower rate, and thus were conducted over longer recordings, quantified in
841 the final 4 min of each drug condition and included if ≥ 1 event/min within the baseline period.

842 Intrinsic membrane and firing properties were analyzed as follows: RMP was calculated as the linearly-
843 extrapolated intersection point along the voltage ramp as previously described[112], or the mean voltage in
844 I = 0 whole-cell recordings. Tau was determined by fitting the mean voltage response to hyperpolarizing
845 current injections with an exponential function. R_{in} was determined by taking the slope of a linear
846 regression of the change in voltage in response to increasing current pulses around RMP. The sag index
847 was determined by measuring the maximum hyperpolarization voltage deflection (V_{peak}) from baseline
848 (V_{rest}) at the onset of the current pulse, and the steady-state voltage deflection (V_{ss}) in the last 200 ms of
849 the current pulse. The sag index was calculated as $(V_{rest} – V_{ss}) / (V_{rest} – V_{peak})$. AP threshold was measured
850 as the voltage at which the slope exceeds 10 mV/ms, and half-width as the width of the AP (ms) at half
851 the maximum voltage amplitude. AHP amplitude and time was measured at the peak hyperpolarization

852 voltage deflection from AP threshold. The maximum firing frequency was measured as the mean
853 frequency during the maximum 800-1000 ms AP train, while the accommodation ration was measured
854 as the ratio of the final (last 3 spikes) over the initial (first 3 spikes) instantaneous frequency.

855 ***Single nucleus RNA sequencing (snRNAseq)***

856 Detailed acquisition and analysis procedures of single nucleus RNA sequencing (snRNAseq)
857 datasets of P10 and P28 hippocampal interneurons will be included in a subsequent publication. In brief,
858 hippocampal tissue was dissected from Dlx5/6^{Cre}:CAG-Sun1/sfGFP mice. Nuclei were isolated as
859 previously described[113] and subsequently sorted on a Sony SH800S cell sorter for GFP+ nuclei.
860 snRNAseq libraries were prepared using the Chromium single cell 3' library and gel beads kit (10x
861 genomics, Cat# PN-1000075). CellRanger v7.0.0 (10x Genomics) was used with default parameters to
862 map snRNAseq data to the mouse reference genome (mm10) provided by 10x Genomics. The
863 snRNAseq data was then processed and annotated using the pipeline as previously described[114].

864 ***In situ Hybridization (ISH) RNAscope***

865 To prepare snap frozen tissue for ISH, freshly dissected brains or brain blocks were submerged into
866 2-methylbutane that was pre-chilled on a dry ice/ethanol bath for 1 minute. Tissue was removed, wrapped
867 in foil, and stored at -80 °C. 10 µm frozen sections were made using a Leica Cryostat, mounted on slides
868 (ThermoFisher Scientific) and stored at -80 °C.

869 Target probes were designed and manufactured by Advanced Cell Diagnostic (ACD): Mm-Pvalb (Cat#
870 421931), Mm-Oprm1-C2 (Cat# 315841-C2), Mm-Oprd1 (Cat# 427371), Mmu-PVALB (Cat# 461691),
871 Mmu-OPRM1-C2(Cat# 518941-C2). ISH was performed following the RNAscope Multiplex Fluorescent
872 v2 Assay instructions provided by ACD. Briefly, frozen thin sections were post-fixed in 4% PFA and
873 dehydrated sequentially in 50%, 70% and 100% ethanol. After H_2O_2 and Protease IV treatment, sections
874 were incubated with probes at 40 °C for 2 hours. Probed signals were detected using RNAscope Multiplex
875 Detection v2 kit (ACD, Cat# 323100). Opal 520 (AKOVA, Cat# OP-001001) and Opal 570 (AKOVA, Cat#
876 OP-001003) were used to detect C1 and C2 probes, respectively. After DAPI staining, sections were
877 covered using ProLong Gold Antifade Mountant (ThermoFisher Scientific, Cat# P10144) and cured in
878 darkness before imaging.

879 ***EdU Protocol***

880 Timed pregnant C57BL/6 Mice (Charles River) were injected once each with 1.25 mg of EdU (Thermo
881 Fisher, Cat# A10044) at E11, E12, E13, E14, and E15 via intraperitoneal injection. Upon reaching P30-
882 32, mice were anesthetized with sodium pentobarbital (Euthasol) via intraperitoneal injection and
883 transcardially perfused with 1x PBS followed by 4% PFA. Brains were then dissected and post-fixed in
884 4% PFA overnight at 4° C. PFA-fixed brain samples were cryopreserved in 30% (w/v) sucrose and
885 sectioned into 20 µm coronal slices using a sliding microtome (Leica). Brain slices were preserved in

886 Storage Buffer, comprising 28% (w/v) sucrose, 30% (v/v) ethylene glycol in 0.1 M sodium phosphate
887 buffer, at -80 °C until further processing. mRNA transcripts were detected using the RNAscope Multiplex
888 Detection v2 kit (ACD, Cat# 323100), following the manufacturer's protocol. The RNAscope catalogue
889 probes used included *Oprm1* (#315841-C2), *Oprd1* (#427371), and *Pvalb* (#421931-C3). Following
890 RNAscope, EdU was detected using the Click-iT EdU imaging Kit (Thermo Fisher, Cat# C10340). For
891 each time point analyzed, two animals from the same litter were used, and two sections were taken from
892 each brain. Images of RNAscope ISH experiments were collected using an upright confocal microscope
893 (Zeiss LSM800) with a 10x objective (Plan-Apochromat 10x/0.45 M27), with stitching performed using
894 the Zeiss software.

895 ***RiboTag***

896 This assay was performed as previously described[44-46]. RNA bound with anti-HA immunoprecipitates
897 and RNA from bulk tissue were purified using RNeasy Plus Micro Kit (Qiagen, Cat# 74034) and the quality
898 of RNA was measured using RNA 6000 Pico kit (Agilent, Cat# 5067-1513) and 2100 Bioanalyzer system
899 (Agilent, Cat# G2939BA). cDNA libraries were constructed from 250 pg RNA using the SMARTer
900 Stranded Total RNA-Seq. Kit v2 (Takara Bio, Cat# 634411) from samples with RNA Integrity Numbers >
901 6. Sequencing of the libraries was performed on the Illumina HiSeq 2500, at 50 million 2 × 100 bp paired-
902 end reads per sample. ~75% of reads were uniquely mapped to genomic features in the reference
903 genome. Bioconductor package DESeq2[109] was used to identify differentially expressed genes (DEG).
904 This package allows for statistical determination of DEGs using a negative binomial distribution model.
905 The resulting values were then adjusted using the Benjamini and Hochberg method for controlling the
906 false discovery rate.

907 ***Immunohistochemistry (IHC)***

908 For mice younger than P10, brain tissues were dissected and drop fixed in 4% PFA for 24 hours at 4
909 °C. Mice older than P10 were transcardially perfused using 4% PFA and dissected brain tissues were
910 post-fixed in 4% PFA for 24 hours at 4 °C. Fixed brain tissues were thoroughly washed in 1x phosphate
911 buffer (PB) followed by cryopreservation using 30% sucrose. 50 µm coronal sections were made on a
912 frozen microtome. Brain slices were washed with 1x PB at room temperature for 1 hour with 2-3 changes
913 of 1x PB. To perform floating section IHC, brain slices were blocked and permeabilized in Blocking
914 Solution (1x PB + 10% goat serum + 0.5% Triton X-100) at room temperature for at least 2 hours. Primary
915 antibodies were diluted using Antibody Solution (1x PB + 1% goat serum + 0.1% Triton X-100). Blocked
916 brain slices were incubated in primary antibodies at 4 °C for 48 hours. After wash with 1x PB at room
917 temperature for 15 minutes with 3 repeats, brain slices were incubated in secondary antibodies diluted
918 with Antibody Solution at room temperature for 1 hour. After wash with 1x PB at room temperature for 15
919 minutes with 3 repeats, brain slices were mounted on gelatin coated slides followed by air drying, cover-

920 slipped with Prolong Diamond Antifade mountant with DAPI (ThermoFisher Scientific Cat# P36962),
921 cured in darkness, and imaged. Primary and secondary antibodies with product numbers listed in Key
922 Resources Table, with working dilutions of 1:1000 for all except primary Rabbit anti-pIκBα (Cell Signaling
923 Technology Cat# 2859, RRID:AB_561111) and secondary CF647 Donkey anti-Mouse (Biotium Cat#
924 20046-1, RRID:AB_10853778), both at 1:500.

925 ***Morphological Reconstruction***

926 Slices containing biocytin filled cells were drop fixed in 4% PFA overnight at 4 ºC. Fixed slices were
927 then washed in PBS, permeabilized with 0.3% Triton X-100 and incubated with Alexa-488 or Alexa-555
928 conjugated streptavidin overnight (Thermo Fisher Scientific, Cat# S11223, S21381). When additional
929 staining was desired, tissue was incubated in Blocking Solution (Carrier Buffer + 10% goat serum + 0.5%
930 Triton X-100) at room temperature for at least 2 hours. Primary antibodies were diluted using Carrier
931 Buffer (1% bovine serum albumin + 1% goat serum in PBS) containing 0.5% Triton X-100 for 3 hours at
932 room temperature. After washing with 1x PBS at room temperature for 15 minutes with 3 repeats, tissue
933 was incubated with secondary antibodies diluted with Carrier Buffer and Triton at room temperature for
934 2 hours. After incubation, slices were incubated in 1 µg/ml DAPI (Millipore Sigma, Cat# D9542), then
935 underwent multiple washes, cryopreserving in 30% sucrose and were resectioned to 70 µm using a
936 freezing microtome (Microm, Whaltham, MA). Slices were then mounted on glass slides (Fisher Scientific,
937 Fisherbrand Superfrost Plus) using Mowiol as a mounting medium. Confocal images of labelled cells
938 were attained on Zeiss LSM 710 and LSM 900 microscopes using a 20x objective. Primary and secondary
939 antibodies with product numbers listed in Key Resources Table, with working dilutions of 1:1000.

940 ***IHC and ISH Image Acquisition and Analysis***

941 IHC Images were captured on a Zeiss LSM 900 (confocal 20x and Airyscan 63x) and an Olympus
942 VS200 slide scanner. Quantified images were captured from 2-5 sections for each subject. Microscope
943 settings were kept consistent for all sections from each subject. Lower resolution confocal (20x) images
944 used a broad z-stack (5 slices every 1.1 µm) which were maximum projected before subsequent analysis.
945 High resolution Airyscan (63x) images used a detailed z-stack (60-70 slices every 0.15 µm). RNAscope
946 images were first acquired on a SLIDEVIEW VS200 slide scanner (Olympus) mounted with an ORCA-
947 Fusion Digital Camera (HAMAMATSU). Hippocampal and neocortical regions were scanned at 20x,
948 guiding subsequent 63x confocal z-stack images at regions of interest (ROIs).

949 For each image, polygonal ROIs were drawn to demarcate hippocampal/neocortical layers and
950 subregions. Mean intensity and correlation across channels for each ROI were then computed by a
951 custom ImageJ (FIJI) macro (see Data and Code Availability). Cells were manually counted for
952 colocalization analysis with the built-in FIJI multiselect tool independently for each channel in 3-4 sections
953 for each subject. The above macro was used to subdivide the counts between ROIs, compute the

954 average cell intensity, ROI intensity, and ROI area. The average signal-to-noise ratio (SNR), defined here
955 as the mean cell intensity divided by the mean ROI SD, was determined to be significantly greater than
956 1 for all manual counts (see Table S1).

957 ***QUANTIFICATION AND STATISTICAL ANALYSIS***

958 Statistical analysis was conducted in Graphpad Prism 10. All data were tested for normality and
959 lognormality with Shapiro-Wilk tests. Parametric tests were selected if all groups were normal. If at least
960 one group was non-normal and all groups were log-normal, data were log-transformed prior to parametric
961 testing. If data were neither normal nor log-normal, non-parametric tests were used whenever available.
962 Throughout, summary data are presented as mean ± SEM with symbols representing individual values.
963 Additional descriptive statistics and details of hypotheses testing are available for each figure in Table
964 S1.

965 Cellular responses to drug treatments were analyzed with a 1-way repeated-measures design
966 (ANOVA/Friedman, with Tukey's/Dunn's *post hoc* multiple comparisons). All statistical tests were
967 conducted on raw non-normalized data, including plots showing responses normalized to baseline.
968 Experiments missing at most one condition (CTAP/naltrindole) were included and analyzed with a mixed-
969 effects model. Comparisons of the normalized DAMGO responses between regions were performed with
970 a 1-sample t-test/Wilcoxon, comparing to 1 (baseline) and correcting sigma for the number of
971 comparisons. Comparisons between different brain regions' drug responses over time were analyzed
972 with a 2-way design (region × time), with Šídák's multiple comparisons restricted to comparisons between
973 time-equivalent bins. In general, *post hoc* tests for 2-way analyses were restricted to comparisons of *a*
974 *priori* interest, employing Šídák's multiple comparisons tests.

975 **SUPPLEMENTAL INFORMATION**

976 ***Fig. S1****: μOR-mCherry mouse model validation.*

977 ***Fig. S2****: Earlier-born PV-INs are not more likely to express Oprm1.*

978 ***Fig. S3****: Additional PV-IN optogenetic experiments.*

979 ***Fig. S4****: Validation of axo-axonic cell (AAC) specific BiPVe4 virus in rodent hippocampus.*

980 ***Fig. S5****: Validation of PV-IN selective Oprm1 knockout.*

981 ***Fig. S6****: Validation of PV-specific S5E2 virus in rhesus macaques.*

982 ***Fig. S7****: Additional IHC validation of Tac1^{Cre} mice as a model for immature PV-INs.*

983 ***Fig. S8****: Morphological reconstructions of Tac1-INs in early development display perisomatic phenotypes*
984 *consistent with immature PV-INs.*

985 ***Fig. S9****: Intrinsic electrophysiological analysis of Tac1-INs reveals a fast-spiking phenotype consistent*
986 *with immature PV-INs and distinct from PCs.*

987 ***Fig. S10****: Additional GDP experiments.*

988 ***Table S1****: Statistical details.*

989 ***Table S2****: Intrinsic Parameters.*

990 ***Fig. S1: μOR-mCherry mouse model validation.***

991 (**A**) Coronal sections of IHC stain with antibody against μOR in μOR-mCherry mice (boosted with anti-
992 RFP), bregma = -1.3 (*left*) and -3.3 (*right*). (**B**) Areas of high μOR expression at 20x magnification
993 including hippocampus (HPC, *left*), habenula (Hb, *middle*), and interpeduncular nucleus (IPN, *right*). μOR
994 antibodies (cyan) exhibited weaker somatic labeling than mCherry expression (red), but both channels
995 appeared well colocalized. IHC performed in 2F P70 with consistent observations.

996 ***Fig. S2: Earlier-born PV-INs are not more likely to express Oprm1.***

997 RNAscope for *Pvalb* and *Oprm1* in a total of 10 P28 mice, 2 each injected with EdU at E11, E12, E13,
998 E14 , and E15. (**A**) Representative coronal section with *Oprm1* (*red*), *Pvalb* (*green*), EdU (*magenta*), and
999 DAPI (*blue*). Highlighted sections in CA1 (E12) and V1 L2/3 (E14) expanded in (**B**), with "#" markers
1000 signifying *Pvalb*+EdU+ co-labeled cells, "&" markers signifying *Pvalb*+*Oprm1*+ co-labeled cells, and "&#"
1001 markers signifying triple labeled *Pvalb*+Edu+*Oprm1*+ cells. (**C-E**) Triple colocalization quantification
1002 across embryonic birthdate E11-15 for HPC (*left*), V1 (*middle*) and CA1+V1 combined (*right*). Each
1003 animal included 2 technical replicates, with each quantified across left and right hemispheres. (**C**) Total
1004 number of counted *Pvalb*+, *Pvalb*+Edu+, and *Pvalb*+Edu+*Oprm1*+ cells. (**D**) Fraction of *Pvalb*+ cells co-
1005 labeled with EdU. (**E**) Fraction of *Pvalb*+EdU+ cells co-labeled with *Oprm1*. Asterisks represent Tukey's
1006 *post hoc* comparisons after a significant effect of birthdate was found via 1-way ANOVA.

1007 ***Fig. S3: Additional PV-IN optogenetic experiments.***

1008 Normalized IeIPSC responses to bath administration of 100 nM DAMGO compared between (**A**) n_{cell} =
1009 12 superficial and 14 deep CA1-PCs, (**B**) n_{cell} = 27 supragranular (L2/3) and 30 infragranular (L5/6)
1010 neocortical PCs, and (**C**) sex effects across n_{cell} = 20 (male), 23 (female) CA-PCs and 20 (male), 27
1011 (female) CTX-PCs. Non-significant p-values and asterisks represent results of unpaired t-tests (*A*, *B*) and
1012 Šídák's *post hoc* comparisons (*C*) after a significant effect of region was observed via 2-way ANOVA. (**D-**
1013 **G**) Mouse IeIPSC experiments with (*top*) averaged example traces and (*bottom*) summary data for varied
1014 drug conditions. (**D**) DAMGO 1 μM: n_{cell} = 7 (CA1), 8 (DG), and 9 (M1) from n_{mice} = 5 (4F), age = P82-101
1015 (P91 ± 4). (**E**) Morphine 10 μM: n_{cell} = 9 (CA1) and 8 (S1) from n_{mice} = 3 (2F), age = P33-118 (P83 ± 26).
1016 (**F**) CTAP 500 nM: n_{cell} = 10 (CA1) and 10 (S1) from n_{mice} = 2 (1F), age = P54, 60. (**G**) Naloxone 1 μM:
1017 n_{cell} = 10 (CA1) and 9 (S1) from n_{mice} = 3 (2F), age = P55-60 (P57 ± 2). Asterisks represent Tukey's *post*
1018 *hoc* comparisons after a significant effect of treatment was found via 1-way repeated measure
1019 ANOVA/mixed model. (**H**) Baseline-normalized DAMGO response of PV-IN IeIPSCs across all drug
1020 conditions in CA1 (*left*) and CTX (*right*), combining data from *Fig. 3H,I,N,U*, (*D-G*), and *Fig. 4G*. CTX
1021 represents S1 for all conditions except DAMGO 1 μM (M1) and DPDPE (V1). Asterisks represent
1022 significant deviations from the normalized baseline via 1-sample t-test.

1023 ***Fig. S4: Validation of axo-axonic cell (AAC) specific BiPVe4 virus in rodent hippocampus.***

1024 (**A**) IHC stain with antibodies against PV (*magenta*) and Satb1 (*green*) in 1M P155 C57BL6/J mouse
1025 injected retro-orbitally with BiPVe4-tdTom (*orange*, boosted with anti-RFP). In bottom zoomed images of
1026 CA2 region, open arrows indicate single marker labeling and closed arrows co-expression by indicated
1027 markers: (*from top to bottom*) BiPVe4+ & BiPVe4+PV+, PV+ & PV+Satb1+, Satb1+ & BiPVe4+Satb1+.
1028 (**B**) Colocalization quantification of triple IHC and (**C**) cell densities. Counts performed in 2 hippocampal
1029 sections each from two mice: 1M P155 C57BL6/J injected retro-orbitally with *BiPVe4-ChR2* and 1F P69
1030 injected intra-cranially with *BiPVe4-tdTom*. (**D**) IHC stain with antibody against anti-pIκBα, labeling the
1031 axon initial segment (AIS, *cyan*) in 1F P44 injected retro-orbitally with *BiPVe4-tdTom*, showing close
1032 proximity of signals as expected from AACs. (**E**) Hippocampal section from same mouse as (*D*) after
1033 biocytin-labeling of recorded AAC (*white*). (*Right*) Intensity profile of 3 sections across CA1 layers,
1034 showing higher expression of BiPVe4 towards *oriens* side of *str. pyr.* (**F**) Schematic of whole-cell
1035 recordings of AACs illustrating membrane response to hyperpolaring/depolarizing current steps to
1036 measure intrinsic parameters (Table S2) and response to DAMGO. (**G**) Example trace showing change
1037 in holding current from DAMGO administration (rapid inward/outward currents reflect sEPSCs/sIPSCs).
1038 (**H**) Holding current summary data across baseline, DAMGO, and wash conditions for n_{cell} = 7 from 1F
1039 P44 injected intra-cranially with BiPVe4-tdTom. Asterisk represents Tukey's *post hoc* comparison after a
1040 significant effect of treatment was found via 1-way repeated measure ANOVA.

1041 ***Fig. S5: Validation of PV-IN selective Oprm1 knockout.***

1042 Double IHC with antibodies against PV (*green, top*) and μOR (*magenta, middle*) in triple transgenic mice:
1043 PV-IN selective knockout (KO) mice ($PV^{Cre/+}$:$Oprm1^{fl/fl}$, 1M P77) and wild-type (WT) littermate controls
1044 lacking Cre-recombinase ($PV^{+/+}$:$Oprm1^{fl/fl}$, 1F P77). In the CA1 region pictured, the selective PV-IN KO
1045 (*right*) exhibits reduced μOR expression in identified PV-INs relative to littermate control (*left*). Open
1046 arrows indicate identified somata for respective signal, filled arrows indicate colocalized somata.

1047 ***Fig. S6: Validation of PV-specific S5E2 virus in rhesus macaques.***

1048 (**A**) Whole-brain coronal slices of rhesus macaque injected with *pAAV(PHP.eB)-S5E2-ChR2-mCherry*
1049 (*red*) in HPC and M1, and stained for PV (*green*), to conduct colocalization analysis (*right*). (**B**) S5E2-PV
1050 colocalization quantified in 3 sections from 1F macaque, age = 11.7 years, quantified in 3 sections within
1051 each region, with (*top*) percentage of PV cells co-expressing S5E2 and vice versa, and (*bottom*) cell
1052 densities. (**C-D**) Normalized IeIPSC responses in 1M macaque, age = 15.9 years, to bath administration
1053 of (**C**) 500 nM of the N-type Ca^{2+} channel blocker ω-conotoxin in n_{cell} = 3 CA-PCs (presynaptic channels
1054 used by CCK-INs[115,116]), (**D**) 250 nM of the P/Q-type Ca^{2+} channel blocker ω-agatoxin in n_{cell} = 6 CA-PCs
1055 (presynaptic channels used by PV-INs[116]), and (**E**) 5 μM of the synthetic cannabinoid agonist WIN 55212-

1056 2 in n_{cell} =4 CA-PCs (suppresses CCK-IN synaptic release through depolarization-induced suppression
1057 of inhibition (DSI)[117]). Non-significant p-values and asterisk represent results of paired t-tests.

1058 ***Fig. S7: Additional IHC validation of Tac1^{Cre} mice as a model for immature PV-INs.***

1059 (**A-B**) Quantified intensity profiles across hippocampal CA1 layers *l.m.*, *rad.*, *pyr.* and *or.* in P5-45
1060 Tac1$^{Cre/+}$:tdTom$^{fl/+}$ mice, with distance = 0 set to *or.-pyr.* border. Intensity values for each section
1061 normalized by z-score prior to group averaging. (**A**) PV-Tac1 intensity profile average of n = 6 sections
1062 from n = 3 mice at each age (same data as example in *Fig. 6D*). (**B**) SST-Tac1 intensity profile average
1063 of n = 4 sections from n = 2 mice at each age (same data as example in *Fig. 6F*). (**C**) IHC stain for PV
1064 (*red*) in Tac1$^{Cre/+}$:ChR2$^{fl/+}$ (*green*), performed in 3 (2F) P37 mice, and (**D**) quantified in 3 sections for each
1065 mouse across HPC and S1, for (*top*) percent colocalization and (*bottom*) cell density. (**E**) IHC stain for
1066 PV in Tac1$^{Cre/+}$:μOR-mCherry mice injected perinatally with *pAAV(AAV5)-pCAG-FLEX-EGFP-WPRE*,
1067 and thus triple-labeled for μOR (*red*), Tac1 (*green*), and PV (*magenta*). Stain replicated in 4 (2F) P13
1068 juveniles and 4 (2F) P45 adults, and (**F-G**) quantified in 4 sections from each mouse, delineating
1069 Tac1+PV+ (*magenta*) and Tac1+PV- (*green*) populations (**F**) percentage of μOR-expressing cells and
1070 (**G**) μOR intensity (A.U. = arbitrary units). Asterisks represent Šidák's *post hoc* comparisons after a
1071 significant effect of cell type was found via 2-way ANOVA.

1072 ***Fig. S8: Morphological reconstructions of Tac1-INs in early development display perisomatic***
1073 ***phenotypes consistent with immature PV-INs.***

1074 Example morphological reconstructions of recorded Tac1 cells for (**A**) n_{cell} = 21 (CA1), (**B**) 3 (CA2), (**C**) 9
1075 (CA3), (**D**) 1 (DG), and (**E**) 1 (CTX), recorded in 7 (P5-11) Tac1$^{Cre/+}$:tdTom$^{fl/+}$ mice (age indicated for each
1076 in lower left). Darker processes designate dendrites and soma, while lighter processes designate axons.
1077 CA1-3 layers: *stratum oriens* (*or.*), *pyramidale* (*pyr.*), *mossy fibers (m.f.)*, *radiatum* (*rad.*), *lacunosum-*
1078 *moleculare* (*l.m.*), DG layers: *molecular* (*mol.*), *granular* (*gr.*), *hilus* (*hil.*). Cells grouped by principal axonal
1079 target: primarily targeting *str. pyr.* and *gr.* consistent with BCs (**A$_1$**, **B$_1$**, **C$_1$**, **D**), targeting both *str. or.* and
1080 *rad.* consistent with BSCs (**A$_2$**, **B$_2$**, **C$_2$**), and primarily targeting superficial dendritic layers *rad.*, *l.m.*, and/or
1081 *hil.* (**A$_3$**, **C$_3$**). All reconstructions on same scale.

1082 ***Fig. S9: Intrinsic electrophysiological analysis of Tac1-INs reveals a fast-spiking phenotype***
1083 ***consistent with immature PV-INs and distinct from PCs.***

1084 (**A**) Schematic of whole-cell current clamp recordings of PCs/Tac1-INs from Tac1$^{Cre/+}$:tdTom$^{fl/+}$ mice and
1085 PV-INs from PV-tdTom mice to characterize intrinsic parameters. (**B-C**) Representative firing of (**B**) P10
1086 PC and (**C**) P10 Tac1 cell, with gray traces showing response to range of hyperpolarizing and
1087 depolarizing current steps, and colored lines indicating maximum firing. Most hyperpolarized step =
1088 current required to take cell to -100 mV (*B*: -150 pA, *C*: -300 pA). Most depolarized step = current to take

1089 cell to maximum firing prior to depolarization block (*B*: +175 pA, *C*: +400 pA). (*Upper inset*) Single action
1090 potential (AP) on expanded time scale. All traces between cell types displayed on same scales. (*Lower*
1091 *inset*) dV/dt vs. V plot of ten successive APs to visualize AP shape differences. (**D**) Summary data for
1092 intrinsic parameters of hippocampal n_{cell} = 14 PC and 57 Tac1 cells from n_{mice} = 4 (P8-11)
1093 Tac1$^{Cre/+}$:tdTom$^{fl/+}$ mice. RMP = resting membrane potential, R_{in} = input resistance, C_{in} = input
1094 capacitance. Asterisks and non-significant p-values represent results of unpaired t-test/Mann Whitney.
1095 (**E-G**) Representative firing of (**E**) P5 Tac1, (**F**) P18 Tac1 cell, and (**G**) P118 PV cell (recorded in PV-
1096 tdTom mouse), with gray traces showing response to range of hyperpolarizing and depolarizing current
1097 steps, and colored lines indicating maximum firing. Most hyperpolarized step = current required to take
1098 cell to -80 mV (*E*: -50 pA, *F*: -100 pA, *G*: -350 pA). Most depolarized step = current to take cell to maximum
1099 firing prior to depolarization block (*E*: +175 pA, *F*: +350 pA, *G*: +550 pA). Same scales as (*B*, *C*). (**H**)
1100 Changes in select intrinsic parameters over time for both HPC and CTX Tac1 cells, plotting n_{cell} = 8 (1
1101 P5), 9 (1 P6), 9 (1 P7),14 (1 P8), 20 (1 P9), 16 (1 P10), 14 (1 P11), 3 (1M P16), 10 (1M P18), and 10 PV
1102 (1F P118, 1F P392). Linear and exponential regressions performed on Tac1 data, with R^2 values
1103 displayed, with PV data plotted for comparison.

1104 ***Fig. S10: Additional GDP experiments.***

1105 (**A**,**C**,**E**) Example traces of GDP associated currents (GDP-Is) recorded intracellularly and voltage-
1106 clamped to 0 mV in WT mice, with (**A**) 100 nM DAMGO applied for 10 min. in S1, (**C**) 500 nM DPDPE
1107 applied for 5 min. in CA3, and (**E**) 500 nM CTAP applied for 5 min. in CA3. (**B**,**D**,**F**) Summary data for
1108 GDP-I event frequency and amplitude for (**B**) n_{cell} = 13 S1-PCs from n_{mice} = 4 (P6-8), (**D**) n_{cell} = 12 CA3-
1109 PCs from n_{mice} = 3 (P6-7), and (**F**) n_{cell} = 8 CA3-PCs from n_{mice} = 4 (P7-8). (**G**) Summary data for
1110 spontaneous inhibitory currents (sIPSCs) detected between GDP-I events in n_{cell} = 17 from 6
1111 Tac1$^{Cre/+}$:ArchT$^{fl/+}$ P5-8 mice (data in *Fig. 7D-F*), quantifying (*left to right*) sIPSC frequency, amplitude,
1112 rise time, and decay time. Asterisks represent Tukey's/Dunn's *post hoc* comparisons after a significant
1113 effect of treatment was found via 1-way repeated measure ANOVA /Friedman's test.

1114 ***Table S1: Statistical details.***

1115 Statistical details including summary statistics, normality tests, hypothesis testing, and *post hoc*
1116 comparisons, detailed in individual worksheets for each figure and supplemental figure.

1117 ***Table S2: Intrinsic Parameters.***

1118 Intrinsic electrophysiological parameters recorded from 14 PCs (P8-11), 101 Tac1 cells (P5-18,
1119 delineated by subregion), 10 PV-INs (P118-392), and 14 AACs (P44).

REFERENCES

1. Le Merrer, J., Becker, J.A., Befort, K., and Kieffer, B.L. (2009). Reward processing by the opioid system in the brain. Physiol Rev *89*, 1379-1412. 10.1152/physrev.00005.2009.
2. Corder, G., Castro, D.C., Bruchas, M.R., and Scherrer, G. (2018). Endogenous and Exogenous Opioids in Pain. Annu Rev Neurosci *41*, 453-473. 10.1146/annurev-neuro-080317-061522.
3. St Marie, B., Coleman, L., Vignato, J.A., Arndt, S., and Segre, L.S. (2020). Use and Misuse of Opioid Pain Medications by Pregnant and Nonpregnant Women. Pain Manag Nurs *21*, 90-93. 10.1016/j.pmn.2019.05.002.
4. Lee, S.J., Bora, S., Austin, N.C., Westerman, A., and Henderson, J.M.T. (2020). Neurodevelopmental Outcomes of Children Born to Opioid-Dependent Mothers: A Systematic Review and Meta-Analysis. Acad Pediatr *20*, 308-318. 10.1016/j.acap.2019.11.005.
5. Nummenmaa, L., Saanijoki, T., Tuominen, L., Hirvonen, J., Tuulari, J.J., Nuutila, P., and Kalliokoski, K. (2018). μ-opioid receptor system mediates reward processing in humans. Nat Commun *9*, 1500. 10.1038/s41467-018-03848-y.
6. Contet, C., Kieffer, B.L., and Befort, K. (2004). Mu opioid receptor: a gateway to drug addiction. Curr Opin Neurobiol *14*, 370-378. 10.1016/j.conb.2004.05.005.
7. Al-Hasani, R., and Bruchas, M.R. (2011). Molecular mechanisms of opioid receptor-dependent signaling and behavior. Anesthesiology *115*, 1363-1381. 10.1097/ALN.0b013e318238bba6.
8. Valentino, R.J., and Volkow, N.D. (2018). Untangling the complexity of opioid receptor function. Neuropsychopharmacology *43*, 2514-2520. 10.1038/s41386-018-0225-3.
9. Bourinet, E., Soong, T.W., Stea, A., and Snutch, T.P. (1996). Determinants of the G protein-dependent opioid modulation of neuronal calcium channels. Proc Natl Acad Sci U S A *93*, 1486-1491. 10.1073/pnas.93.4.1486.
10. Rusin, K.I., Giovannucci, D.R., Stuenkel, E.L., and Moises, H.C. (1997). Kappa-opioid receptor activation modulates Ca2+ currents and secretion in isolated neuroendocrine nerve terminals. J Neurosci *17*, 6565-6574. 10.1523/jneurosci.17-17-06565.1997.
11. Svoboda, K.R., and Lupica, C.R. (1998). Opioid inhibition of hippocampal interneurons via modulation of potassium and hyperpolarization-activated cation (Ih) currents. J Neurosci *18*, 7084-7098. 10.1523/jneurosci.18-18-07084.1998.
12. Torrecilla, M., Marker, C.L., Cintora, S.C., Stoffel, M., Williams, J.T., and Wickman, K. (2002). G-protein-gated potassium channels containing Kir3.2 and Kir3.3 subunits mediate the acute inhibitory effects of opioids on locus ceruleus neurons. J Neurosci *22*, 4328-4334. 10.1523/jneurosci.22-11-04328.2002.
13. Torrecilla, M., Quillinan, N., Williams, J.T., and Wickman, K. (2008). Pre- and postsynaptic regulation of locus coeruleus neurons after chronic morphine treatment: a study of GIRK-knockout mice. Eur J Neurosci *28*, 618-624. 10.1111/j.1460-9568.2008.06348.x.
14. Nicoll, R.A., Siggins, G.R., Ling, N., Bloom, F.E., and Guillemin, R. (1977). Neuronal actions of endorphins and enkephalins among brain regions: a comparative microiontophoretic study. Proc Natl Acad Sci U S A *74*, 2584-2588. 10.1073/pnas.74.6.2584.
15. Lupica, C.R., Proctor, W.R., and Dunwiddie, T.V. (1992). Dissociation of mu and delta opioid receptor-mediated reductions in evoked and spontaneous synaptic inhibition in the rat hippocampus in vitro. Brain Res *593*, 226-238. 10.1016/0006-8993(92)91312-3.
16. Capogna, M., Gähwiler, B.H., and Thompson, S.M. (1993). Mechanism of mu-opioid receptor-mediated presynaptic inhibition in the rat hippocampus in vitro. J Physiol *470*, 539-558. 10.1113/jphysiol.1993.sp019874.

17. Lupica, C.R. (1995). Delta and mu enkephalins inhibit spontaneous GABA-mediated IPSCs via a cyclic AMP-independent mechanism in the rat hippocampus. J Neurosci *15*, 737-749. 10.1523/jneurosci.15-01-00737.1995.

18. Zieglgänsberger, W., French, E.D., Siggins, G.R., and Bloom, F.E. (1979). Opioid peptides may excite hippocampal pyramidal neurons by inhibiting adjacent inhibitory interneurons. Science *205*, 415-417. 10.1126/science.451610.

19. Nicoll, R.A., Alger, B.E., and Jahr, C.E. (1980). Enkephalin blocks inhibitory pathways in the vertebrate CNS. Nature *287*, 22-25. 10.1038/287022a0.

20. Madison, D.V., and Nicoll, R.A. (1988). Enkephalin hyperpolarizes interneurones in the rat hippocampus. J Physiol *398*, 123-130. 10.1113/jphysiol.1988.sp017033.

21. Glickfeld, L.L., Atallah, B.V., and Scanziani, M. (2008). Complementary modulation of somatic inhibition by opioids and cannabinoids. J Neurosci *28*, 1824-1832. 10.1523/jneurosci.4700-07.2008.

22. Shao, C., Chen, P., Chen, Q., Zhao, M., Zhang, W.N., and Yang, K. (2020). Mu opioid receptors inhibit GABA release from parvalbumin interneuron terminals onto CA1 pyramidal cells. Biochem Biophys Res Commun *522*, 1059-1062. 10.1016/j.bbrc.2019.12.013.

23. He, X.J., Patel, J., Weiss, C.E., Ma, X., Bloodgood, B.L., and Banghart, M.R. (2021). Convergent, functionally independent signaling by mu and delta opioid receptors in hippocampal parvalbumin interneurons. Elife *10*. 10.7554/eLife.69746.

24. Drake, C.T., and Milner, T.A. (2002). Mu opioid receptors are in discrete hippocampal interneuron subpopulations. Hippocampus *12*, 119-136. 10.1002/hipo.1107.

25. Stumm, R.K., Zhou, C., Schulz, S., and Höllt, V. (2004). Neuronal types expressing mu- and delta-opioid receptor mRNA in the rat hippocampal formation. J Comp Neurol *469*, 107-118. 10.1002/cne.10997.

26. Svoboda, K.R., Adams, C.E., and Lupica, C.R. (1999). Opioid receptor subtype expression defines morphologically distinct classes of hippocampal interneurons. J Neurosci *19*, 85-95. 10.1523/jneurosci.19-01-00085.1999.

27. Krook-Magnuson, E., Luu, L., Lee, S.H., Varga, C., and Soltesz, I. (2011). Ivy and neurogliaform interneurons are a major target of μ-opioid receptor modulation. J Neurosci *31*, 14861-14870. 10.1523/jneurosci.2269-11.2011.

28. George, S.R., Zastawny, R.L., Briones-Urbina, R., Cheng, R., Nguyen, T., Heiber, M., Kouvelas, A., Chan, A.S., and O'Dowd, B.F. (1994). Distinct distributions of mu, delta and kappa opioid receptor mRNA in rat brain. Biochem Biophys Res Commun *205*, 1438-1444. 10.1006/bbrc.1994.2826.

29. Mansour, A., Fox, C.A., Burke, S., Meng, F., Thompson, R.C., Akil, H., and Watson, S.J. (1994). Mu, delta, and kappa opioid receptor mRNA expression in the rat CNS: an in situ hybridization study. J Comp Neurol *350*, 412-438. 10.1002/cne.903500307.

30. Cahill, C.M., McClellan, K.A., Morinville, A., Hoffert, C., Hubatsch, D., O'Donnell, D., and Beaudet, A. (2001). Immunohistochemical distribution of delta opioid receptors in the rat central nervous system: evidence for somatodendritic labeling and antigen-specific cellular compartmentalization. J Comp Neurol *440*, 65-84. 10.1002/cne.1370.

31. Erbs, E., Faget, L., Scherrer, G., Matifas, A., Filliol, D., Vonesch, J.L., Koch, M., Kessler, P., Hentsch, D., Birling, M.C., et al. (2015). A mu-delta opioid receptor brain atlas reveals neuronal co-occurrence in subcortical networks. Brain Struct Funct *220*, 677-702. 10.1007/s00429-014-0717-9.

32. Ehrlich, A.T., Semache, M., Gross, F., Da Fonte, D.F., Runtz, L., Colley, C., Mezni, A., Le Gouill, C., Lukasheva, V., Hogue, M., et al. (2019). Biased Signaling of the Mu Opioid Receptor Revealed in Native Neurons. iScience *14*, 47-57. 10.1016/j.isci.2019.03.011.

33. Hu, H., Gan, J., and Jonas, P. (2014). Fast-spiking, parvalbumin+ GABAergic interneurons: From cellular design to microcircuit function. Science *345*, 1255263. 10.1126/science.1255263.

34. Wonders, C.P., and Anderson, S.A. (2006). The origin and specification of cortical interneurons. Nat Rev Neurosci *7*, 687-696. 10.1038/nrn1954.

35. Armstrong, C., and Soltesz, I. (2012). Basket cell dichotomy in microcircuit function. J Physiol *590*, 683-694. 10.1113/jphysiol.2011.223669.

36. Pelkey, K.A., Chittajallu, R., Craig, M.T., Tricoire, L., Wester, J.C., and McBain, C.J. (2017). Hippocampal GABAergic Inhibitory Interneurons. Physiological Reviews *97*, 1619-1747. 10.1152/physrev.00007.2017.

37. Uchigashima, M., Narushima, M., Fukaya, M., Katona, I., Kano, M., and Watanabe, M. (2007). Subcellular arrangement of molecules for 2-arachidonoyl-glycerol-mediated retrograde signaling and its physiological contribution to synaptic modulation in the striatum. J Neurosci *27*, 3663-3676. 10.1523/jneurosci.0448-07.2007.

38. Wilson, R.I., and Nicoll, R.A. (2002). Endocannabinoid signaling in the brain. Science *296*, 678-682. 10.1126/science.1063545.

39. Lee, B.R., Dalley, R., Miller, J.A., Chartrand, T., Close, J., Mann, R., Mukora, A., Ng, L., Alfiler, L., Baker, K., et al. (2023). Signature morphoelectric properties of diverse GABAergic interneurons in the human neocortex. Science *382*, eadf6484. 10.1126/science.adf6484.

40. Szegedi, V., Bakos, E., Furdan, S., Kovács, B.H., Varga, D., Erdélyi, M., Barzó, P., Szücs, A., Tamás, G., and Lamsa, K. (2023). HCN channels at the cell soma ensure the rapid electrical reactivity of fast-spiking interneurons in human neocortex. PLoS Biol *21*, e3002001. 10.1371/journal.pbio.3002001.

41. Giannopoulos, P., and Papatheodoropoulos, C. (2013). Effects of μ-opioid receptor modulation on the hippocampal network activity of sharp wave and ripples. British Journal of Pharmacology *168*, 1146-1164. 10.1111/j.1476-5381.2012.02240.x.

42. Gulyás, A.I., Szabó, G.G., Ulbert, I., Holderith, N., Monyer, H., Erdélyi, F., Szabó, G., Freund, T.F., and Hájos, N. (2010). Parvalbumin-Containing Fast-Spiking Basket Cells Generate the Field Potential Oscillations Induced by Cholinergic Receptor Activation in the Hippocampus. Journal of Neuroscience *30*, 15134-15145. 10.1523/JNEUROSCI.4104-10.2010.

43. Tricoire, L., Pelkey, K.A., Erkkila, B.E., Jeffries, B.W., Yuan, X., and McBain, C.J. (2011). A blueprint for the spatiotemporal origins of mouse hippocampal interneuron diversity. The Journal of Neuroscience: The Official Journal of the Society for Neuroscience *31*, 10948-10970. 10.1523/JNEUROSCI.0323-11.2011.

44. Sanz, E., Yang, L., Su, T., Morris, D.R., McKnight, G.S., and Amieux, P.S. (2009). Cell-type-specific isolation of ribosome-associated mRNA from complex tissues. Proc Natl Acad Sci U S A *106*, 13939-13944. 10.1073/pnas.0907143106.

45. Mahadevan, V., Peltekian, A., and McBain, C.J. (2020). Translatome Analyses Using Conditional Ribosomal Tagging in GABAergic Interneurons and Other Sparse Cell Types. Current Protocols in Neuroscience *92*, e93. 10.1002/cpns.93.

46. Mahadevan, V., Mitra, A., Zhang, Y., Yuan, X., Peltekian, A., Chittajallu, R., Esnault, C., Maric, D., Rhodes, C., Pelkey, K.A., et al. (2021). NMDARs Drive the Expression of Neuropsychiatric Disorder Risk Genes Within GABAergic Interneuron Subtypes in the Juvenile Brain. Front Mol Neurosci *14*, 712609. 10.3389/fnmol.2021.712609.

47. Butt, S.J., Fuccillo, M., Nery, S., Noctor, S., Kriegstein, A., Corbin, J.G., and Fishell, G. (2005). The temporal and spatial origins of cortical interneurons predict their physiological subtype. Neuron *48*, 591-604. 10.1016/j.neuron.2005.09.034.

48. Miyoshi, G., Butt, S.J., Takebayashi, H., and Fishell, G. (2007). Physiologically distinct temporal cohorts of cortical interneurons arise from telencephalic Olig2-expressing precursors. J Neurosci *27*, 7786-7798. 10.1523/jneurosci.1807-07.2007.

49. Harrison, C., and Traynor, J.R. (2003). The [35S]GTPgammaS binding assay: approaches and applications in pharmacology. Life Sci *74*, 489-508. 10.1016/j.lfs.2003.07.005.

50. Lee, S.-H., Marchionni, I., Bezaire, M., Varga, C., Danielson, N., Lovett-Barron, M., Losonczy, A., and Soltesz, I. (2014). Parvalbumin-Positive Basket Cells Differentiate Among Hippocampal Pyramidal Cells. Neuron *82*, 1129-1144. 10.1016/j.neuron.2014.03.034.

51. Valero, M., Cid, E., Averkin, R.G., Aguilar, J., Sanchez-Aguilera, A., Viney, T.J., Gomez-Dominguez, D., Bellistri, E., and Menéndez de la Prida, L. (2015). Determinants of different deep and superficial CA1 pyramidal cell dynamics during sharp-wave ripples. Nature Neuroscience *18*, 1281-1290. 10.1038/nn.4074.

52. Piskorowski, R.A., and Chevaleyre, V. (2013). Delta-opioid receptors mediate unique plasticity onto parvalbumin-expressing interneurons in area CA2 of the hippocampus. J Neurosci *33*, 14567-14578. 10.1523/jneurosci.0649-13.2013.

53. Loyd, D.R., and Murphy, A.Z. (2014). The neuroanatomy of sexual dimorphism in opioid analgesia. Exp Neurol *259*, 57-63. 10.1016/j.expneurol.2014.04.004.

54. Torres-Reveron, A., Williams, T.J., Chapleau, J.D., Waters, E.M., McEwen, B.S., Drake, C.T., and Milner, T.A. (2009). Ovarian steroids alter mu opioid receptor trafficking in hippocampal parvalbumin GABAergic interneurons. Exp Neurol *219*, 319-327. 10.1016/j.expneurol.2009.06.001.

55. Milner, T.A., Burstein, S.R., Marrone, G.F., Khalid, S., Gonzalez, A.D., Williams, T.J., Schierberl, K.C., Torres-Reveron, A., Gonzales, K.L., McEwen, B.S., and Waters, E.M. (2013). Stress differentially alters mu opioid receptor density and trafficking in parvalbumin-containing interneurons in the female and male rat hippocampus. Synapse *67*, 757-772. 10.1002/syn.21683.

56. Wang, Z., Bilsky, E.J., Porreca, F., and Sadée, W. (1994). Constitutive mu opioid receptor activation as a regulatory mechanism underlying narcotic tolerance and dependence. Life Sci *54*, PI339-350. 10.1016/0024-3205(94)90022-1.

57. Neilan, C.L., Akil, H., Woods, J.H., and Traynor, J.R. (1999). Constitutive activity of the delta-opioid receptor expressed in C6 glioma cells: identification of non-peptide delta-inverse agonists. Br J Pharmacol *128*, 556-562. 10.1038/sj.bjp.0702816.

58. Wang, D., Raehal, K.M., Bilsky, E.J., and Sadée, W. (2001). Inverse agonists and neutral antagonists at mu opioid receptor (MOR): possible role of basal receptor signaling in narcotic dependence. J Neurochem *77*, 1590-1600. 10.1046/j.1471-4159.2001.00362.x.

59. Shoblock, J.R., and Maidment, N.T. (2006). Constitutively active micro opioid receptors mediate the enhanced conditioned aversive effect of naloxone in morphine-dependent mice. Neuropsychopharmacology *31*, 171-177. 10.1038/sj.npp.1300782.

60. Furlanis, E., Dai, M., Leyva Garcia, B., Vergara, J., Pereira, A., Pelkey, K., Tran, T., Gorissen, B.L., Vlachos, A., Hairston, A., et al. (2024). An enhancer-AAV toolbox to target and manipulate distinct interneuron subtypes. bioRxiv, 2024.2007.2017.603924. 10.1101/2024.07.17.603924.

61. Jiang, C., Wang, X., Le, Q., Liu, P., Liu, C., Wang, Z., He, G., Zheng, P., Wang, F., and Ma, L. (2021). Morphine coordinates SST and PV interneurons in the prelimbic cortex to disinhibit pyramidal neurons and enhance reward. Mol Psychiatry *26*, 1178-1193. 10.1038/s41380-019-0480-7.

62. Vormstein-Schneider, D., Lin, J.D., Pelkey, K.A., Chittajallu, R., Guo, B., Arias-Garcia, M.A., Allaway, K., Sakopoulos, S., Schneider, G., Stevenson, O., et al. (2020). Viral manipulation of functionally distinct interneurons in mice, non-human primates and humans. Nature Neuroscience. 10.1038/s41593-020-0692-9.

63. Alcántara, S., Ferrer, I., and Soriano, E. (1993). Postnatal development of parvalbumin and calbindin D28K immunoreactivities in the cerebral cortex of the rat. Anat Embryol (Berl) *188*, 63-73. 10.1007/bf00191452.

64. Wamsley, B., Jaglin, X.H., Favuzzi, E., Quattrocolo, G., Nigro, M.J., Yusuf, N., Khodadadi-Jamayran, A., Rudy, B., and Fishell, G. (2018). Rbfox1 Mediates Cell-type-Specific Splicing in Cortical Interneurons. Neuron *100*, 846-859.e847. 10.1016/j.neuron.2018.09.026.

65. Favuzzi, E., Deogracias, R., Marques-Smith, A., Maeso, P., Jezequel, J., Exposito-Alonso, D., Balia, M., Kroon, T., Hinojosa, A.J., E, F.M., and Rico, B. (2019). Distinct molecular programs regulate synapse specificity in cortical inhibitory circuits. Science *363*, 413-417. 10.1126/science.aau8977.

66. Camp, C.R., Vlachos, A., Klöckner, C., Krey, I., Banke, T.G., Shariatzadeh, N., Ruggiero, S.M., Galer, P., Park, K.L., Caccavano, A., et al. (2023). Loss of Grin2a causes a transient delay in the electrophysiological maturation of hippocampal parvalbumin interneurons. Commun Biol *6*, 952. 10.1038/s42003-023-05298-9.

67. Mòdol, L., Moissidis, M., Selten, M., Oozeer, F., and Marín, O. (2024). Somatostatin interneurons control the timing of developmental desynchronization in cortical networks. Neuron. 10.1016/j.neuron.2024.03.014.

68. Chamberland, S., Grant, G., Machold, R., Nebet, E.R., Tian, G., Stich, J., Hanani, M., Kullander, K., and Tsien, R.W. (2024). Functional specialization of hippocampal somatostatin-expressing interneurons. Proc Natl Acad Sci U S A *121*, e2306382121. 10.1073/pnas.2306382121.

69. Pfeffer, C.K., Xue, M., He, M., Huang, Z.J., and Scanziani, M. (2013). Inhibition of inhibition in visual cortex: the logic of connections between molecularly distinct interneurons. Nature Neuroscience *16*, 1068-1076. 10.1038/nn.3446.

70. Que, L., Lukacsovich, D., Luo, W., and Földy, C. (2021). Transcriptional and morphological profiling of parvalbumin interneuron subpopulations in the mouse hippocampus. Nat Commun *12*, 108. 10.1038/s41467-020-20328-4.

71. Donato, F., Rompani, S.B., and Caroni, P. (2013). Parvalbumin-expressing basket-cell network plasticity induced by experience regulates adult learning. Nature *504*, 272-276. 10.1038/nature12866.

72. Donato, F., Chowdhury, A., Lahr, M., and Caroni, P. (2015). Early- and late-born parvalbumin basket cell subpopulations exhibiting distinct regulation and roles in learning. Neuron *85*, 770-786. 10.1016/j.neuron.2015.01.011.

73. Doischer, D., Hosp, J.A., Yanagawa, Y., Obata, K., Jonas, P., Vida, I., and Bartos, M. (2008). Postnatal differentiation of basket cells from slow to fast signaling devices. J Neurosci *28*, 12956-12968. 10.1523/jneurosci.2890-08.2008.

74. Ben-Ari, Y., Cherubini, E., Corradetti, R., and Gaiarsa, J.L. (1989). Giant synaptic potentials in immature rat CA3 hippocampal neurones. J Physiol *416*, 303-325. 10.1113/jphysiol.1989.sp017762.

75. Ben-Ari, Y. (2001). Developing networks play a similar melody. Trends Neurosci *24*, 353-360. 10.1016/s0166-2236(00)01813-0.

76. Wester, J.C., and McBain, C.J. (2016). Interneurons Differentially Contribute to Spontaneous Network Activity in the Developing Hippocampus Dependent on Their Embryonic Lineage. J Neurosci *36*, 2646-2662. 10.1523/jneurosci.4000-15.2016.

77. Bonifazi, P., Goldin, M., Picardo, M.A., Jorquera, I., Cattani, A., Bianconi, G., Represa, A., Ben-Ari, Y., and Cossart, R. (2009). GABAergic hub neurons orchestrate synchrony in developing hippocampal networks. Science *326*, 1419-1424. 10.1126/science.1175509.

78. Picardo, M.A., Guigue, P., Bonifazi, P., Batista-Brito, R., Allene, C., Ribas, A., Fishell, G., Baude, A., and Cossart, R. (2011). Pioneer GABA cells comprise a subpopulation of hub neurons in the developing hippocampus. Neuron *71*, 695-709. 10.1016/j.neuron.2011.06.018.

79. Flossmann, T., Kaas, T., Rahmati, V., Kiebel, S.J., Witte, O.W., Holthoff, K., and Kirmse, K. (2019). Somatostatin Interneurons Promote Neuronal Synchrony in the Neonatal Hippocampus. Cell Rep *26*, 3173-3182.e3175. 10.1016/j.celrep.2019.02.061.

80. Liu, J.G., and Prather, P.L. (2001). Chronic exposure to mu-opioid agonists produces constitutive activation of mu-opioid receptors in direct proportion to the efficacy of the agonist used for pretreatment. Mol Pharmacol *60*, 53-62. 10.1124/mol.60.1.53.

81. Meye, F.J., van Zessen, R., Smidt, M.P., Adan, R.A., and Ramakers, G.M. (2012). Morphine withdrawal enhances constitutive μ-opioid receptor activity in the ventral tegmental area. J Neurosci *32*, 16120-16128. 10.1523/jneurosci.1572-12.2012.

82. Basheer, R., and Tempel, A. (1993). Morphine-induced reciprocal alterations in G alpha s and opioid peptide mRNA levels in discrete brain regions. J Neurosci Res *36*, 551-557. 10.1002/jnr.490360507.

83. Taki, K., Kaneko, T., and Mizuno, N. (2000). A group of cortical interneurons expressing μ-opioid receptor-like immunoreactivity: a double immunofluorescence study in the rat cerebral cortex. Neuroscience *98*, 221-231. 10.1016/s0306-4522(00)00124-x.

84. Blasco-Ibáñez, J.M., Martínez-Guijarro, F.J., and Freund, T.F. (1998). Enkephalin-containing interneurons are specialized to innervate other interneurons in the hippocampal CA1 region of the rat and guinea-pig. Eur J Neurosci *10*, 1784-1795. 10.1046/j.1460-9568.1998.00190.x.

85. Leroy, F., de Solis, C.A., Boyle, L.M., Bock, T., Lofaro, O.M., Buss, E.W., Asok, A., Kandel, E.R., and Siegelbaum, S.A. (2021). Enkephalin release from VIP interneurons in the hippocampal CA2/3a region mediates heterosynaptic plasticity and social memory. Mol Psychiatry. 10.1038/s41380-021-01124-y.

86. Gurgenidze, S., Bäuerle, P., Schmitz, D., Vida, I., Gloveli, T., and Dugladze, T. (2022). Cell-Type Specific Inhibition Controls the High-Frequency Oscillations in the Medial Entorhinal Cortex. Int J Mol Sci *23*. 10.3390/ijms232214087.

87. Witkowski, G., and Szulczyk, P. (2006). Opioid mu receptor activation inhibits sodium currents in prefrontal cortical neurons via a protein kinase A- and C-dependent mechanism. Brain Res *1094*, 92-106. 10.1016/j.brainres.2006.03.119.

88. Yokota, E., Koyanagi, Y., Yamamoto, K., Oi, Y., Koshikawa, N., and Kobayashi, M. (2016). Opioid subtype- and cell-type-dependent regulation of inhibitory synaptic transmission in the rat insular cortex. Neuroscience *339*, 478-490. 10.1016/j.neuroscience.2016.10.004.

89. Lau, B.K., Ambrose, B.P., Thomas, C.S., Qiao, M., and Borgland, S.L. (2020). Mu-Opioids Suppress GABAergic Synaptic Transmission onto Orbitofrontal Cortex Pyramidal Neurons with Subregional Selectivity. J Neurosci *40*, 5894-5907. 10.1523/jneurosci.2049-19.2020.

90. Preuss, T.M., and Wise, S.P. (2022). Evolution of prefrontal cortex. Neuropsychopharmacology *47*, 3-19. 10.1038/s41386-021-01076-5.

91. Cossart, R., and Khazipov, R. (2021). How development sculpts hippocampal circuits and function. Physiol Rev. 10.1152/physrev.00044.2020.

92. Xie, C.W., and Lewis, D.V. (1991). Opioid-mediated facilitation of long-term potentiation at the lateral perforant path-dentate granule cell synapse. J Pharmacol Exp Ther *256*, 289-296.

93. Bramham, C.R., and Sarvey, J.M. (1996). Endogenous activation of mu and delta-1 opioid receptors is required for long-term potentiation induction in the lateral perforant path: dependence on GABAergic inhibition. J Neurosci *16*, 8123-8131. 10.1523/jneurosci.16-24-08123.1996.

94. Mansouri, F.A., Motamedi, F., Fathollahi, Y., Atapour, N., and Semnanian, S. (1997). Augmentation of LTP induced by primed-bursts tetanic stimulation in hippocampal CA1 area of morphine dependent rats. Brain Res *769*, 119-124. 10.1016/s0006-8993(97)00608-2.

95. Pu, L., Bao, G.B., Xu, N.J., Ma, L., and Pei, G. (2002). Hippocampal long-term potentiation is reduced by chronic opiate treatment and can be restored by re-exposure to opiates. J Neurosci *22*, 1914-1921. 10.1523/jneurosci.22-05-01914.2002.

96. McQuiston, A.R. (2008). Layer selective presynaptic modulation of excitatory inputs to hippocampal cornu Ammon 1 by mu-opioid receptor activation. Neuroscience *151*, 209-221. 10.1016/j.neuroscience.2007.09.077.

97. Valero, M., Navas-Olive, A., de la Prida, L.M., and Buzsáki, G. (2022). Inhibitory conductance controls place field dynamics in the hippocampus. Cell Rep *40*, 111232. 10.1016/j.celrep.2022.111232.

98. Sun, Y., and Giocomo, L.M. (2022). Neural circuit dynamics of drug-context associative learning in the mouse hippocampus. Nat Commun *13*, 6721. 10.1038/s41467-022-34114-x.

99. Oh, S.W., Harris, J.A., Ng, L., Winslow, B., Cain, N., Mihalas, S., Wang, Q., Lau, C., Kuan, L., Henry, A.M., et al. (2014). A mesoscale connectome of the mouse brain. Nature *508*, 207-214. 10.1038/nature13186.

100. Hippenmeyer, S., Vrieseling, E., Sigrist, M., Portmann, T., Laengle, C., Ladle, D.R., and Arber, S. (2005). A developmental switch in the response of DRG neurons to ETS transcription factor signaling. PLoS biology *3*, e159. 10.1371/journal.pbio.0030159.

101. Taniguchi, H., He, M., Wu, P., Kim, S., Paik, R., Sugino, K., Kvitsiani, D., Kvitsani, D., Fu, Y., Lu, J., et al. (2011). A resource of Cre driver lines for genetic targeting of GABAergic neurons in cerebral cortex. Neuron *71*, 995-1013. 10.1016/j.neuron.2011.07.026.

102. Harris, J.A., Hirokawa, K.E., Sorensen, S.A., Gu, H., Mills, M., Ng, L.L., Bohn, P., Mortrud, M., Ouellette, B., Kidney, J., et al. (2014). Anatomical characterization of Cre driver mice for neural circuit mapping and manipulation. Front Neural Circuits *8*, 76. 10.3389/fncir.2014.00076.

103. Xu, Q., Tam, M., and Anderson, S.A. (2008). Fate mapping Nkx2.1-lineage cells in the mouse telencephalon. J Comp Neurol *506*, 16-29. 10.1002/cne.21529.

104. Monory, K., Massa, F., Egertová, M., Eder, M., Blaudzun, H., Westenbroek, R., Kelsch, W., Jacob, W., Marsch, R., Ekker, M., et al. (2006). The endocannabinoid system controls key epileptogenic circuits in the hippocampus. Neuron *51*, 455-466. 10.1016/j.neuron.2006.07.006.

105. Madisen, L., Zwingman, T.A., Sunkin, S.M., Oh, S.W., Zariwala, H.A., Gu, H., Ng, L.L., Palmiter, R.D., Hawrylycz, M.J., Jones, A.R., et al. (2010). A robust and high-throughput Cre reporting and characterization system for the whole mouse brain. Nature Neuroscience *13*, 133-140. 10.1038/nn.2467.

106. Madisen, L., Mao, T., Koch, H., Zhuo, J.M., Berenyi, A., Fujisawa, S., Hsu, Y.W., Garcia, A.J., 3rd, Gu, X., Zanella, S., et al. (2012). A toolbox of Cre-dependent optogenetic transgenic mice for light-induced activation and silencing. Nat Neurosci *15*, 793-802. 10.1038/nn.3078.

107. Daigle, T.L., Madisen, L., Hage, T.A., Valley, M.T., Knoblich, U., Larsen, R.S., Takeno, M.M., Huang, L., Gu, H., Larsen, R., et al. (2018). A Suite of Transgenic Driver and Reporter Mouse Lines with Enhanced Brain-Cell-Type Targeting and Functionality. Cell *174*, 465-480.e422. 10.1016/j.cell.2018.06.035.

108. Luo, C., Keown, C.L., Kurihara, L., Zhou, J., He, Y., Li, J., Castanon, R., Lucero, J., Nery, J.R., Sandoval, J.P., et al. (2017). Single-cell methylomes identify neuronal subtypes and regulatory elements in mammalian cortex. Science *357*, 600-604. 10.1126/science.aan3351.

109. Love, M.I., Huber, W., and Anders, S. (2014). Moderated estimation of fold change and dispersion for RNA-seq data with DESeq2. Genome Biol *15*, 550. 10.1186/s13059-014-0550-8.

110. Fredericks, J.M., Dash, K.E., Jaskot, E.M., Bennett, T.W., Lerchner, W., Dold, G., Ide, D., Cummins, A.C., Der Minassian, V.H., Turchi, J.N., et al. (2020). Methods for mechanical delivery of viral vectors into rhesus monkey brain. J Neurosci Methods *339*, 108730. 10.1016/j.jneumeth.2020.108730.

111. Valentino, R.J., and Dingledine, R. (1982). Pharmacological characterization of opioid effects in the rat hippocampal slice. J Pharmacol Exp Ther *223*, 502-509.

112. Verheugen, J.A., Fricker, D., and Miles, R. (1999). Noninvasive measurements of the membrane potential and GABAergic action in hippocampal interneurons. J Neurosci *19*, 2546-2555. 10.1523/jneurosci.19-07-02546.1999.

113. Allaway, K.C., Gabitto, M.I., Wapinski, O., Saldi, G., Wang, C.Y., Bandler, R.C., Wu, S.J., Bonneau, R., and Fishell, G. (2021). Genetic and epigenetic coordination of cortical interneuron development. Nature *597*, 693-697. 10.1038/s41586-021-03933-1.

114. Wu, S.J., Dai, M., Yang, S.P., McCann, C., Qiu, Y., Marrero, G.J., Stogsdill, J.A., Di Bella, D.J., Xu, Q., Farhi, S.L., et al. (2024). Pyramidal neurons proportionately alter the identity and survival of specific cortical interneuron subtypes. Res Sq. 10.21203/rs.3.rs-4774421/v1.

115. Wilson, R.I., Kunos, G., and Nicoll, R.A. (2001). Presynaptic specificity of endocannabinoid signaling in the hippocampus. Neuron *31*, 453-462. 10.1016/s0896-6273(01)00372-5.

116. Hefft, S., and Jonas, P. (2005). Asynchronous GABA release generates long-lasting inhibition at a hippocampal interneuron-principal neuron synapse. Nat Neurosci *8*, 1319-1328. 10.1038/nn1542.

117. Wilson, R.I., and Nicoll, R.A. (2001). Endogenous cannabinoids mediate retrograde signalling at hippocampal synapses. Nature *410*, 588-592. 10.1038/35069076.

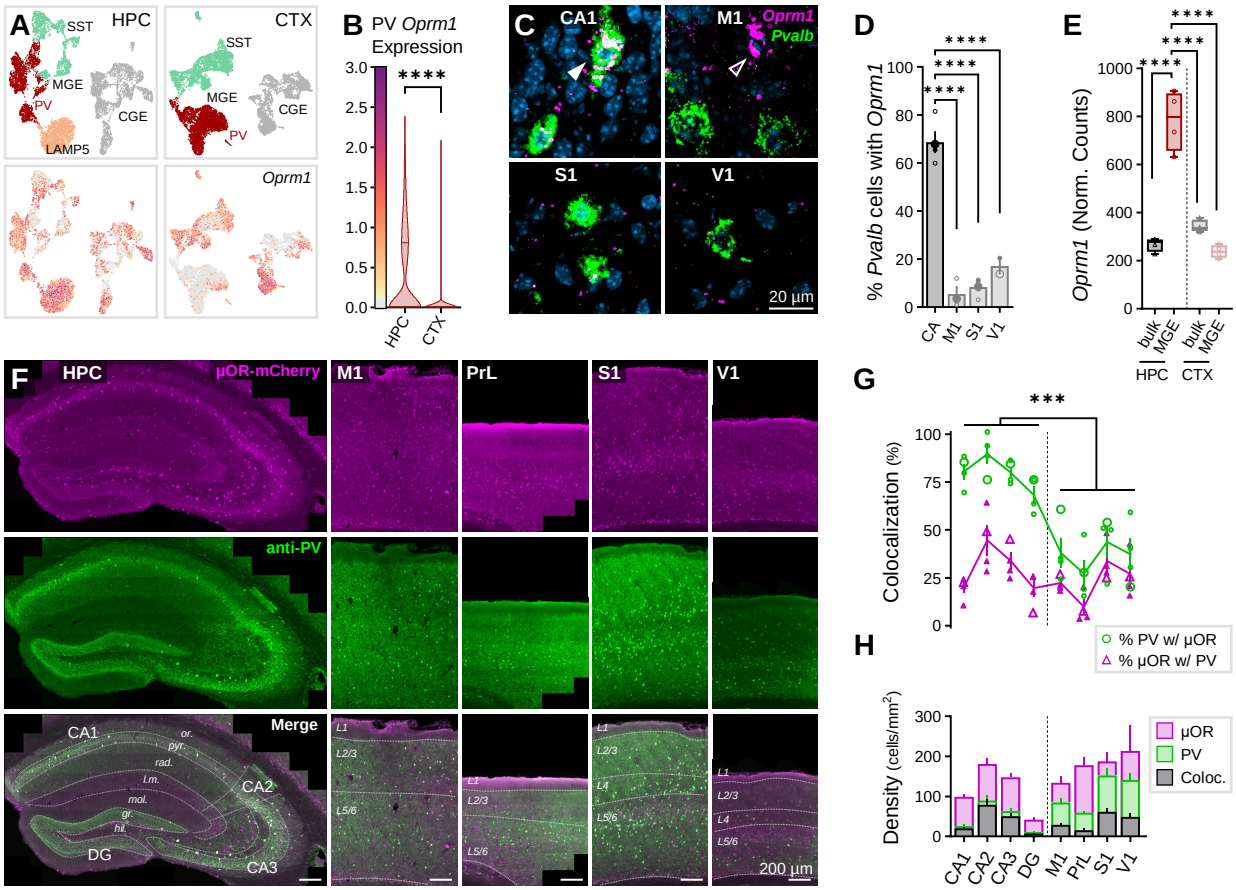
A
HPC
CTX
SST
MGE
CGE
PV
LAMP5
Oprm1
B
PV Oprm1 Expression
****
HPC
CTX
C
CA1
M1
S1
V1
Oprm1
Pvalb
20 µm
D
% Pvalb cells with Oprm1
CA
M1
S1
V1
E
Oprm1 (Norm. Counts)
bulk
MGE
HPC
CTX
F
HPC
µOR-mCherry
M1
PrL
S1
V1
anti-PV
Merge
CA1
CA2
CA3
DG
200 µm
G
Colocalization (%)
***
% PV w/ µOR
% µOR w/ PV
H
Density (cells/mm²)
µOR
PV
Coloc.
CA1
CA2
CA3
DG
M1
PrL
S1
V1

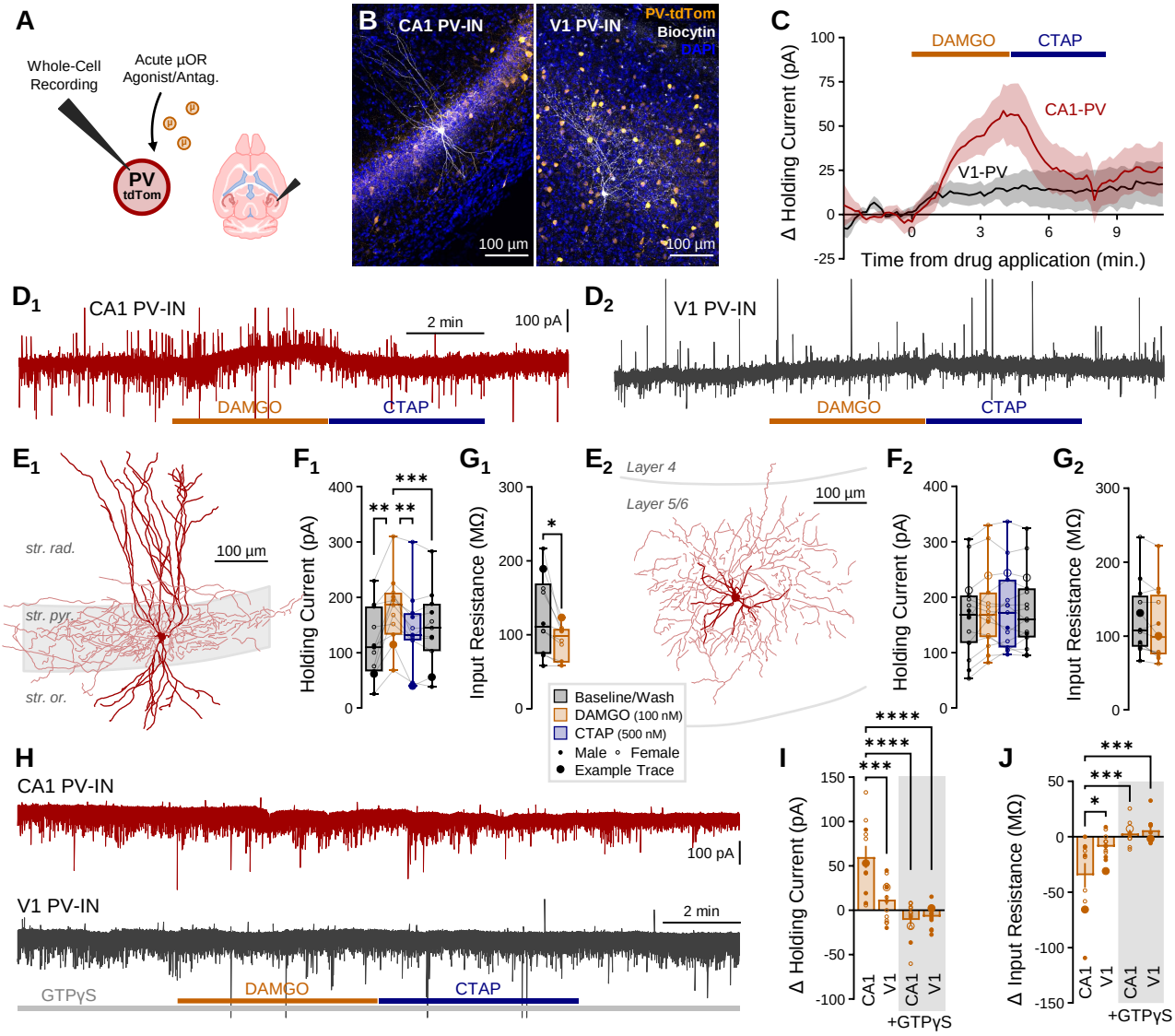
A
Whole-Cell Recording
Acute μOR Agonist/Antag.
PV tdTom
B
CA1 PV-IN
V1 PV-IN
PV-tdTom
Biocytin
DAPI
100 μm
C
DAMGO
CTAP
CA1-PV
V1-PV
Δ Holding Current (pA)
Time from drug application (min.)
D1
CA1 PV-IN
2 min
100 pA
D2
V1 PV-IN
E1
str. rad.
str. pyr.
str. or.
E2
Layer 4
Layer 5/6
F1
F2
Holding Current (pA)
G1
G2
Input Resistance (MΩ)
Baseline/Wash
DAMGO (100 nM)
CTAP (500 nM)
Male
Female
Example Trace
H
GTPγS
I
Δ Holding Current (pA)
CA1
V1
+GTPγS
J
Δ Input Resistance (MΩ)

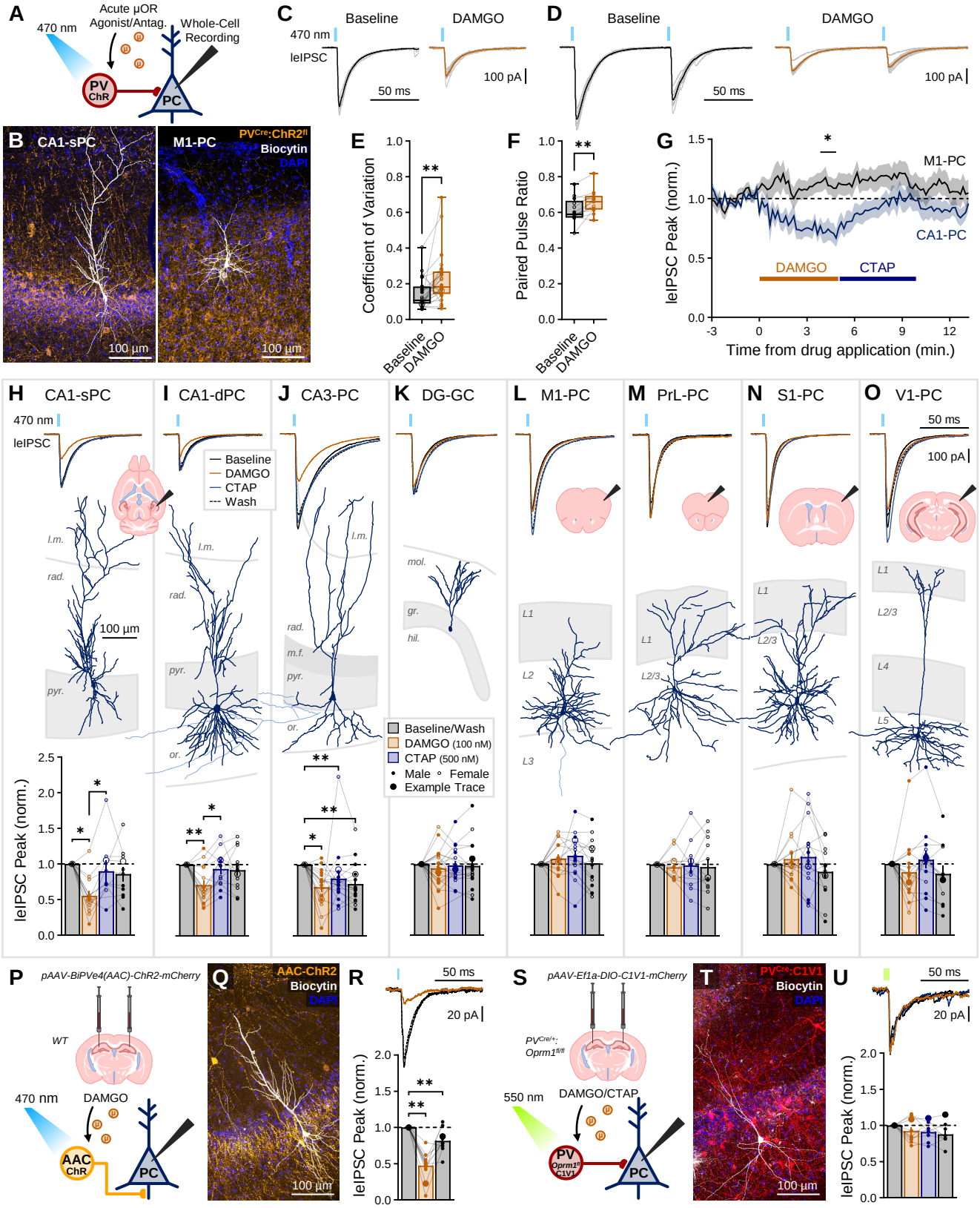
A
470 nm
Acute μOR Agonist/Antag.
Whole-Cell Recording
PV ChR
PC
B
CA1-sPC
M1-PC
PVCre:ChR2fl
Biocytin
DAPI
100 μm
C
Baseline
DAMGO
470 nm
IeIPSC
50 ms
100 pA
D
E
Coefficient of Variation
Baseline
DAMGO
F
Paired Pulse Ratio
G
IeIPSC Peak (norm.)
M1-PC
CA1-PC
DAMGO
CTAP
Time from drug application (min.)
H CA1-sPC
I CA1-dPC
J CA3-PC
K DG-GC
L M1-PC
M PrL-PC
N S1-PC
O V1-PC
Baseline
DAMGO
CTAP
Wash
Baseline/Wash
DAMGO (100 nM)
CTAP (500 nM)
Male
Female
Example Trace
P
pAAV-BiPVe4(AAC)-ChR2-mCherry
WT
470 nm
DAMGO
AAC ChR
PC
Q
AAC-ChR2
R
S
pAAV-Ef1a-DIO-C1V1-mCherry
PVCre/+:Oprm1fl/fl
550 nm
DAMGO/CTAP
PV Oprm1fl C1V1
T
PVCre:C1V1
U

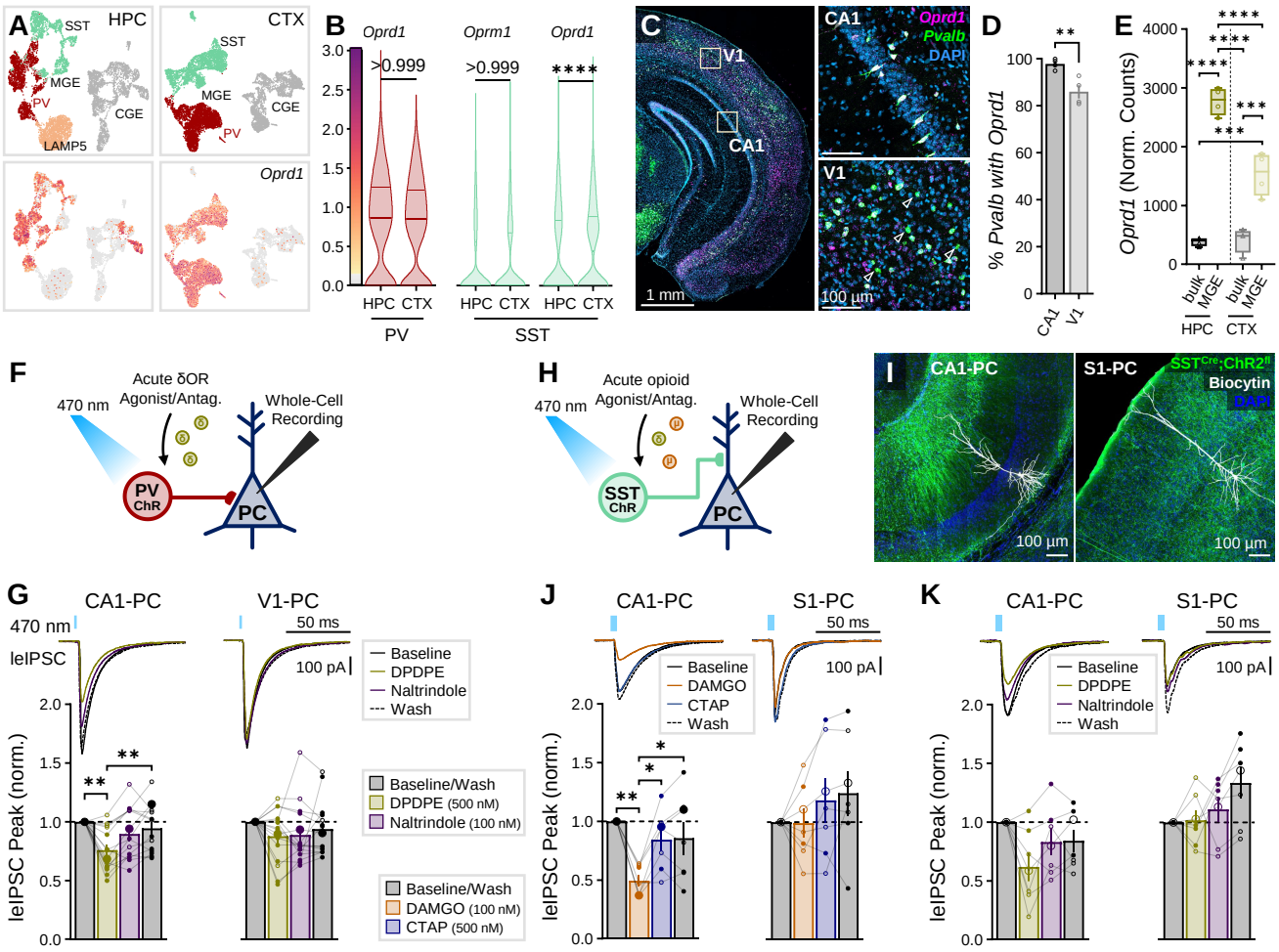
A
HPC
CTX
SST
MGE
CGE
PV
LAMP5
Oprd1
B
Oprd1
Oprm1
Oprd1
>0.999
>0.999
****
HPC CTX HPC CTX HPC CTX
PV
SST
C
V1
CA1
1 mm
Oprd1
Pvalb
DAPI
100 µm
D
% Pvalb with Oprd1
CA1
V1
E
Oprd1 (Norm. Counts)
bulk MGE bulk MGE
HPC CTX
F
470 nm
Acute δOR Agonist/Antag.
Whole-Cell Recording
PV ChR
PC
H
470 nm
Acute opioid Agonist/Antag.
Whole-Cell Recording
SST ChR
PC
I
CA1-PC
S1-PC
SST^Cre;ChR2^fl
Biocytin
DAPI
100 µm
G
CA1-PC
V1-PC
470 nm
IeIPSC
50 ms
100 pA
Baseline
DPDPE
Naltrindole
Wash
IeIPSC Peak (norm.)
Baseline/Wash
DPDPE (500 nM)
Naltrindole (100 nM)
Baseline/Wash
DAMGO (100 nM)
CTAP (500 nM)
J
CA1-PC
S1-PC
Baseline
DAMGO
CTAP
Wash
K
CA1-PC
S1-PC
Baseline
DPDPE
Naltrindole
Wash

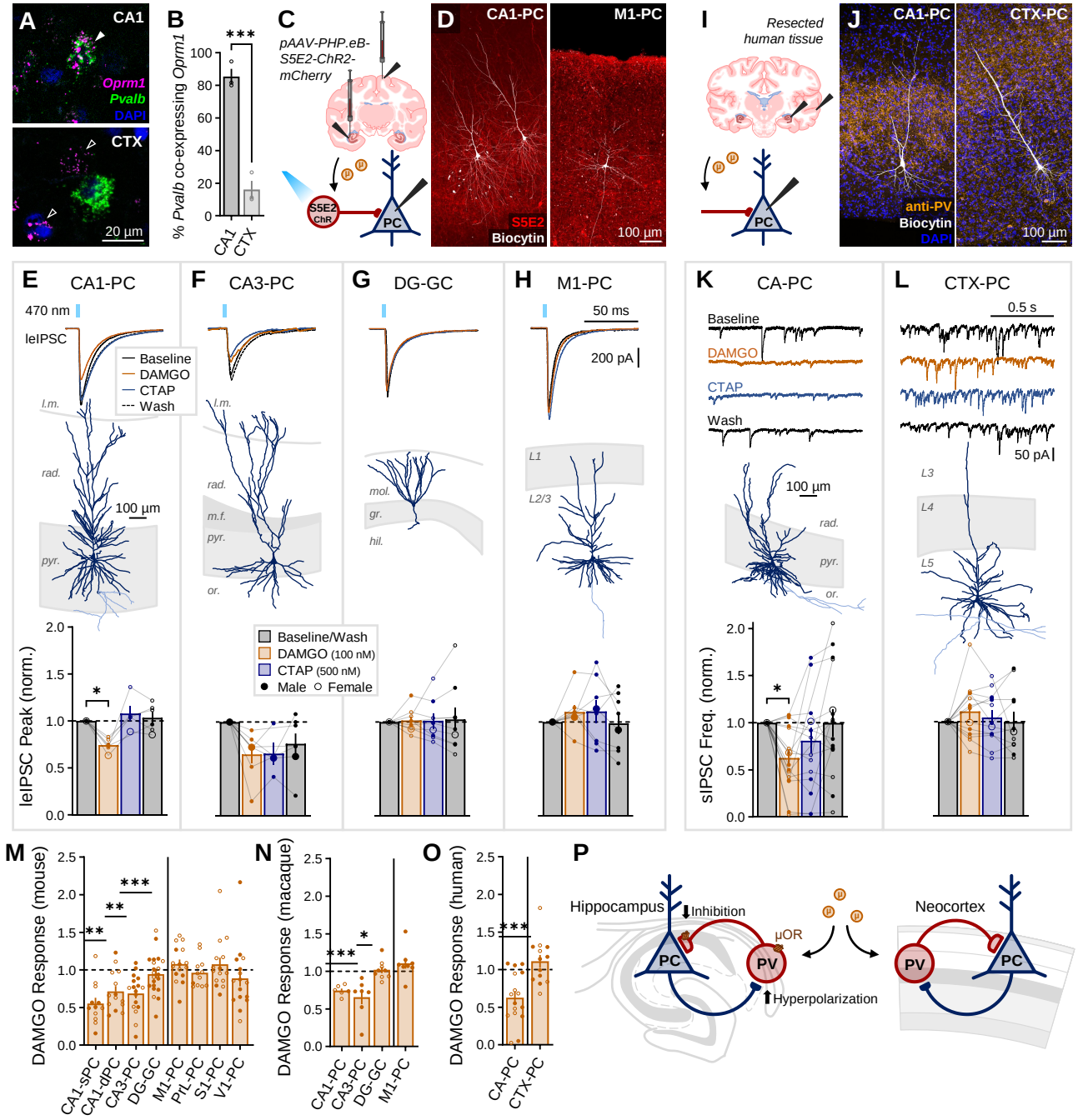
A
CA1
Oprm1
Pvalb
DAPI
CTX
20 µm
B
% Pvalb co-expressing Oprm1
***
CA1
CTX
C
pAAV-PHP.eB-S5E2-ChR2-mCherry
S5E2 ChR
PC
D
CA1-PC
M1-PC
S5E2
Biocytin
100 µm
I
Resected human tissue
PC
J
CA1-PC
CTX-PC
anti-PV
Biocytin
DAPI
100 µm
E CA1-PC
470 nm
IeIPSC
Baseline
DAMGO
CTAP
Wash
l.m.
rad.
pyr.
100 µm
IeIPSC Peak (norm.)
F CA3-PC
l.m.
rad.
m.f.
pyr.
or.
Baseline/Wash
DAMGO (100 nM)
CTAP (500 nM)
Male
Female
G DG-GC
mol.
gr.
hil.
H M1-PC
50 ms
200 pA
L1
L2/3
K CA-PC
Baseline
DAMGO
CTAP
Wash
100 µm
rad.
pyr.
or.
sIPSC Freq. (norm.)
L CTX-PC
0.5 s
50 pA
L3
L4
L5
M
DAMGO Response (mouse)
CA1-sPC
CA1-dPC
CA3-PC
DG-GC
M1-PC
PrL-PC
S1-PC
V1-PC
N
DAMGO Response (macaque)
CA1-PC
CA3-PC
DG-GC
M1-PC
O
DAMGO Response (human)
CA-PC
CTX-PC
P
Hippocampus
Inhibition
PC
PV
µOR
Hyperpolarization
Neocortex
PV
PC

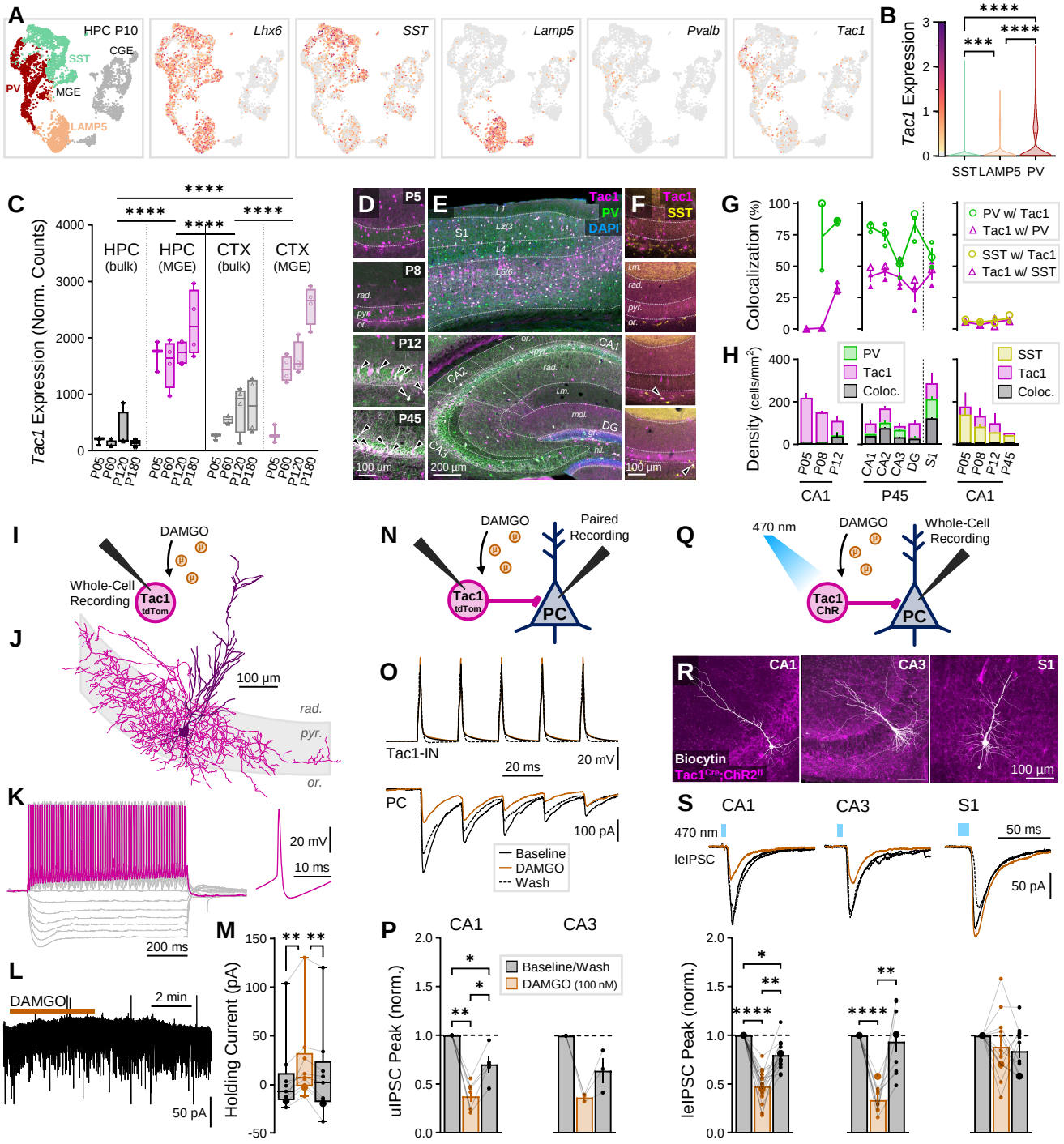
A
HPC P10
CGE
SST
PV
MGE
LAMP5
Lhx6
SST
Lamp5
Pvalb
Tac1
B
Tac1 Expression
SST LAMP5 PV
C
Tac1 Expression (Norm. Counts)
HPC (bulk)
HPC (MGE)
CTX (bulk)
CTX (MGE)
P05 P08 P12 P18
D
P5
P8
P12
P45
E
Tac1
PV
DAPI
F
Tac1
SST
G
Colocalization (%)
PV w/ Tac1
Tac1 w/ PV
SST w/ Tac1
Tac1 w/ SST
H
Density (cells/mm²)
PV
Tac1
Coloc.
SST
CA1
P45
I
DAMGO
Whole-Cell Recording
Tac1 tdTom
J
100 µm
rad.
pyr.
or.
K
20 mV
10 ms
200 ms
L
DAMGO
2 min
50 pA
M
Holding Current (pA)
N
DAMGO
Paired Recording
Tac1 tdTom
PC
O
Tac1-IN
20 ms
20 mV
PC
100 pA
Baseline
DAMGO
Wash
P
CA1
CA3
uIPSC Peak (norm.)
Baseline/Wash
DAMGO (100 nM)
Q
470 nm
DAMGO
Whole-Cell Recording
Tac1 ChR
PC
R
CA1
CA3
S1
Biocytin
Tac1Cre:ChR2fl
100 µm
S
CA1
CA3
S1
470 nm
IeIPSC
50 ms
50 pA
IeIPSC Peak (norm.)

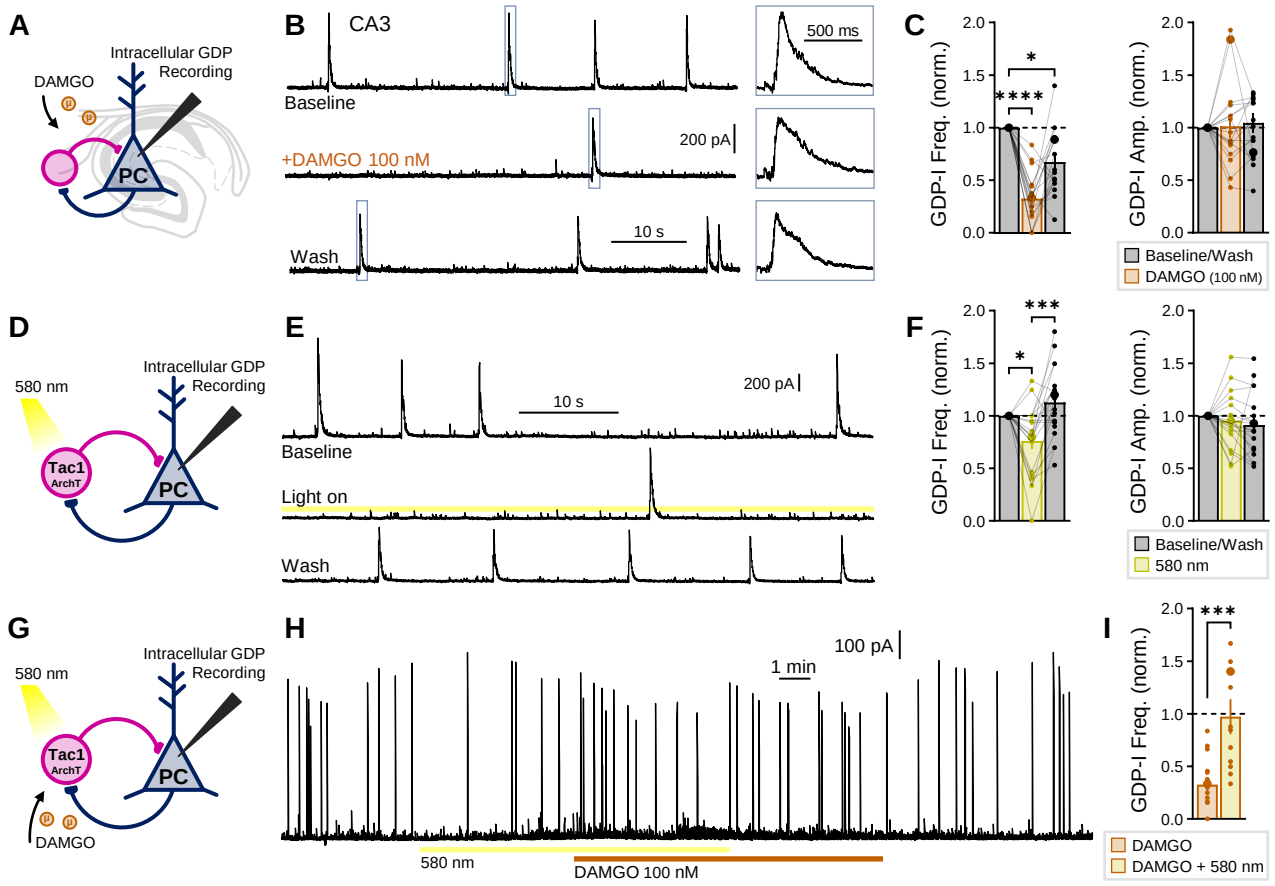
A
Intracellular GDP Recording
DAMGO
PC
B
CA3
Baseline
+DAMGO 100 nM
Wash
500 ms
200 pA
10 s
C
GDP-I Freq. (norm.)
GDP-I Amp. (norm.)
Baseline/Wash
DAMGO (100 nM)
D
580 nm
Intracellular GDP Recording
Tac1
ArchT
PC
E
10 s
200 pA
Baseline
Light on
Wash
F
GDP-I Freq. (norm.)
GDP-I Amp. (norm.)
Baseline/Wash
580 nm
G
580 nm
Intracellular GDP Recording
Tac1
ArchT
PC
DAMGO
H
100 pA
1 min
580 nm
DAMGO 100 nM
I
GDP-I Freq. (norm.)
DAMGO
DAMGO + 580 nm

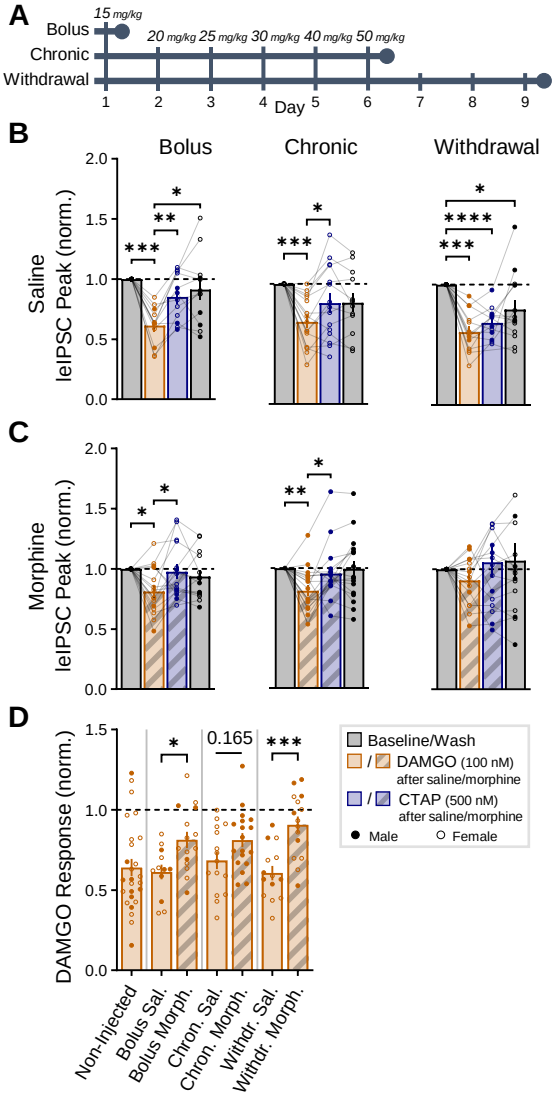
A
Bolus
Chronic
Withdrawal
15 mg/kg
20 mg/kg
25 mg/kg
30 mg/kg
40 mg/kg
50 mg/kg
1
2
3
4
5
6
7
8
9
Day
B
Bolus
Chronic
Withdrawal
Saline
IeIPSC Peak (norm.)
2.0
1.5
1.0
0.5
0.0
***
**
*
***
*
***
****
*
C
Morphine
IeIPSC Peak (norm.)
2.0
1.5
1.0
0.5
0.0
*
*
**
*
D
DAMGO Response (norm.)
1.5
1.0
0.5
0.0
*
0.165
***
Non-Injected
Bolus Sal.
Bolus Morph.
Chron. Sal.
Chron. Morph.
Withdr. Sal.
Withdr. Morph.
Baseline/Wash
/ DAMGO (100 nM)
after saline/morphine
/ CTAP (500 nM)
after saline/morphine
Male
Female

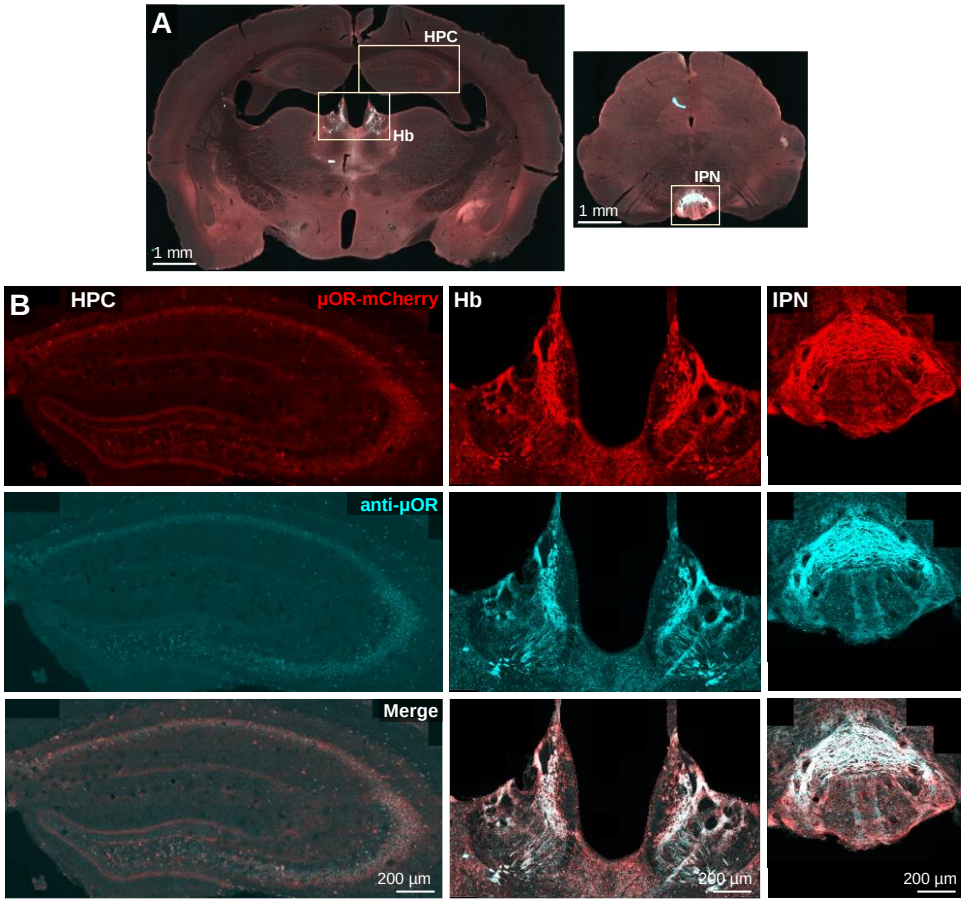
A
HPC
Hb
1 mm
IPN
1 mm
B
HPC
μOR-mCherry
Hb
IPN
anti-μOR
Merge
200 μm
200 μm
200 μm

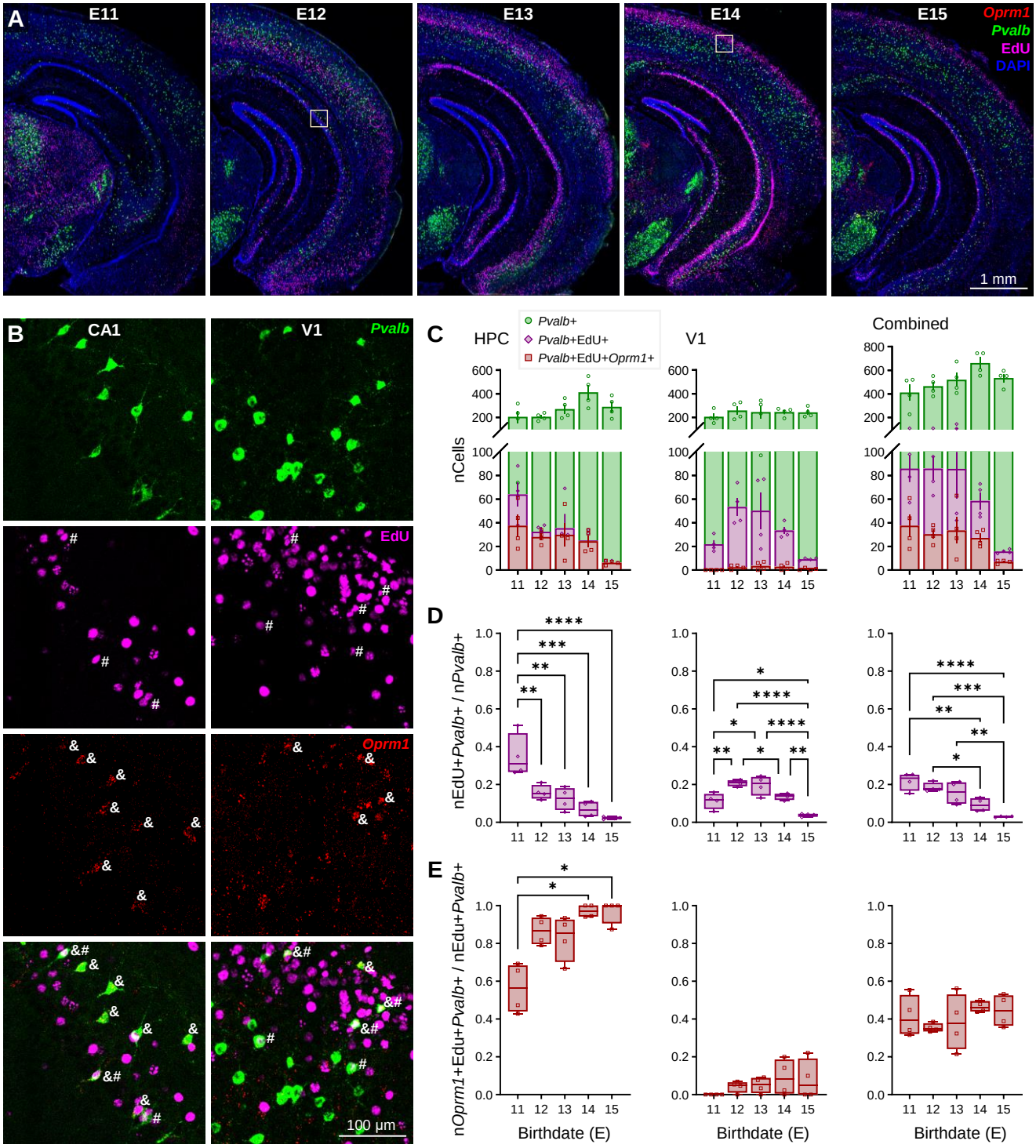
A
E11
E12
E13
E14
E15
Oprm1
Pvalb
EdU
DAPI
1 mm
B
CA1
V1
Pvalb
EdU
Oprm1
100 µm
C
HPC
V1
Combined
Pvalb+
Pvalb+EdU+
Pvalb+EdU+Oprm1+
nCells
D
nEdU+Pvalb+ / nPvalb+
E
nOprm1+Edu+Pvalb+ / nEdu+Pvalb+
Birthdate (E)

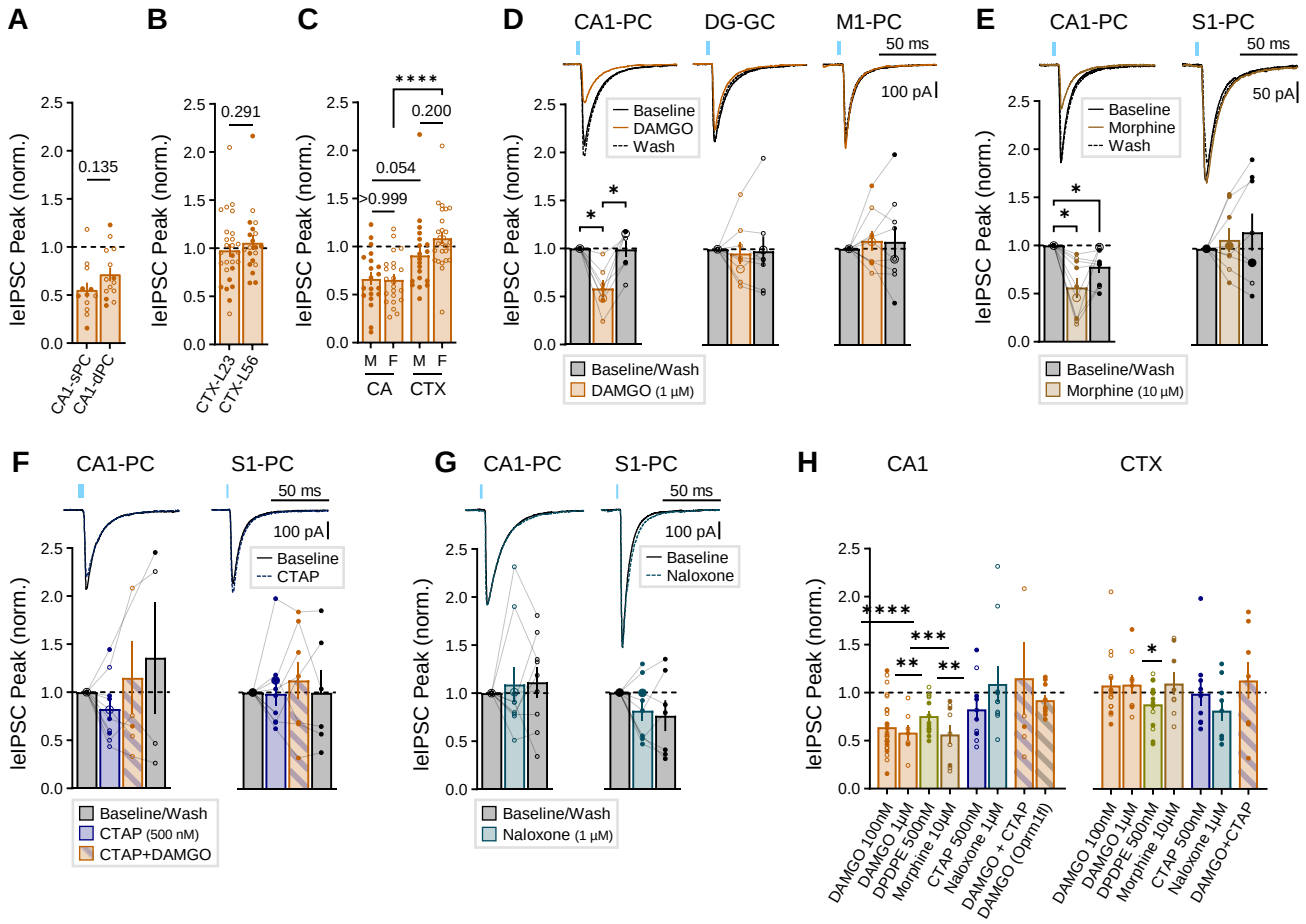
A
B
C
D
E
F
G
H
IeIPSC Peak (norm.)
0.135
CA1-sPC
CA1-dPC
0.291
CTX-L23
CTX-L56
****
0.200
0.054
>0.999
M F M F
CA CTX
CA1-PC
DG-GC
M1-PC
50 ms
100 pA
Baseline
DAMGO
Wash
Baseline/Wash
DAMGO (1 μM)
S1-PC
50 pA
Morphine
Morphine (10 μM)
CTAP
CTAP (500 nM)
CTAP+DAMGO
Naloxone
Naloxone (1 μM)
CA1
CTX
DAMGO 100nM
DAMGO 1μM
DPDPE 500nM
Morphine 10μM
CTAP 500nM
Naloxone 1μM
DAMGO + CTAP
DAMGO (Oprm1fl)
DAMGO+CTAP

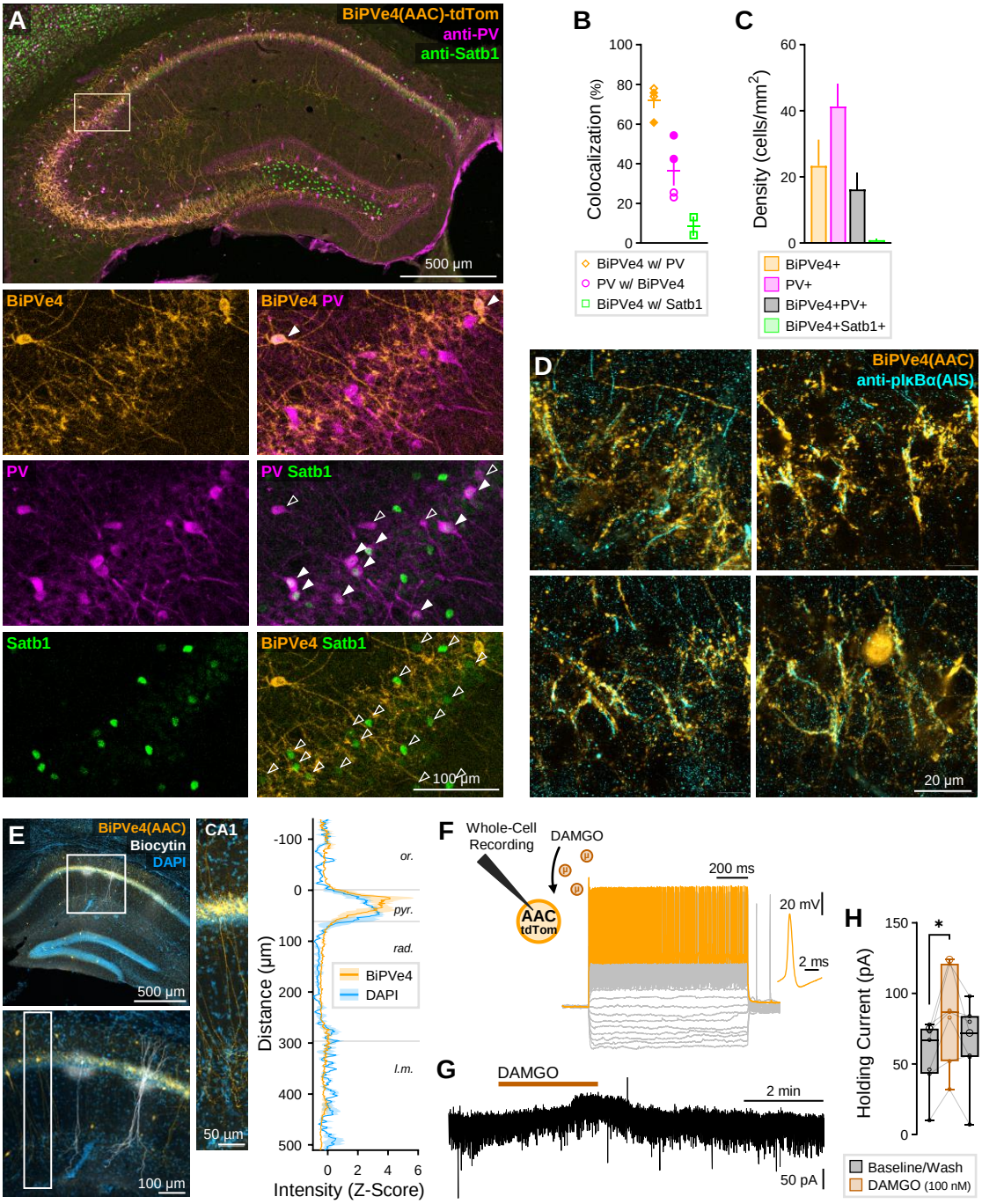
A
BiPVe4(AAC)-tdTom
anti-PV
anti-Satb1
500 µm
BiPVe4
BiPVe4 PV
PV
PV Satb1
Satb1
BiPVe4 Satb1
100 µm
B
Colocalization (%)
BiPVe4 w/ PV
PV w/ BiPVe4
BiPVe4 w/ Satb1
C
Density (cells/mm2)
BiPVe4+
PV+
BiPVe4+PV+
BiPVe4+Satb1+
D
BiPVe4(AAC)
anti-pIκBα(AIS)
20 µm
E
BiPVe4(AAC)
Biocytin
DAPI
500 µm
100 µm
CA1
50 µm
Distance (µm)
or.
pyr.
rad.
l.m.
BiPVe4
DAPI
Intensity (Z-Score)
F
Whole-Cell Recording
DAMGO
AAC tdTom
200 ms
20 mV
2 ms
G
DAMGO
2 min
50 pA
H
Holding Current (pA)
Baseline/Wash
DAMGO (100 nM)

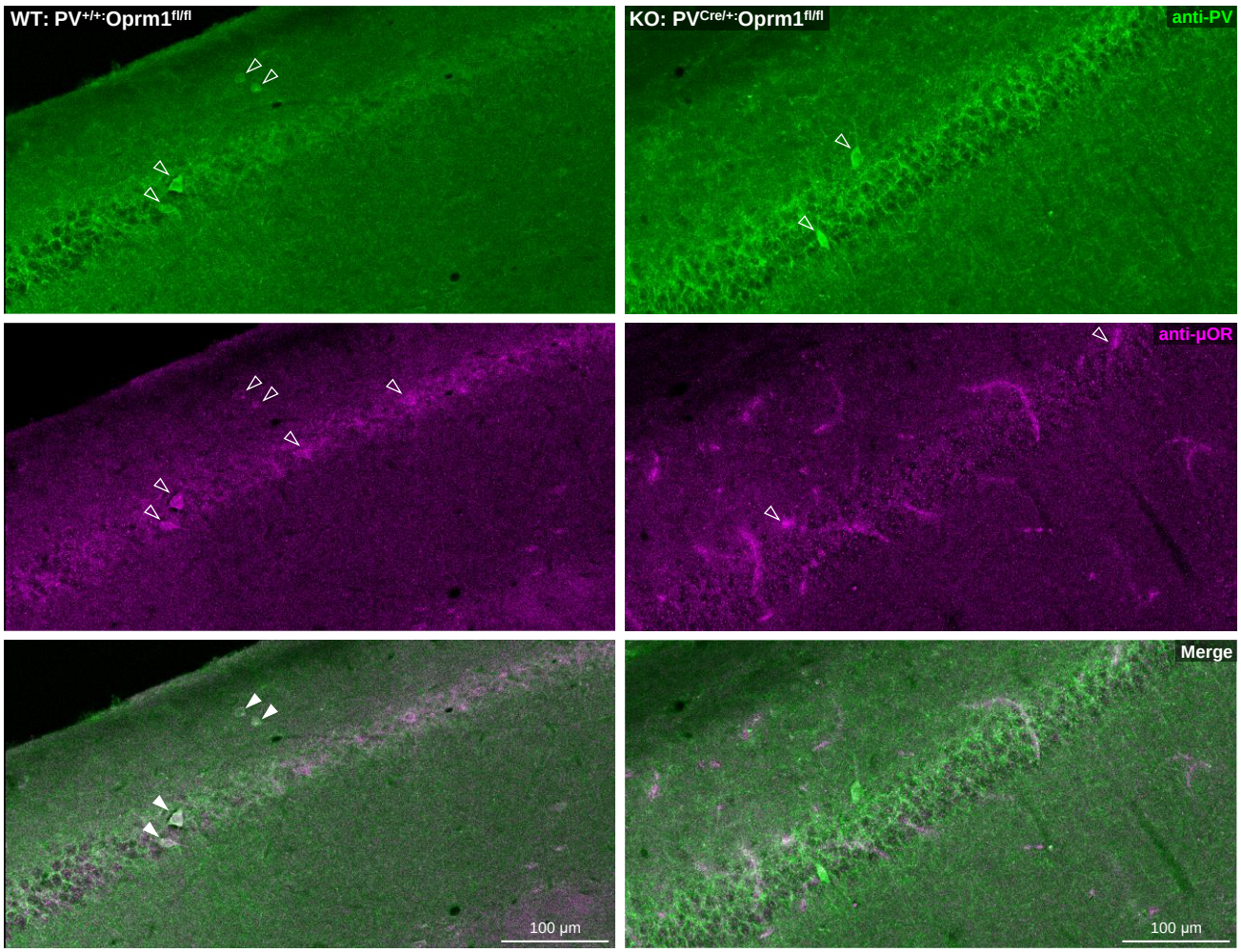
WT: PV+/+:Oprm1fl/fl
KO: PVCre/+:Oprm1fl/fl
anti-PV
anti-μOR
Merge
100 μm
100 μm

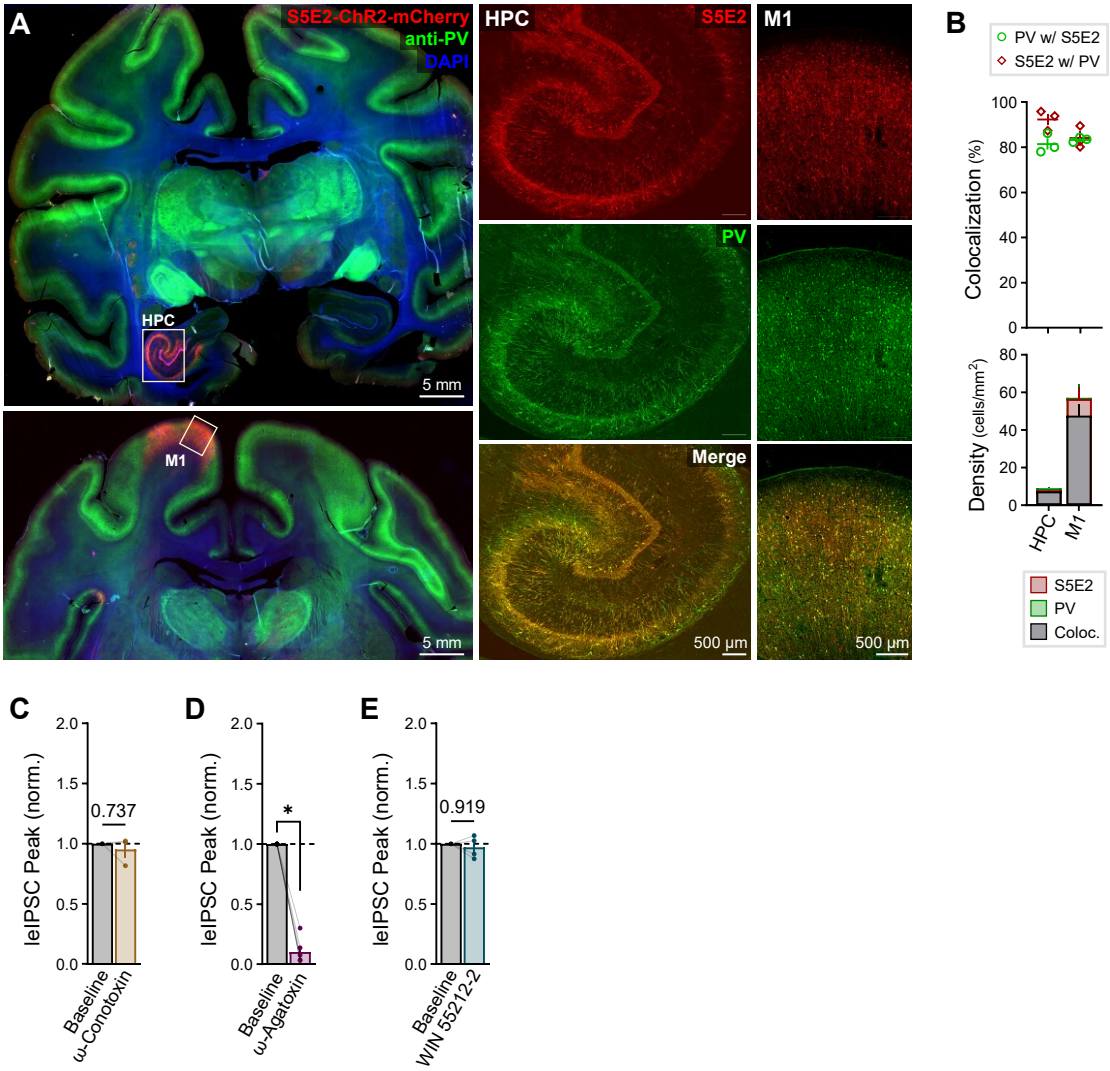
A
S5E2-ChR2-mCherry
anti-PV
DAPI
HPC
5 mm
M1
5 mm
HPC
S5E2
M1
PV
Merge
500 µm
500 µm
B
PV w/ S5E2
S5E2 w/ PV
Colocalization (%)
100
80
60
40
20
0
Density (cells/mm²)
80
60
40
20
0
HPC
M1
S5E2
PV
Coloc.
C
D
E
IeIPSC Peak (norm.)
2.0
1.5
1.0
0.5
0.0
0.737
*
0.919
Baseline
ω-Conotoxin
Baseline
ω-Agatoxin
Baseline
WIN 55212-2

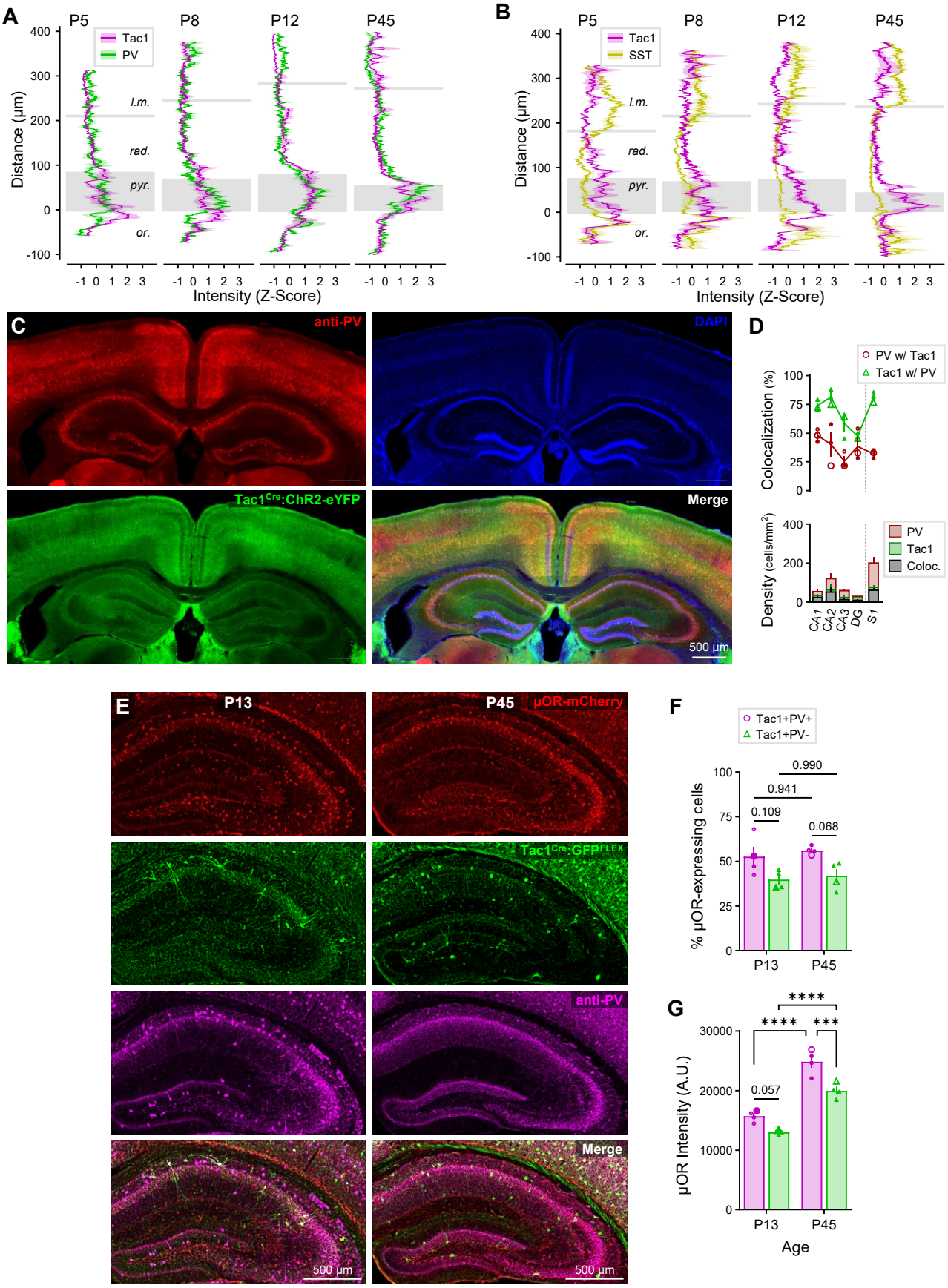
A
P5
P8
P12
P45
Tac1
PV
Distance (µm)
l.m.
rad.
pyr.
or.
Intensity (Z-Score)
B
Tac1
SST
C
anti-PV
DAPI
Tac1Cre:ChR2-eYFP
Merge
500 µm
D
PV w/ Tac1
Tac1 w/ PV
Colocalization (%)
Density (cells/mm2)
PV
Tac1
Coloc.
CA1
CA2
CA3
DG
S1
E
P13
P45
µOR-mCherry
Tac1Cre:GFPFLEX
anti-PV
Merge
500 µm
F
Tac1+PV+
Tac1+PV-
% µOR-expressing cells
0.990
0.941
0.109
0.068
G
µOR Intensity (A.U.)
****
***
0.057
Age

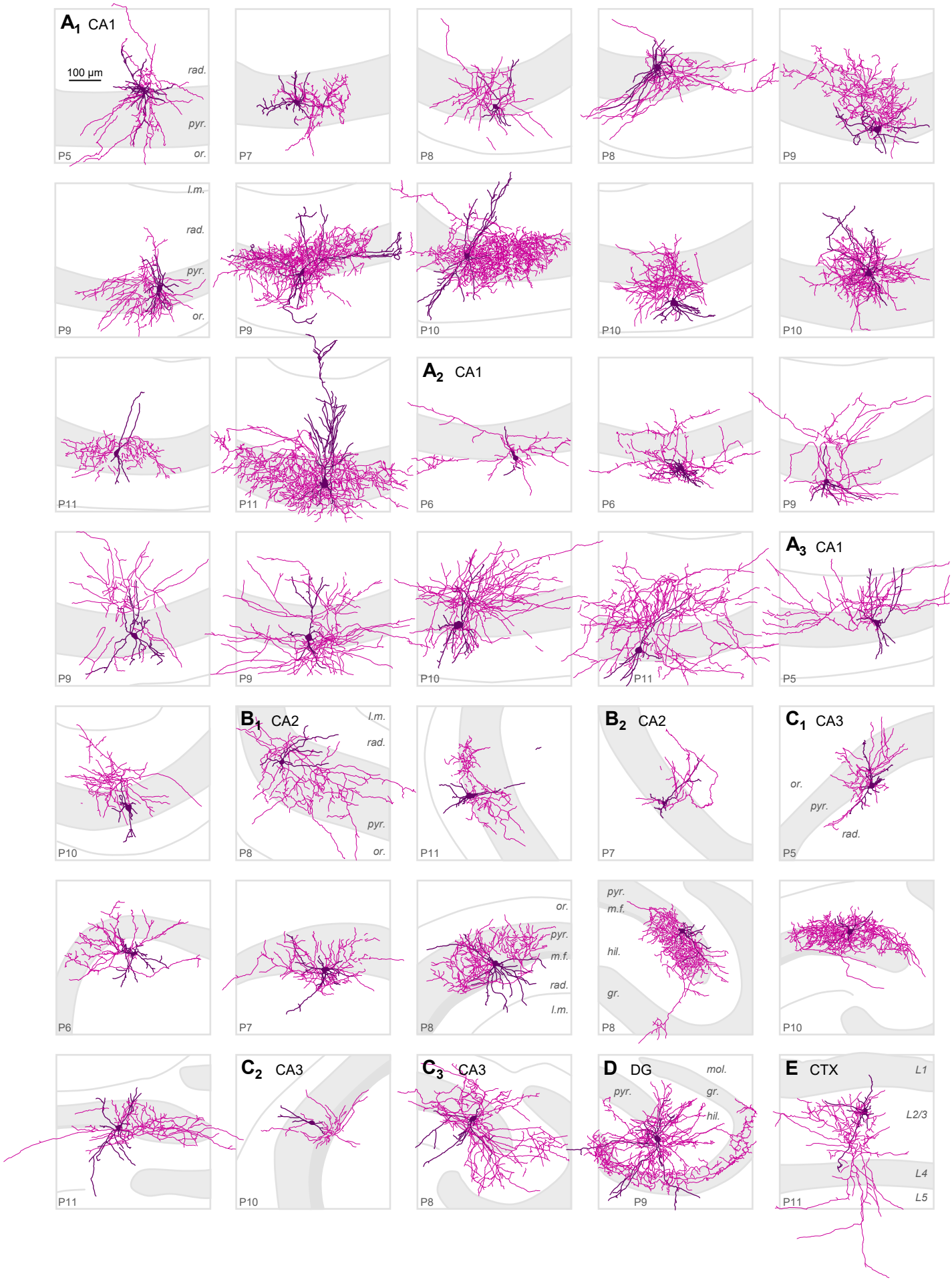
A1 CA1
100 µm
rad.
pyr.
or.
P5
P7
P8
P8
P9
l.m.
rad.
pyr.
or.
P9
P9
P10
P10
P10
P11
P11
A2 CA1
P6
P6
P9
P9
P9
P10
P11
A3 CA1
P5
P10
B1 CA2
l.m.
rad.
pyr.
or.
P8
P11
B2 CA2
P7
C1 CA3
or.
pyr.
rad.
P5
P6
P7
or.
pyr.
m.f.
rad.
l.m.
P8
pyr.
m.f.
hil.
gr.
P8
P10
P11
C2 CA3
P10
C3 CA3
P8
D DG
mol.
pyr.
gr.
hil.
P9
E CTX
L1
L2/3
L4
L5
P11

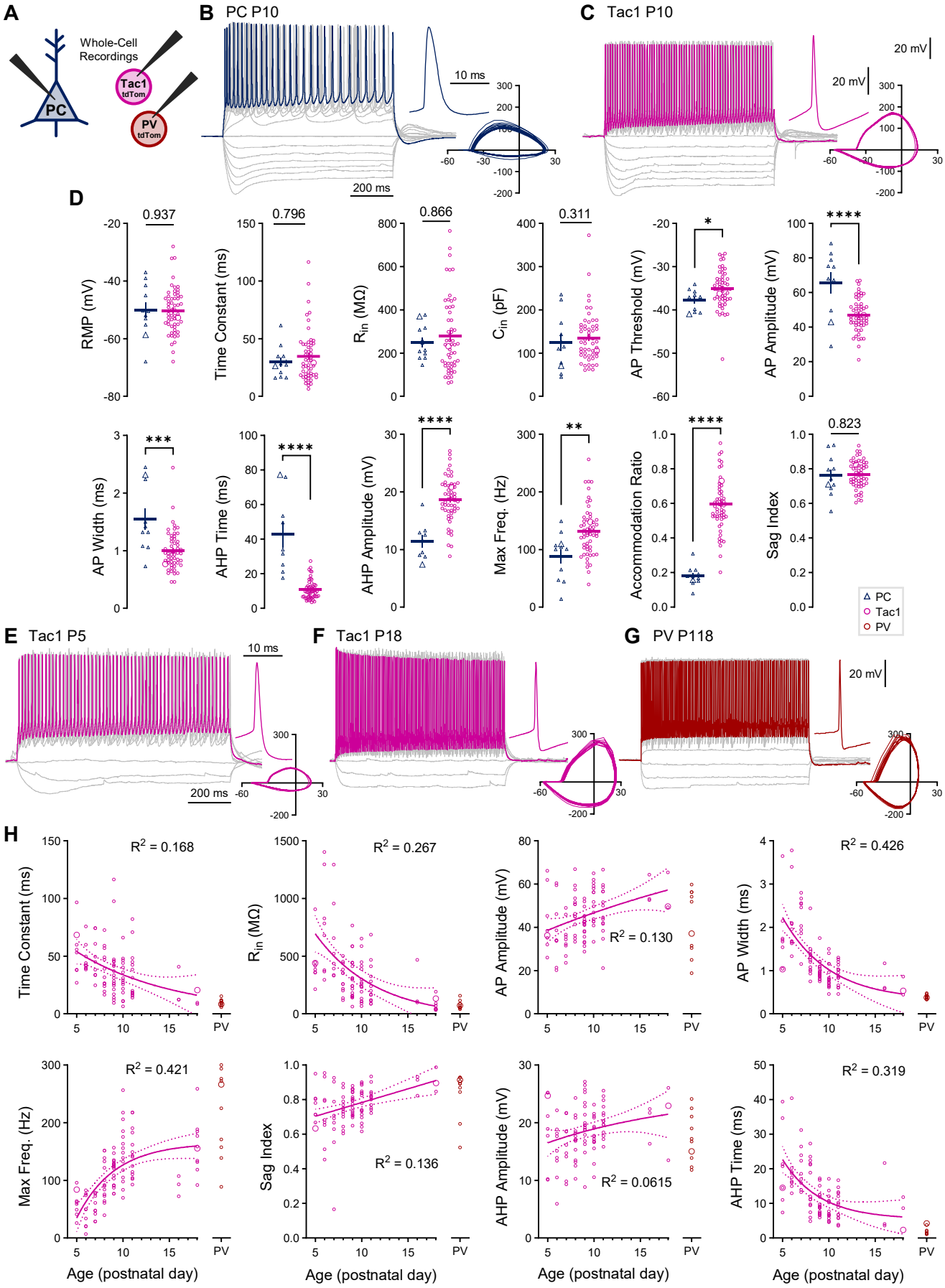
A
Whole-Cell Recordings
PC
Tac1 tdTom
PV tdTom
B PC P10
10 ms
200 ms
C Tac1 P10
20 mV
20 mV
D
RMP (mV)
0.937
Time Constant (ms)
0.796
Rin (MΩ)
0.866
Cin (pF)
0.311
AP Threshold (mV)
*
AP Amplitude (mV)
****
AP Width (ms)
***
AHP Time (ms)
****
AHP Amplitude (mV)
****
Max Freq. (Hz)
**
Accommodation Ratio
****
Sag Index
0.823
PC
Tac1
PV
E Tac1 P5
10 ms
200 ms
F Tac1 P18
G PV P118
20 mV
H
R2 = 0.168
R2 = 0.267
R2 = 0.130
R2 = 0.426
R2 = 0.421
R2 = 0.136
R2 = 0.0615
R2 = 0.319
Time Constant (ms)
Rin (MΩ)
AP Amplitude (mV)
AP Width (ms)
Max Freq. (Hz)
Sag Index
AHP Amplitude (mV)
AHP Time (ms)
PV
Age (postnatal day)

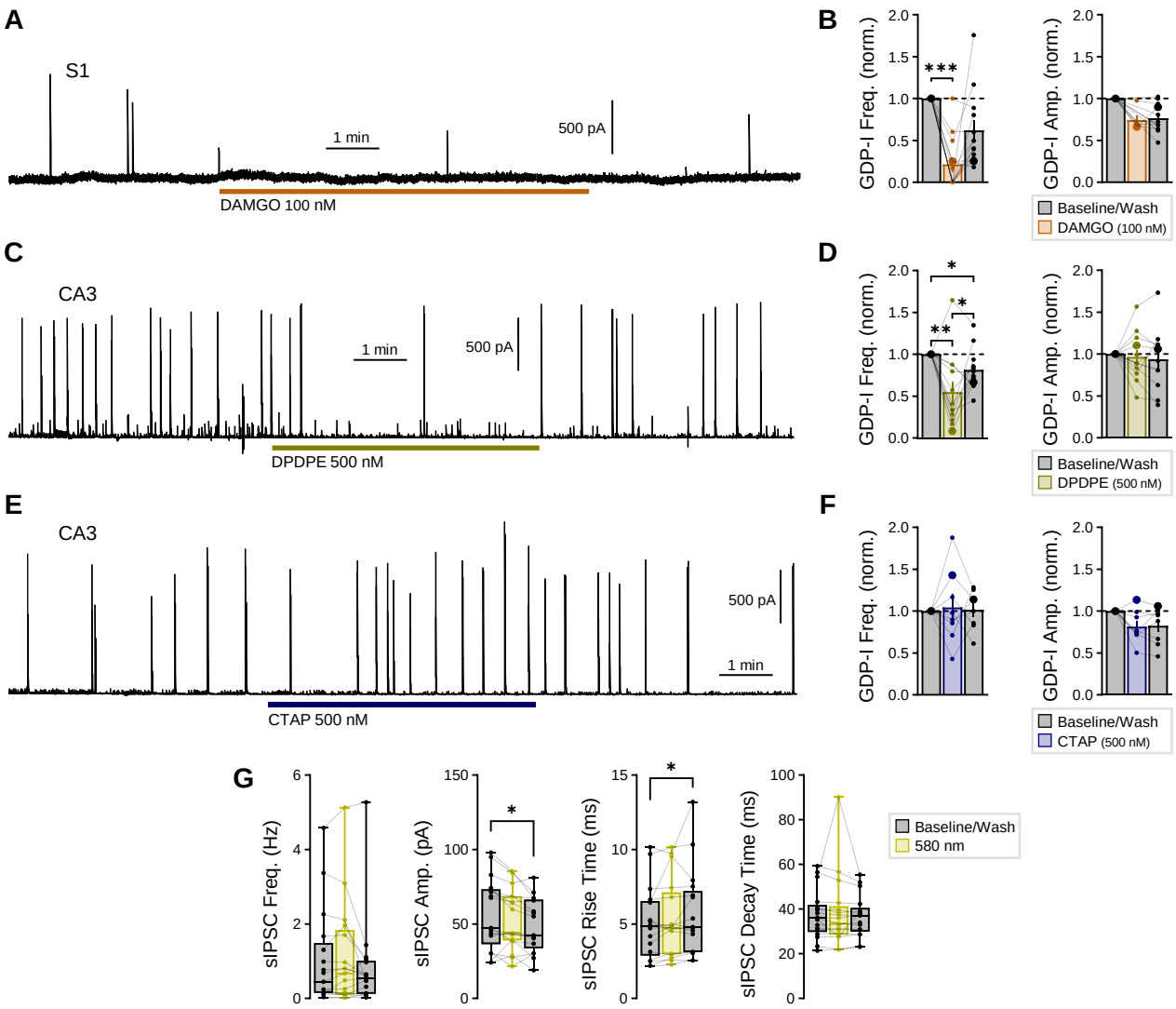
A
S1
1 min
500 pA
DAMGO 100 nM
B
GDP-I Freq. (norm.)
GDP-I Amp. (norm.)
***
Baseline/Wash
DAMGO (100 nM)
C
CA3
1 min
500 pA
DPDPE 500 nM
D
GDP-I Freq. (norm.)
GDP-I Amp. (norm.)
*
**
*
Baseline/Wash
DPDPE (500 nM)
E
CA3
500 pA
1 min
CTAP 500 nM
F
GDP-I Freq. (norm.)
GDP-I Amp. (norm.)
Baseline/Wash
CTAP (500 nM)
G
sIPSC Freq. (Hz)
sIPSC Amp. (pA)
sIPSC Rise Time (ms)
sIPSC Decay Time (ms)
*
*
Baseline/Wash
580 nm